

STRUCTURE EVOLUTION AND NANO-MECHANICAL BEHAVIOR OF BULK
METALLIC GLASSES AND MULTI-PRINCIPAL ELEMENT ALLOYS

Sanghita Mridha, B.E., M.E.

Dissertation Prepared for the Degree of

DOCTOR OF PHILOSOPHY

UNIVERSITY OF NORTH TEXAS

May 2017

APPROVED:

Sundeeep Mukherjee, Major Professor
Jincheng Du, Committee Member
Narendra Dahotre, Committee Member
Rajarshi Banerjee, Committee Member
Marcus Young, Committee Member
Andrey Voevodin, Chair of the Department of
Materials Science and Engineering
Costas Tsatsoulis, Dean of the College of
Engineering
Victor Prybutok, Vice Provost of the Toulouse
Graduate School

Mridha, Sanghita. *Structure Evolution and Nano-Mechanical Behavior of Bulk Metallic Glasses and Multi-Principal Element Alloys*. Doctor of Philosophy (Materials Science and Engineering), May 2017, 130 pp., 6 tables, 84 figures, chapter references.

Bulk metallic glasses and multi-principal element alloys represent relatively new classes of multi-component engineering materials designed for satisfying multiple functionalities simultaneously. Correlating the microstructure with mechanical behavior (at the microstructural length-scales) in these materials is key to understanding their performance. In this study, the structure evolution and nano-mechanical behavior of these two classes of materials was investigated with the objective of fundamental scientific understanding of their properties. The structure evolution, high temperature nano-mechanical behavior, and creep of two Zr-based alloys was studied: Zr_{41.2}Ti_{13.8}Cu_{12.5}Ni_{10.0}Be₂₂ (Vitreloy1) and Zr_{52.5}Ti₅Cu_{17.9}Ni_{14.6}Al₁₀ (Vitreloy105). Devitrification was found to proceed via the formation of a metastable icosahedral phase with five-fold symmetry. The deformation mechanism changes from inhomogeneous or serrated flow to homogenous flow near 0.9T_g, where T_g is the glass transition temperature. The creep activation energy for Vitreloy1 and Vitreloy105 were 144 kJ/mol and 125 kJ/mol, respectively in the range of room temperature to 0.75T_g. The apparent activation energy increased drastically to 192 kJ/mol for Vitreloy1 and 215 kJ/mol for Vitreloy105 in the range of 0.9T_g to T_g, indicating a change in creep mechanism. Structure evolution in catalytic amorphous alloys, Pt_{57.5}Cu_{14.7}Ni_{5.3}P_{22.5} and Pd₄₃Cu₂₇Ni₁₀P₂₀, was studied using 3D atom probe tomography and elemental segregation between different phases and the interface characteristics were identified.

Copyright 2017

By

Sanghita Mridha

ACKNOWLEDGEMENT

I would like to express my deep regards to Dr. Sundeep Mukherjee for his kind support, guidance, supervision and encouragement throughout my PhD. His knowledge, experience and guidance were instrumental in shaping my overall research perspective in the diverse field of material science and engineering. I would also like to thank Dr. Mishra for his support and guidance.

I would like to express my gratitude to my committee members Dr. Dahotre, Dr. Young, Dr. Du and Dr. Banerjee for their valuable inputs to my dissertation.

I would like thank everyone who has helped me with my PhD (Aniket, Ved, Aditya, Jitu, Shami, Medha, Nishitha, Harpreet, Shantanu, Dr. Bhowmick, Dr. Jaeger, Bharat, Sameehan, Seth, Vahid, Hunter, Jennifer, Ailen, Nelson, Maggie, Kai, Shiva, Urmila and other friends and colleagues)

I am deeply grateful to my parents, sisters, brothers and other family members. I would like to thank my husband for his love and support.

TABLE OF CONTENTS

	Page
ACKNOWLEDGEMENT	iii
LIST OF TABLES	vii
LIST OF FIGURES	viii
CHAPTER 1. INTRODUCTION	1
1.1. Bulk Metallic Glass.....	1
1.1.1. Bulk Metallic Glasses and Their Unique Properties.....	1
1.1.2. History of Bulk Metallic Glasses	5
1.1.3. Glass Formation	6
1.1.4. Devitrification Behavior	8
1.1.5. Mechanical Behavior	8
1.2. Multi-Principal Element Alloys (MPEAs).....	16
1.2.1. Core Effects	17
1.2.2. Enthalpy of Formation	21
1.3. Thesis Overview	21
1.4. References.....	23
CHAPTER 2. EXPERIMENTAL TECHNIQUES.....	28
2.1. X-Ray Diffraction (XRD)	28
2.2. Differential Scanning Calorimetry (DSC)	29
2.3. Scanning Electron Microscopy (SEM)	29
2.4. Electron Backscatter Diffraction (EBSD).....	30
2.5. Focused Ion Beam (FIB).....	30
2.6. Transmission Electron Microscopy (TEM)	31
2.7. 3D Atom Probe (3DAP).....	32
2.8. Nano-Indentation	32
2.8.1. Load-Displacement Curve	34
2.8.2. Hardness and Modulus Measurement.....	35
2.8.3. Nano-Indentation Setup	37
2.8.4. Room Temperature Test Set Up	38

2.8.5. High Temperature Set Up	39
2.8.6. Calibration.....	40
2.9. Pico-Indentation	42
2.10. Data Analysis	44
2.11. References.....	46
CHAPTER 3. EVOLUTION OF ATOMIC DISTRIBUTION DURING DEVITRIFICATION OF BULK METALLIC GLASS INVESTIGATED BY ATOM PROBE MICROSCOPY AND NANO-INDENTATION	47
3.1. Abstract	47
3.2. Introduction.....	47
3.3. Experimental	48
3.4. Results and Discussion	49
3.5. Conclusions.....	59
3.6. References.....	59
CHAPTER 4. ATOMIC DISTRIBUTION IN CATALYTIC AMORPHOUS METALS.....	61
4.1. Abstract	61
4.2. Introduction.....	61
4.3. Experimental	63
4.4. Results and Discussion	63
4.5. Conclusions.....	71
4.6. References.....	72
CHAPTER 5. HIGH TEMPERATURE NANO-MECHANICAL BEHAVIOR OF BULK METALLIC GLASSES	74
5.1. Abstract	74
5.2. Introduction.....	74
5.3. Experimental	75
5.4. Results and Discussion	76
5.5. Conclusions.....	82
5.6. References.....	82
CHAPTER 6. STRAIN GRADIENT PLASTICITY IN MULTI-PRINCIPAL ELEMENT ALLOYS.....	84
6.1. Abstract	84

6.2.	Introduction.....	84
6.3.	Experimental.....	85
6.4.	Results.....	86
6.5.	Conclusions.....	94
6.6.	References.....	95
CHAPTER 7. DISLOCATION NUCLEATION IN MULTI-PRINCIPAL ELEMENT ALLOYS		
.....		97
7.1.	Abstract.....	97
7.2.	Introduction.....	97
7.3.	Experimental.....	99
7.4.	Results and Discussion	100
7.5.	Discussion.....	108
	7.5.1. Homogeneous Dislocation Nucleation	108
	7.5.2. Heterogeneous Dislocation Nucleation.....	109
7.6.	Conclusions.....	111
7.7.	References.....	111
CHAPTER 8. STRAIN RATE SENSITIVITY OF NANOCRYSTALLINE $Al_{0.1}CoCrFeNi$		
MULTI-PRINCIPAL ELEMENT ALLOY.....		115
8.1.	Abstract.....	115
8.2.	Introduction.....	115
8.3.	Experimental.....	116
8.4.	Results and Discussion	117
8.5.	Conclusions.....	124
8.6.	Future Work.....	124
8.7.	References.....	124
APPENDIX A. LOAD FUNCTION FOR ROOM TEMPERATURE AND HIGH		
TEMPERATURE INDENTATION		127
APPENDIX B. LIST OF PUBLICATIONS.....		129

LIST OF TABLES

	Page
Table 3.1: Elemental composition in the as-cast Vitreloy1, $Zr_{41.2}Ti_{13.8}Cu_{12.5}Ni_{10.0}Be_{22.5}$ (As-cast), metallic glass annealed at 663K for 5 min, metallic glass annealed at 673K for 10 min and fully crystallized metallic glass, as determined by 3D atom probe microscopy. Phases “A”, “B”, “C”, and “D” in the fully crystallized sample are shown in Figure 3.3. [12]	51
Table 3.2: Volume fraction and chemical composition of icosahedral phase as a function of size for Vitreloy1 ($Zr_{41.2}Ti_{13.8}Cu_{12.5}Ni_{10.0}Be_{22.5}$), annealed at 673 K for 10 minutes. [12]	53
Table 3.3: Vicker hardness and Nano-indentation hardness and modulus for as-cast glass, glass embedded with quasi-crystal and devitrified glass	56
Table 4.1: Elemental composition (at. %) obtained using atom probe microscopy of different phases identified in crystallized $Pd_{43}Cu_{27}Ni_{10}P_{20}$ metallic glass [9]	68
Table 4.2: Elemental composition (at. %) obtained using atom probe microscopy of different phases identified in crystallized $Pt_{57.5}Cu_{14.7}Ni_{5.3}P_{22.5}$ metallic glass [9]	68
Table 7.1: Reduced modulus, activation volume, and activation enthalpy of three alloys	103

LIST OF FIGURES

	Page
Figure 1.1: Bulk metallic glass forming palladium alloy with diameter ranging over 3 mm to 6mm.	2
Figure 1.2: Strength vs elastic limit for BMGs compared to other structural materials [7].	2
Figure 1.3: Strength versus temperature plot for steel, metallic glass and plastic. Above glass transition temperature (T_g), BMG softens to a viscous liquid and can be processed like plastic [9].	3
Figure 1.4: Macro- to nano-scale BMG fabricated by thermos-plastic forming [10].	4
Figure 1.5: Application for BMGs: (a) Glof club head and (b) Omega watch components.	4
Figure 1.6: Critical casting thickness of different metallic glass alloy systems and the corresponding year they were reported [17]	5
Figure 1.7: Schematic showing the periodic structure for a crystalline metal and disordered structure for glass.	6
Figure 1.8: Schematic TTT Diagram. Liquid metal forms glassy structure when cooled with cooling rates higher than curve (1). Below T_g the liquid atoms fall out of equilibrium and are frozen in a random disordered phase known as “glass”.	7
Figure 1.9: Two-dimensional schematic of atomistic deformation mechanism proposed on shear transformation zone, Argon model [23].	9
Figure 1.10: Two-dimensional schematic of atomistic deformation mechanism proposed on a local atomic jump, Spaepen [24].	10
Figure 1.11: Steady-state homogenous flow data for $Zr_{41.2}Ti_{13.8}Cu_{12.5}Ni_{10}Be_{22.5}$ metallic glass at high temperatures [36].	12
Figure 1.12: $Pd_{40}Ni_{40}P_{20}$ metallic glass wires before and after deformation at $T = 620$ K and $\dot{\epsilon} = 10^{-1}s^{-1}$ [36].	13
Figure 1.13: (a) Stress overshoot and (b) stress undershoot during strain rate change testing [24].	13
Figure 1.14: The process of strain localization and calculation from the work of (a) Argon [23] (b) Steif et al. [42].	14
Figure 1.15: Deformation map of metallic glass: (a) stress-temperature and (b) strain rate-temperature [45,47,50].	15

Figure 1.16: Schematic illustration of conventional alloying approach and MPEA alloying approach [52].	16
Figure 1.17: XRD patterns of binary to septenary alloys [62].	18
Figure 1.18: Schematic of potential energy change for migration in Ni atom in pure metal, Fe-Cr-Ni and CoCrFeMn _{0.5} Ni alloy [65].	19
Figure 1.19: Schematic illustration of FCC structure of single element (left) and distorted FCC structure of MPEA (right) [68].	20
Figure 1.20: Hardness of Al _x CoCrCuFeNi alloy as a function of Al content [62].	21
Figure 2.1: Bragg's law and principle of x-ray diffraction.	28
Figure 2.2: Inside view of differential scanning calorimeter.	29
Figure 2.3: Schematic of EBSD set up.	30
Figure 2.4: Schematic of FIB system and principles of FIB including: (a) Imaging, (b) Milling, and (c) Deposition.	31
Figure 2.5: Schematic diagram of a three-dimensional atom probe.	32
Figure 2.6: (a) shows a series of indentations performed on the sample, (b) shows an isolated indentation on amorphous matrix, (c) on the crystalline dendrite and, (d) on the interphase boundary of the two phases. The corresponding modulus and hardness obtained from the series of indentations shown in (a) is shown in (e) and (f) respectively [1].	33
Figure 2.7: Schematic of load displacement curve.	35
Figure 2.8: Projected area of berkovich tip.	36
Figure 2.9: Set up of Hysitron nano-indenter and high temperature stage.	38
Figure 2.10: (a) Nanoindenter with high temperature stage, (b) expended view of the dashed white box.	40
Figure 2.11: Schematic of picoindenter set up.	43
Figure 2.12: Zoomed in view of the stage and tip for high temperature test.	44
Figure 2.13: (a) Pillar compression of Au single crystal and (b) stress-strain generated plot [7].	45
Figure 3.1: (a) DSC curve obtained by heating as-cast Vitreloy1 at a rate of 20 K/min; (b) XRD for as-cast metallic glass, metallic glass annealed at 673 K for 10 min, and fully crystallized metallic glass; (c) Atom probe 3D reconstruction and (d) concentration profile for as-cast metallic glass. The glass transition and crystallization temperatures are indicated by T _g and T _x	

respectively. Tp1 and Tp2 are the first and second crystallization peaks respectively. XRD shows fully amorphous structure for the as-cast sample and sample annealed at 663 K for 5 minutes. The sample annealed at 673 K for 10 min shows the formation of metastable i-phase, while the fully crystallized sample shows six different binary phases [12]. 50

Figure 3.2: Atom probe 3D reconstruction for sample annealed at 673 K for 10 min showing (a) i-phase particle and amorphous matrix and (b) i-phase particle with the matrix suppressed; (c) An isolated i-phase particle and (d) concentration profile along the line 1-1' shown in (c), HRTEM image showing icosahedra-like short range clusters in an amorphous matrix. White dashed lines around the clusters are added as a guide to the eye. [12]..... 52

Figure 3.3: (a) and (b) Atom probe 3D reconstruction for fully crystallized metallic glass; (c) concentration profile between phases A and B; (d) SEM image showing the microstructure of the crystallized metallic glass. Atom probe results show the formation of four distinct regions marked by “A”, “B”, “C” and “D”. SEM shows nanocrystalline phases in the size range of 10 nm to 100 nm [12]..... 54

Figure 3.4: (a) Hardness and (b) modulus of glass, glass+i-phase and crystallized at different temperatures. 57

Figure 3.5: Loading curve of glass, glass+i-phase, and crystallized sample at (a) 298K, (b) 373K, (c) 473K, and (d) 598K. 58

Figure 4.1: DSC curves for (a) $\text{Pd}_{43}\text{Cu}_{27}\text{Ni}_{10}\text{P}_{20}$ metallic glass and (b) $\text{Pt}_{57.5}\text{Cu}_{14.7}\text{Ni}_{5.3}\text{P}_{22.5}$ metallic glass; (c) SEM micrograph for the crystallized $\text{Pd}_{43}\text{Cu}_{27}\text{Ni}_{10}\text{P}_{20}$ alloy; (d) SEM micrograph for the crystallized $\text{Pt}_{57.5}\text{Cu}_{14.7}\text{Ni}_{5.3}\text{P}_{22.5}$ alloy. The glass transition and crystallization temperatures are indicated by T_g and T_x respectively. Pd alloy has a lamellar eutectic structure compared to an acicular eutectic structure for the Pt alloy [9]. 65

Figure 4.2: XRD analysis curves for (a) $\text{Pd}_{43}\text{Cu}_{27}\text{Ni}_{10}\text{P}_{20}$ metallic glass and (b) $\text{Pt}_{57.5}\text{Cu}_{14.7}\text{Ni}_{5.3}\text{P}_{22.5}$ metallic glass in as-cast amorphous and crystallized form. The different crystalline phases are marked alongside the XRD peaks [9]. 66

Figure 4.3: (a) 3DAP reconstruction and (b) elemental distribution for as cast $\text{Pd}_{43}\text{Cu}_{27}\text{Ni}_{10}\text{P}_{20}$ metallic glass; (c) 3DAP reconstruction and (d) elemental distribution for as cast $\text{Pt}_{57.5}\text{Cu}_{14.7}\text{Ni}_{5.3}\text{P}_{22.5}$ metallic glass. Atom probe results show homogeneous distribution of all the elements in the as-cast structure of both the alloys [9]. 67

Figure 4.4: (a) SEM image of crystallized $\text{Pd}_{43}\text{Cu}_{27}\text{Ni}_{10}\text{P}_{20}$ metallic glass used for atom-probe microscopy; (b) 3DAP reconstruction for $\text{Pd}_{43}\text{Cu}_{27}\text{Ni}_{10}\text{P}_{20}$ metallic glass crystallized at 450 °C; (c) elemental map and (d) composition profile across the interface between phases “1” and “3”; (e) elemental map and (f) composition profile across the interface between phases “1” and “2”; Phases marked 1, 2 and 3 corresponds to Pd_7P_2 , PdCu_3 and $\text{Pd}_4\text{Ni}_3\text{P}_3$ respectively. The thickness of all the interfaces was found to be less than 0.5 nm [9]. 69

Figure 4.5: (a) 3DAP reconstruction for $\text{Pt}_{57.5}\text{Cu}_{14.7}\text{Ni}_{5.3}\text{P}_{22.5}$ metallic glass crystallized at 450 °C; (b) elemental distribution and composition profile across the interface between phases “1” and “2”; Phases marked 1 and 2 corresponds to Pt_3PCu and PtP_2 respectively [9]. 70

Figure 5.1: The hardness and modulus of the (a) Vitreloy 1 and (b) Vitreloy 105 as function of T_g . Both the glass show decrease in hardness and modulus with increasing temperature.....	77
Figure 5.2: Loading curve of (a) Vitreloy 1 and (b) Vitreloy 105 at different at different temperature as function of T_g . Both the glass show serrated plastic deformation at lower temperature (up to $0.91T_g$) due to formation of shear band. At higher temperature ($0.95T_g$) the glass shows uniform plastic deformation as the glass behave as Newtonian fluid at higher temperature.	77
Figure 5.3: Displacement vs time plot at constant load of 8000 μN at different temperature as a function of T_g for (a) Vitreloy 1 (b) Vitreloy 105 shows an increase in displacement rate at higher temperature (above $0.91T_g$).	80
Figure 5.4: Minimum creep rate of Vitreloy 1 and Vitreloy 105 at different temperature as function of T_g . Vitreloy 1 shows lower minimum creep than Vitreloy 105 at all temperature.....	81
Figure 5.5: $\ln(\text{strain rate})$ vs T plot to evaluate the apparent activation energy of creep for the glass. As the deformation mechanism changes the activation energy also get changed. (a) Vitreloy 1 $0.4-0.74T_g$, (b) Vitreloy 1 $0.91T_g - T_g$, (c) Vitreloy 105 $0.4-0.74T_g$, and (d) Vitreloy 105 $0.91T_g - T_g$	81
Figure 6.1: X-ray diffraction for annealed and rolled condition for CoCrNi and CoCrFeMnNi.	86
Figure 6.2: SEM backscattered micrographs of CoCrNi alloy (a) annealed and (b) work hardened and CoCrFeMnNi alloy (c) annealed and (d) work hardened condition.	87
Figure 6.3: EBSD map of (a) CoCrNi alloy and (d) CoCrFeMnNi alloy of annealed sample, (b) and (e) grain size distribution and (c) and (f) misorientation angle for both the annealed sample.	88
Figure 6.4: (a) and (b) Load–displacement plots at a load of 8000 μN ; (c) and (d) Nano-Hardness and Vicker-Hardness plot for the different processing conditions at a load of 8000 μN for Ni, CoCrNi and CoCrFeMnNi.....	89
Figure 6.5: Hardness as a function of depth for (a) annealed samples (b) work hardened samples of Ni, CoCrNi and CoCrFeMnNi alloys.....	91
Figure 6.6: $(H/H_0)^2$ versus $1/h_c$ plot to show the depth dependence of hardness for Ni (a) annealed and (d) work hardened, CoCrNi alloy (c) annealed and (d) work hardened and CoCrFeMnNi alloy (e) annealed and (f) work hardened samples.	93
Figure 7.1: XRD pattern of multi-principal CoCrFeMnNi, $\text{Al}_{0.1}\text{CoCrFeNi}$, and CoCrNi alloys after rolling and annealing for 20h. The XRD peaks corresponds to single phase FCC structure	100
Figure 7.2: Backscattered SEM image of the annealed samples (a) $\text{Al}_{0.1}\text{CoCrFeNi}$, (b) CoCrFeMnNi, (c) CoCrNi. Shows equiaxed grain in the alloys after annealing with grain size 30-60 μm	101

Figure 7.3: (a) representative load-displacement curve of CoCrFeMnNi alloy for single indent performed at room temperature along with the Hertzian. Green circle shows the “pop-in” event in the load-displacement curve. (b) load-displacement curve of CoCrFeMnNi alloy at different temperature along with the Hetzian equation.	102
Figure 7.4: Cumulative fraction of experiment loads at the pop-in events plotted for 25°C and 200°C for (a) Ni, (c) CoCrNi alloys, (c) CoCrFeMnNi, and (d) Al _{0.1} CoCrFeNi.....	104
Figure 7.5: Plot of $\ln[-\ln(1-F)]$ vs $P^{1/3}$ to determine the activation volume from experimental data analysis at 25°C and 200°C for (a) Ni, (b) CoCrNi, , (c) CoCrFeMnNi, and (d) Al _{0.1} CoCrFeNi	106
Figure 7.6: Plot of $P^{1/3}$ vs T to evaluate the activation enthalpy for the first burst for (a) Ni, (b) CoCrNi, (c) CoCrFeMnNi, and (d) Al _{0.1} CoCrFeNi alloys.	107
Figure 8.1: (a) XRD patterns of thin film and target Al _{0.1} CoCrFeNi MPEA, showing peak correspond to FCC phase, and (b) SEM image of the thin film showing nano-size grains with average grain size of 40 nm.	118
Figure 8.2: (a) SEM image during the test showing diamond punch and nano-pillar (b) SEM image of the nano-pillar with diameter 450 nm (c) SEM image of the nano-pillar after compression test.....	119
Figure 8.3: (a) Engineering stress – engineering strain curve at strain rate of $7.5 \times 10^{-3} \text{ s}^{-1}$ showing YS of 2376 MPa. Insets show the in situ image of pillar at different engineering strain during the test (b) YS vs $d^{-1/2}$ plot with Hall-Petch equation (H-P) fit. Hall-Petch parameters, σ_0 and k for MPEA were 126 MPa and 449 MPa (μm) ^{1/2} and for Ni 70 MPa and 250 MPa (μm) ^{1/2} , respectively.	120
Figure 8.4: (a) Engineering stress - engineering strain plot at different strain rates showing the increase in tensile strength with increase in strain rate; (b) flow stress at 1% offset strain vs strain rate plot in ln scale to calculate the strain rate sensitivity, m. The calculated m was 0.043 for the NC Al _{0.1} CoCrFeNi MPEA.....	122

CHAPTER 1

INTRODUCTION

Traditional alloy development has been focused to fulfil the requirement of principal property, termed “first-tier” property. There is a paradigm shift in design of structural materials to fulfil the increasing demands. This paradigm shift inspired to develop new alloy systems that simultaneously satisfy multiple “next-tier” properties [1]. MPEAs and BMGs are the examples of the alloys, which are developed based on such strategy. Both MPEAs and BMGs are disordered alloys and possess excellent mechanical and physical properties combining superior corrosion properties. Both the alloys are catalogued under same group of alloys as both formed into a solid solution, in spite of different crystallographic structure [2]. MPEAs have simple BCC, FCC or mixed BCC and FCC structure, whereas BMGs have glassy structure. The alloy design of MPEAs and BMGs follow common factors [3]: (i) number of elements (N)- for MPEAs, equiatomic or near equiatomic multicomponent alloys with five or more elements ($N \geq 5$) and for BMGs $N \geq 3$ except few couple of binary alloys, such as Cu-Zr [4,5] and Ni-Nb [6]., (ii) difference in atomic size- MPEAs not limited by definition but cover the Inoue’s second rule for BMGs, and (iii) mixing enthalpy. Beside these factors, entropy plays important role in MPEAs and BMGs. MPEAs are characterized by configurational entropy (S_{conf}). For BMGs, a mismatch entropy (S_{σ}) is used to describe the difference in atomic size, which is similar to delta parameter (δ) in MPEAs [2].

1.1. Bulk Metallic Glass

1.1.1. Bulk Metallic Glasses and Their Unique Properties

Bulk metallic glasses (BMGs) are multicomponent metallic alloys with exceptional stability against crystallization. Some of the newer BMG compositions can be produced in length-scales on the order of few centimeters with fully amorphous structure (Figure 1.1) [7,8]. BMGs

exhibit an unusual combination of physical, mechanical, magnetic and chemical properties. Compared to their crystalline counterparts, BMGs demonstrate very high strength ($\sim 2\text{GPa}$) and hardness ($\sim 6\text{GPa}$). Compared to commonly used structural materials, metallic glasses demonstrate significantly higher strength and close to theoretical elasticity (Figure 1.2).[7]



Figure 1.1: Bulk metallic glass forming palladium alloy with diameter ranging over 3 mm to 6mm.

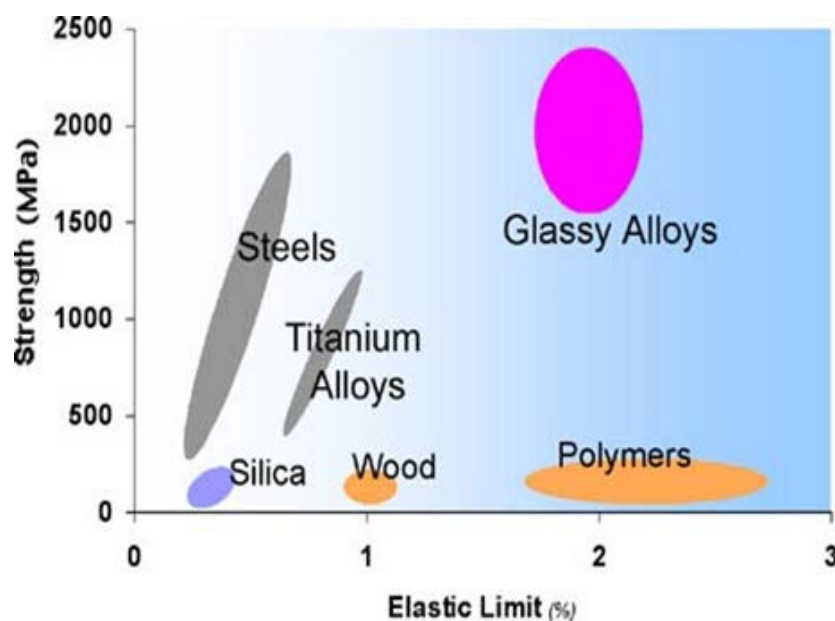


Figure 1.2: Strength vs elastic limit for BMGs compared to other structural materials [7].

One of the unique characteristics of metallic glasses is their ability to be processed into complicated shapes through thermo-plastic forming with applications ranging from fuel cells to micro-electro-mechanical systems (MEMS). When heated above their glass transition temperature (T_g) in the supercooled liquid region, these glassy alloys can be easily processed to form near-net shape structures over multiple length-scales. Figure 1.3 shows the decrease in strength and viscosity with increase in temperature for BMGs. Above the glass transition temperature, the metallic glass softens into a viscous liquid and can be processed like a plastic. Casting defects will be low due to low processing temperature.

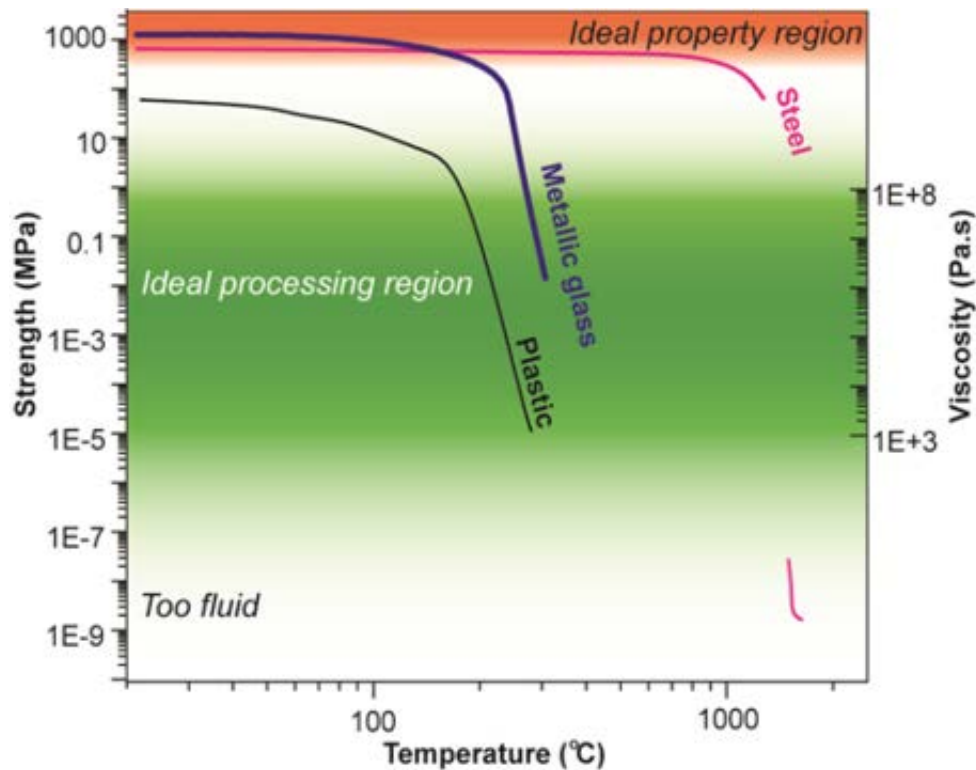


Figure 1.3: Strength versus temperature plot for steel, metallic glass and plastic. Above glass transition temperature (T_g), BMG softens to a viscous liquid and can be processed like plastic [9].

Due to this unique processing ability, BMGs are promising for a wide range of applications (Figure 1.4). High strength and toughness led to the first use of Zr-based metallic glasses in heads of golf clubs and few other sporting goods.

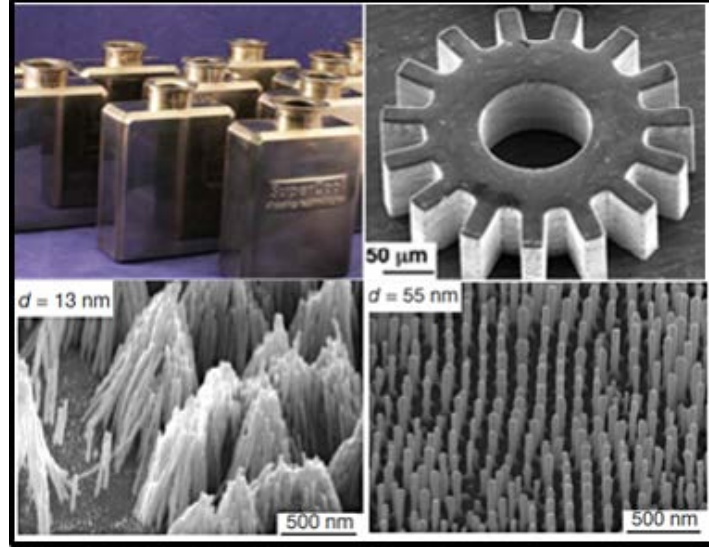


Figure 1.4: Macro- to nano-scale BMG fabricated by thermos-plastic forming [10].

Pd-based metallic glasses are used as a die material and electrode material. Some example of parts made of BMGs are shown in Figure 1.5.

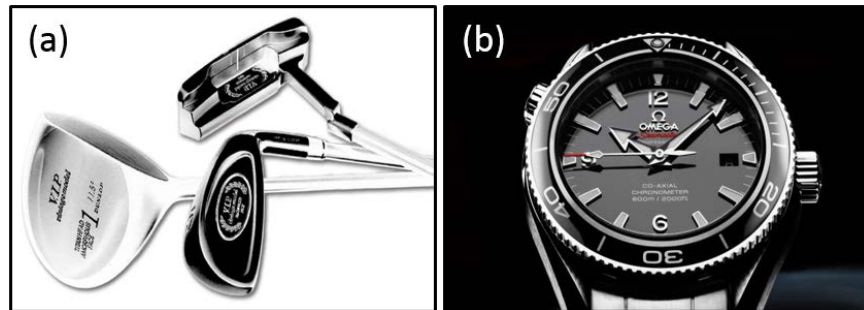


Figure 1.5: Application for BMGs: (a) Glof club head and (b) Omega watch components.

High hardness, superior wear, and scratch resistance of metallic glasses make them attractive for common gadgets such as cell phone cases or laptop cases. Metallic glasses could potentially replace brittle silicon dies for nano-imprint lithography as metallic glass nano-molds are easy to fabricate and are very durable. Better electronic, thermal and mechanical properties of BMGs compared to polymers make them good candidates to develop nano-composites for electronic application, such as electron field emission devices. High corrosion and wear resistance of BMGs

also make them promising for biomedical applications including hip/knee implants and surgical tools.

1.1.2. History of Bulk Metallic Glasses

In 1960, Duwez et al [11] first reported on vitrification of $\text{Au}_{75}\text{Si}_{25}$ binary alloy at a cooling rate of 10^6 K/s. In 1970, Chen et al [12] reported on a millimeter diameter amorphous rod of Pd-Cu-Si alloy using suction casting at a cooling rate of 10^3 K/s. In the 1980s, Turnbull reported the development of Pd-based metallic glass, $\text{Pd}_{40}\text{Ni}_{20}\text{P}_{20}$, with a diameter of 5mm [13,14]. Following these developments, BMGs with different compositions ($\text{La}_{55}\text{Al}_{25}\text{Ni}_{20}$; Mg-Ni-Y; Mg-Cu-Y) with critical casting thickness more than 5 mm have been made. Inoue's group contrived a family of Zr-Al-Ni-Cu alloys having high thermal stability and good glass forming ability. Production of these alloys initiated research interest in BMGs for engineering applications.

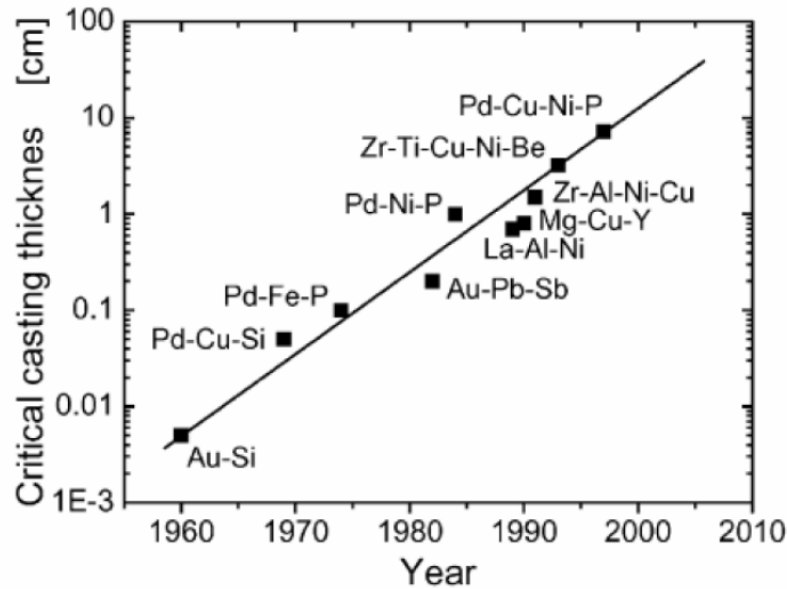


Figure 1.6: Critical casting thickness of different metallic glass alloy systems and the corresponding year they were reported [17]

Building upon Inoue's work, Johnson and his group developed Zr-Ti-Cu-Ni-Be alloy system with an unprecedented glass forming ability [15, 16]. One of the alloys from this Zirconium-based alloy

system with the nominal composition of $\text{Zr}_{41.2}\text{Ti}_{13.8}\text{Cu}_{12.5}\text{Ni}_{10}\text{Be}_{22.5}$ (Vitreloy1) was found to have a critical cooling rate as low as 1 K/s. Since this alloy has very low critical cooling rate, it can be synthesized into fully amorphous rod of 5-10 cm using conventional casting methods. Critical casting thickness versus the year of discovery of BMG is given in Figure 1.6.

1.1.3. Glass Formation

The fundamental difference between metallic glasses and crystalline metallic alloys is the atomic arrangement. Crystalline metals and alloys possess a periodic arrangement of atoms, whereas in metallic glasses the atomic arrangement is disordered, almost like liquids and does not show any long-range ordering. Figure 1.7 shows a periodic arrangement in crystalline material and disordered structure in an amorphous metal. Crystalline structure is thermodynamically stable configuration for metals, while amorphous structure is metastable.

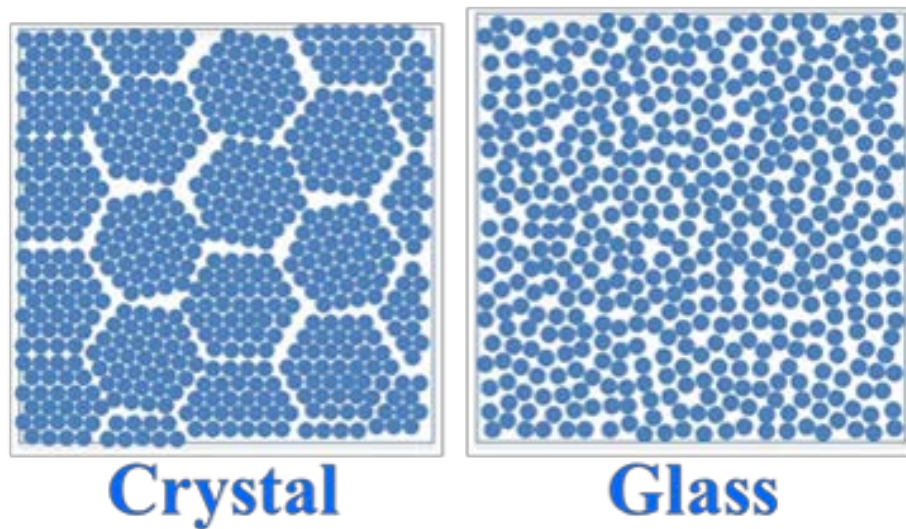


Figure 1.7: Schematic showing the periodic structure for a crystalline metal and disordered structure for glass.

Below its melting point, metallic alloy transforms to crystalline structure. However, the transformation does not happen instantly at melting temperature. It occurs by nucleation and growth processes. An appropriate driving force is required to overcome the activation barrier for

nucleation to occur as there is competition between volume and interfacial free energies. This driving force is provided by undercooling the melt (cooling the melt below its melting temperature (T_m)). Nucleation process involves formation of nuclei/embryos in the liquid melt. These embryos come together and form a cluster. Gradually these clusters grow and develop into a crystalline structure. The nucleation and growth processes require diffusion of atoms which depends on time and temperature. Thus, the crystallization process depends on time and temperature. The time-temperature relationship for crystal formation can be represented by a typical C-curve or TTT diagram (time-temperature-transformation diagram, Figure 1.8). The smallest time required for the crystal formation is represented by point “c” or nose of the TTT diagram (Figure 1.8).

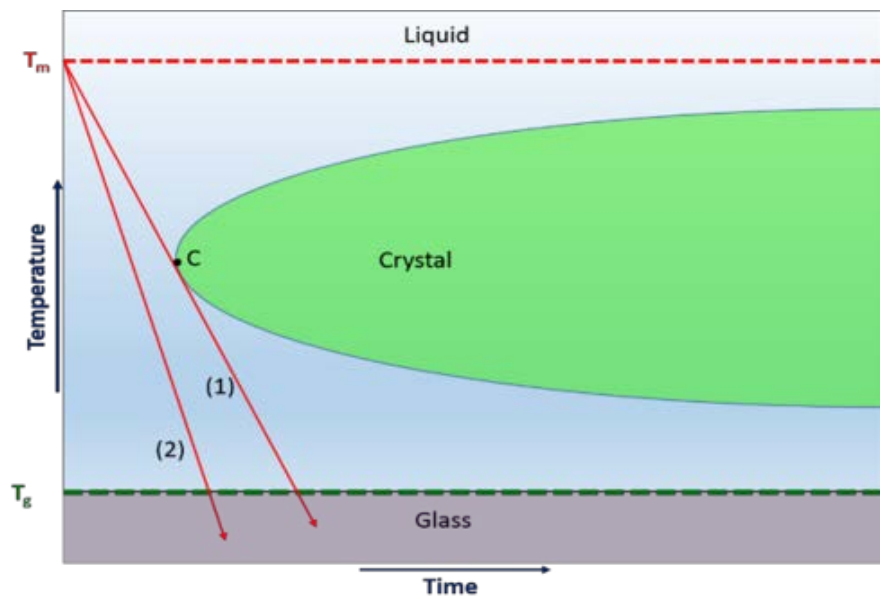


Figure 1.8: Schematic TTT Diagram. Liquid metal forms glassy structure when cooled with cooling rates higher than curve (1). Below T_g the liquid atoms fall out of equilibrium and are frozen in a random disordered phase known as “glass.”

Bypassing the nucleation and growth processes results in an amorphous structure. It is possible to avoid the nucleation and growth processes by using very high cooling rates. The cooling rate represented by curve 1 in Figure 1.8 gives the minimum critical cooling rate required for nucleation. Cooling the alloy at any higher cooling rate can suppress the nucleation process (e.g.

curve 2 in Figure 1.8). However, the requirement of such high cooling rates restricts the sample geometry [8]. The Turnbull group found similarities between metallic glass and nonmetallic glass and predicted the presence of T_g for metallic glass as well [12-14]. They proposed that the ratio of T_g and T_m ($T_{rg} = T_g/T_m$) could be used as a criterion for determining the glass forming ability of an alloy [15]. A liquid with $T_{rg} = 2/3$ becomes stable and is relatively easy to transform to a glass. This limiting condition for suppression of crystallization is used as rule of thumb in prediction of glass forming ability (GFA) of liquids [12,18-21]. The alloying elements also play an important role in GFA.

1.1.4. Devitrification Behavior

Since metallic glasses are metastable materials, they typically transform into corresponding equilibrium crystalline phases when exposed to high temperature for sufficient time. The temperature at which the glassy phase starts to transform to crystalline phase is referred as the crystallization temperature (T_x). Unlike melting point, T_x is not a thermodynamic parameter for a material as it depends on the heating rate. The crystallization temperature for a material increases for higher heating rates. Normally, T_g and T_x are measured using differential scanning calorimetry (DSC) technique. Crystallization of BMGs occurs by the nucleation and growth process. The driving force for the crystallization is the difference in free energy of the glassy phase and the corresponding crystalline phase. Devitrification can result in significant changes in microstructure and properties of metallic glasses [8].

1.1.5. Mechanical Behavior

Mechanical properties of amorphous metallic alloys have attracted fundamental scientific interest due to their unique features relative to other engineering materials. For instance, bulk metallic glasses show very high room temperature strength and exhibit similar elastic modulus

relative to other metallic alloys. We here put focus on overview of mechanical properties and more specific on fundamentals of deformation mechanisms.

In the amorphous metallic alloys, the bonding nature is metallic and hence accommodate strain at the atomic level. But, these alloys do not exhibit long range translation like crystalline materials. Deformation behavior in metallic glasses is not fully clear, however it is generally believed that deformation occur through local rearrangement of atoms which accommodate shear strain. Figure 1.9 shows one of such type of local rearrangement proposed by Argon and Kuo [22,23], which is based on atomic-analog bubble-raft model. Another model based on local atomic jump proposed by Spaepen [24].

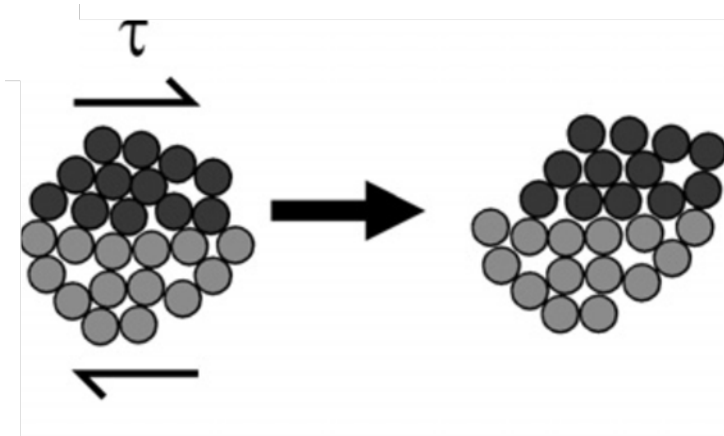


Figure 1.9: Two-dimensional schematic of atomistic deformation mechanism proposed on shear transformation zone, Argon model [23].

The event in the Figure 1.9 is commonly referred as shear transformation zone (STZ). STZ is local clusters of atoms and not structural defects like dislocations in a crystal defect. It is mainly defined as an event in a local volume and not a feature of the glass structure. Argon [23] developed first quantitative model of STZ and calculated the free energy as function of elastic constants

$$\Delta F_0 = \left[\frac{7 - 5\nu}{30(1 - \nu)} + \frac{2(1 + \nu)}{9(1 - \nu)} \beta^2 + \frac{1}{2\gamma_0} \frac{\tau_0}{\mu(T)} \right] \mu(T) \gamma_0^2 \Omega_0 \quad (1)$$

There is another commonly accepted deformation mechanism, which is based on the classical free-volume model proposed by Turnbull and co-workers [25,26]. Spaepen [24] proposed local atomic jump based on the free-volume concept (shown in Figure 1.10). It depicts the discrete atomic jumps near the zones of high free-volume. Further, deformation of bulk metallic glasses is regarded as competition among the different mechanisms, and it depends on the strain, temperature and microstructure.

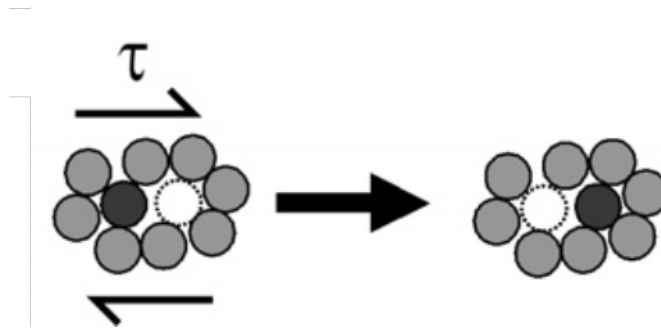


Figure 1.10: Two-dimensional schematic of atomistic deformation mechanism proposed on a local atomic jump, Spaepen [24].

1.1.5.1. Elastic Deformation

Amorphous alloys are speculated as elastically isotropic in nature and mainly having two independent elastic constants: Young's modulus (E) and Poisson's ratio (ν). However, bulk modulus (B) and shear modulus (μ) are more useful from fundamental point of view. Typically, bulk modulus of amorphous alloys is approximately 6 % smaller than crystalline alloys. However, comparison between crystalline and metallic glass is complicated due to complex microstructure of the crystallized metallic glass. Bulk modulus for crystalline materials increases with increase in curvature of interatomic potential and decreases with increase in equilibrium distance between atoms [27]. μ and E for amorphous alloys are approximately 30% lesser than corresponding crystals [28-32]. Weaire and co-workers [33] proposed that change in modulus depends on

rearrangements of atoms up on application of shear stresses. Simulations also confirm that internal rearrangements decrease the shear modulus by about 30% [33].

1.1.5.2. Plastic Deformation

The plastic deformation is accumulation of load strain generated by STZs and free volume redistribution. It can be homogenous or inhomogenous depending upon the temperature and strain rate.

1.1.5.2.1. Homogenous Plastic Flow

The homogenous plastic flow in metallic glasses occur at elevated temperature, near to the supercooled liquid regime. It can be assumed like viscous flow of supercooled fluid. It is classified in two types of flow, steady-state flow and non-steady-state flow.

1.1.5.2.2. Steady-State Flow

Homogenous flow under steady-state condition results from a balance between structural disordering and ordering or creation and annihilation of free volume. The activation of diffusive jump or STZ operation follows the rate law expression:

$$\dot{s} = v_0 \exp\left(-\frac{Q - \tau V}{kT}\right) \quad (2)$$

where, \dot{s} is the rate for occurrence of event under applied shear stress τ , Q is the characteristics activation energy, v_0 is the attempt frequency, k is the Boltzmann constant and T is the absolute temperature. The steady state uniaxial strain rate can be expressed as [25,34,35]

$$\dot{\epsilon} = \alpha'_0 v_0 \gamma_0 \exp\left(-\frac{Q}{kT}\right) \sinh\left(\frac{\sigma V}{\sqrt{3}kT}\right) \quad (3)$$

where, α'_0 is a modified constant.

Lu et al. [36] studied the steady-state homogenous flow for $Zr_{41.2}Ti_{13.8}Cu_{12.5}Ni_{10}Be_{22.5}$ metallic glass at elevated temperature. Figure 1.11 shows the data for $Zr_{41.2}Ti_{13.8}Cu_{12.5}Ni_{10}Be_{22.5}$ alloy at eight different temperatures, two of stresses and more than five decades of strain rate.

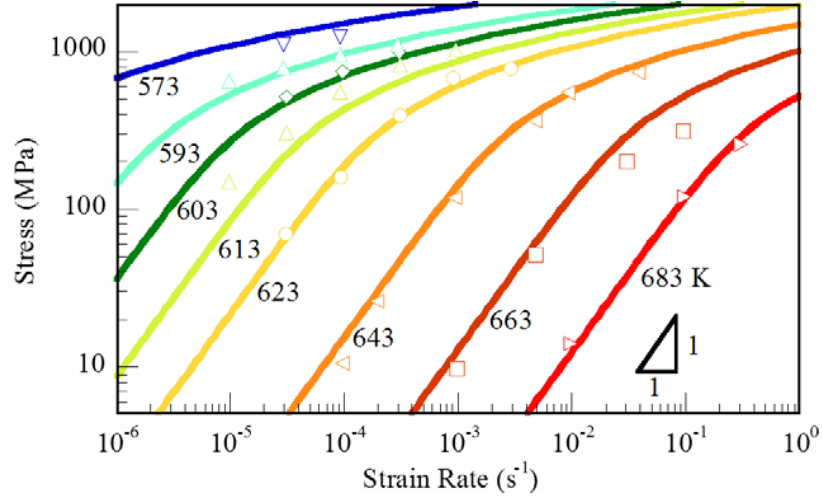


Figure 1.11: Steady-state homogenous flow data for $Zr_{41.2}Ti_{13.8}Cu_{12.5}Ni_{10}Be_{22.5}$ metallic glass at high temperatures [36].

In metallic glass, study of stress and strain rate-sensitivity in steady state flow is a topic of long-term interest. The strain rate can be expressed in power law

$$\dot{\gamma} = A\tau^n \quad (4)$$

where A is a temperature-dependent constant and n is the stress sensitivity.

Kawamura et al. [37] tested the $Pd_{40}Ni_{40}P_{20}$ metallic glass at different temperatures and strain rates. Figure 1.12 shows the 1260 % homogenous elongation at 620 K and $\dot{\epsilon} = 10^{-1}s^{-1}$. Further Nieh and Co-workers [38,39] reported the transition from Newtonian to non-Newtonian flow of $Zr_{52.5}Al_{10}Ti_5Cu_{17.9}Ni_{14.6}$ metallic glass at high strain rates. Through the TEM examination, they related the non-Newtonian flow to precipitation of nano-crystals. Nano-crystals during homogenous steady-state flow has also linked to strain hardening [40,41].

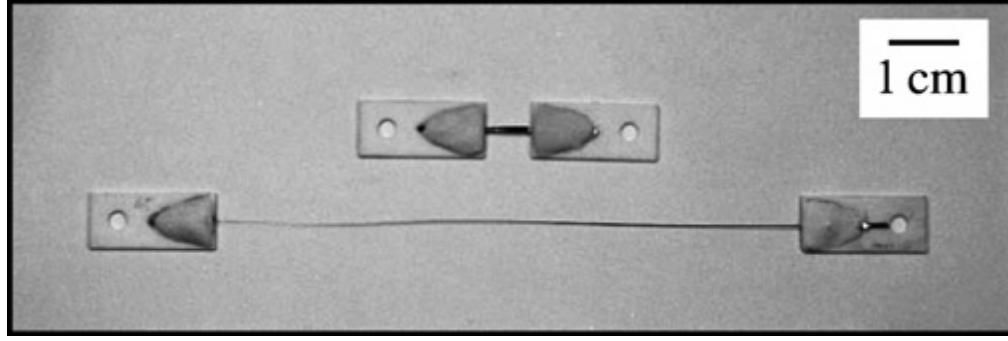


Figure 1.12: $Pd_{40}Ni_{40}P_{20}$ metallic glass wires before and after deformation at $T = 620\text{ K}$ and $\dot{\epsilon} = 10^{-1}\text{ s}^{-1}$ [36].

1.1.5.2.3. Non-Steady-State Flow

Homogenous flow under transient structural condition defined as non-steady-state flow. In non-steady-state flow, there is always net loss or gain of free volume during deformation. It is observed upon strain initiation from relaxed condition as shown in Figure 1.13 (a). Spaepen [24] predicted that overshoot occurs due to non-steady evolution of free volume. The stress undershoot can be observed (Figure 1.13 (b)) during rapid strain-rate change testing.

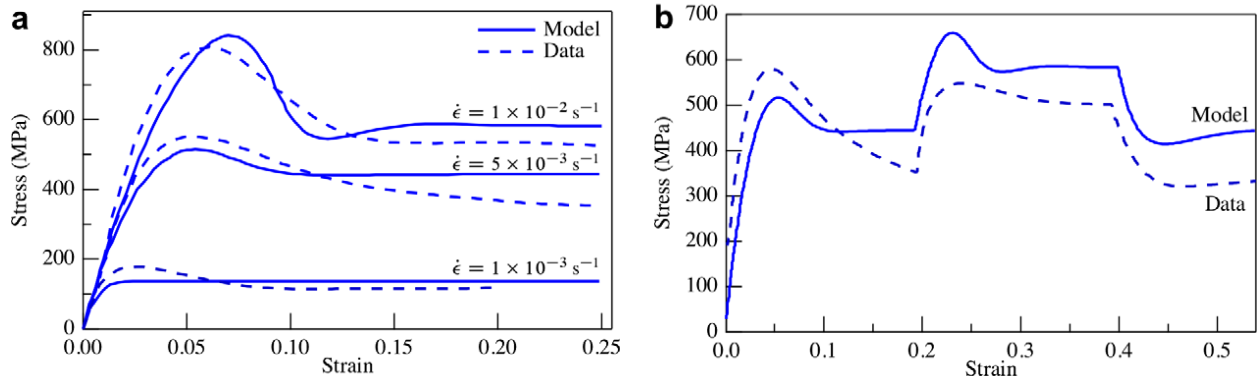


Figure 1.13: (a) Stress overshoot and (b) stress undershoot during strain rate change testing [24].

1.1.5.2.4. Inhomogeneous Flow

At very high stresses and lower temperatures, metallic glasses deform inhomogeneously via localization processes. It can be confirmed by the existence of cracking and shear banding during the deformation in metallic glass at high stress and low temperature.

1.1.5.3. Localization Processes

Shear localization is usually occurred as an outcome of strain softening phenomena. The main reasons for strain softening and localization are local production of free volume, local structural evolution, redistribution of internal stresses and local heat generation. Among these, local change in free volume and structural evolution are the dominant factors. Argon [23] proposed a one-dimensional model for the localization deformation flow, which occurred due to strain softening from accumulation of free volume (Figure 1.14 (a)). The shear band formation during inhomogenous deformation is mainly because of local perturbation in strain rate. Steif et al. [42] also developed one-dimensional model considering free volume concept (Figure 1.14 (b)).

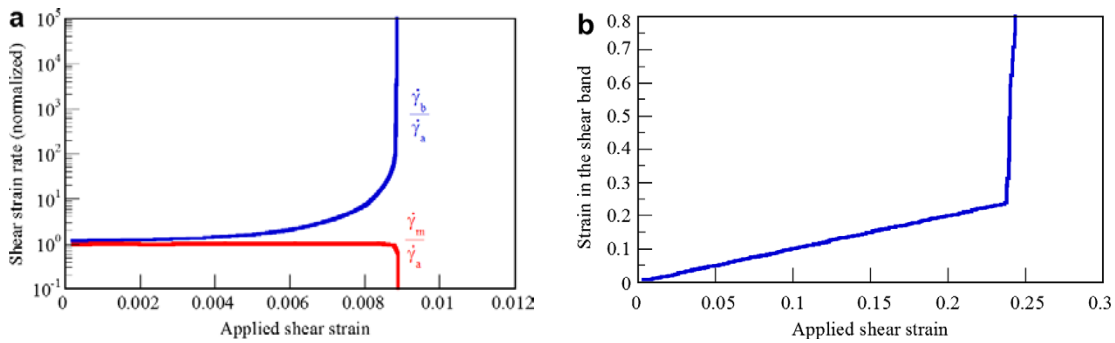


Figure 1.14: The process of strain localization and calculation from the work of (a) Argon [23] (b) Steif et al. [42].

Both the models follow same approach for inhomogenous flow: initially, elastic strain accommodate on application of stress until the stress level reaches a point where the local perturbation region generated and then strain accommodate in the local perturbed region which resulted in strain softening in the alloy. But, both models do not include the accommodation of decrease in deformation driving force and applied strain. Anand et al. [43] developed a finite-element model that capture multiaxial loading conditions and accommodate the applied strain. For the constrained loading, deformation flow is occurred through a series of shear banding events [44,45]. Therefore, shear localization is a critical and important area of research in metallic glass.

Another important discussion in field of the shear localization is thermal effect on it. Leamy and co-workers [46] proposed shear banding event as an adiabatic phenomenon. But this proposed theory was criticized by others [47,48].

1.1.5.4. Deformation Map

Spaepen was constructed a deformation map for metallic glass based on free-volume deformation concept [39]. Later it has been revisited by many authors [36,49,50]. Schuh et al. [47] reconstructed the deformation map incorporating recent observations in the field. Figure 1.15 (a) shows the stress-temperature deformation map. Figure 1.15 (b) depicts the strain rate-temperature deformation map [50]. The most important part of the map is transition line between homogenous steady-state flow to inhomogenous deformation, represented by thick solid line in the maps. This line is a boundary between two regimes, high temperature and low stress or strain rate regimes to low temperature and higher stress or strain rates. The homogenous regimes consist sub-regimes named elastic, Newtonian and non-Newtonian. In inhomogenous regimes at lower temperature, the glass strength is rate independent. The deformation map of metallic glasses provide the information of deformation behavior as a function of temperature, stress and strain rate and assumed unconstrained modes of loading.

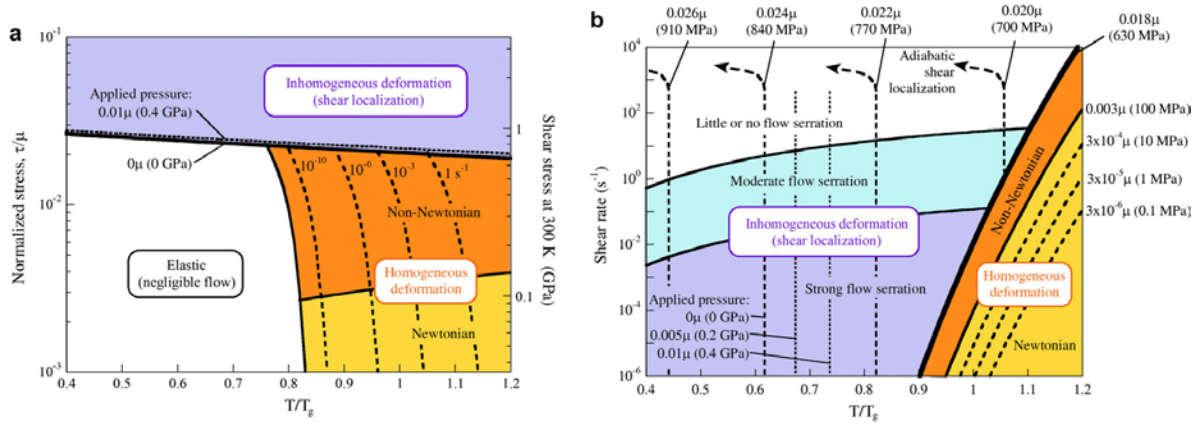


Figure 1.15: Deformation map of metallic glass: (a) stress-temperature and (b) strain rate-temperature [45,47,50].

1.2. Multi-Principal Element Alloys (MPEAs)

Conventional alloy design is based on a principal element and alloying addition to achieve a certain property. For example, steel is based on the principal element Fe while Ni-based super alloys are based on Ni. A new alloy design approach has recently emerged involving multiple principal elements instead of one dominant element [51]. Figure 1.16 shows the schematic of alloying approach in conventional and multi-principal element alloys (MPEAs) [52]. Several of these MPEAs form single phase solid solution which is attributed to high configurational entropy that suppresses the formation of intermetallic compounds. Numerous research has been done on these alloys in the recent decade. MPEAs possess exceptional properties compared to conventional alloys including superior strength and hardness, better wear and corrosion resistance, exceptional high temperature strength and stability.

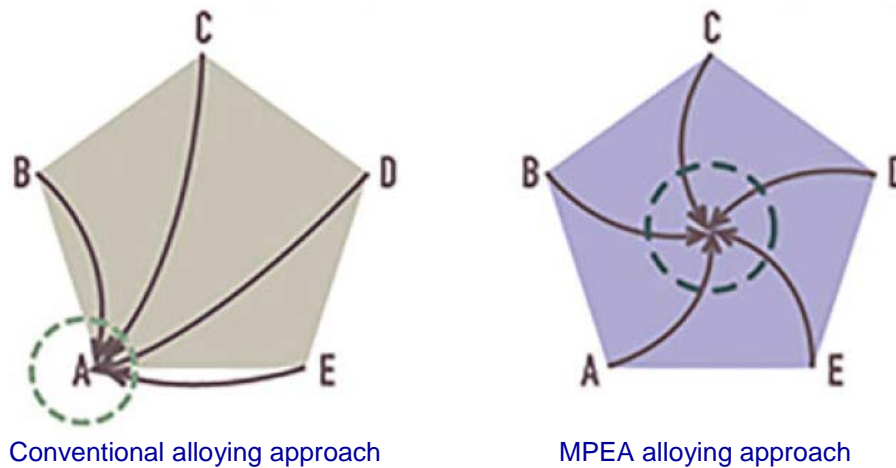


Figure 1.16: Schematic illustration of conventional alloying approach and MPEA alloying approach [52].

The single-phase MPEAs are often referred to as high entropy alloys (HEAs) as the higher configurational entropy is the major driving force for solid-solution formation [53]. These alloys typically consist of five or more elements with concentration between 5-35 at % [53,54]. In later years, it was found that solid-solution formation does not need to strictly follow these rules. Alloys

with $\Delta S_{conf} < R$ are typically referred to as low entropy alloys, $R < \Delta S_{conf} < 1.5R$ as medium entropy alloys and $\Delta S_{conf} > 1.5R$ as high entropy alloys. This entropy based definition also lead to some questions. The ΔS_{conf} calculated from Boltzman equation requires complete random arrangement of atoms in their lattice position which rarely occurs in metallic alloys. Recent research works also found ΔS_{conf} may not be solely responsible for solid solution, in fact enthalpy of formation ΔH also plays an important role in the formation of solid-solution.

1.2.1. Core Effects

MPEAs have most of the elements in equimolar or near equimolar proportions which leads to important effects in comparison to conventional alloys. These effects are termed as “core effects” as briefly described below.

1.2.1.1. High Entropy Effect

The presence of multi-principal elements in a disordered way increases the configurational entropy of MPEAs and therefore lowers the free energy of solid solution phases and suppress the intermetallic phases, especially at higher temperatures. The overall degree of order in MPEAs decreases with increasing temperature. Therefore, some ordered phases in MPEAs, which form during casting, can transform to random solid solution at elevated temperature. There is the possibility of the presence of intermetallic compounds only if enthalpy formation is large enough to suppress the entropy effect at high temperature. Various studies report the existence of high entropy effect [55-61]. Figure 1.17 depicts XRD patterns of binary to seven component alloys, which demonstrates the entropy effect [62].

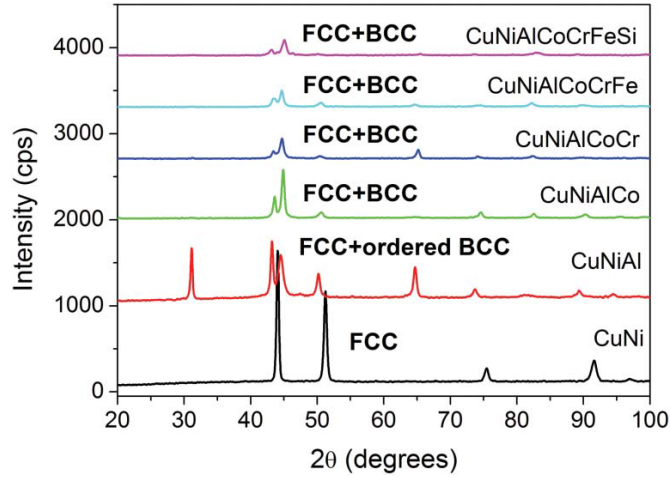


Figure 1.17: XRD patterns of binary to septenary alloys [62].

However, the presence of intermetallic compounds in MPEAs have been reported by various researchers [53,63] and these intermediate phases also lead to good properties in MPEAs.

1.2.1.2. Sluggish Diffusion Effect

It has been hypothesized by several group that the kinetics for diffusion and phase transformation in MPEAs are slower in comparison to corresponding conventional alloys [64]. Two aspects are important to understand this effect. The first one, in multi-principal elements alloys, neighboring atoms of each lattice site are different unlike conventional alloys. Therefore, neighboring atoms before and after the jump into vacancy are different and it generates different atomic configurations, which results in different local-energy sites. This process hinders the diffusion process. Figure 1.18 shows diffusion of Ni atom in pure metal, Fe-Cr-Ni and CoCrFeMn_{0.5}Ni alloy. In CoCrFeMn_{0.5}Ni alloy, the diffusion of Ni atom is slowest [65].

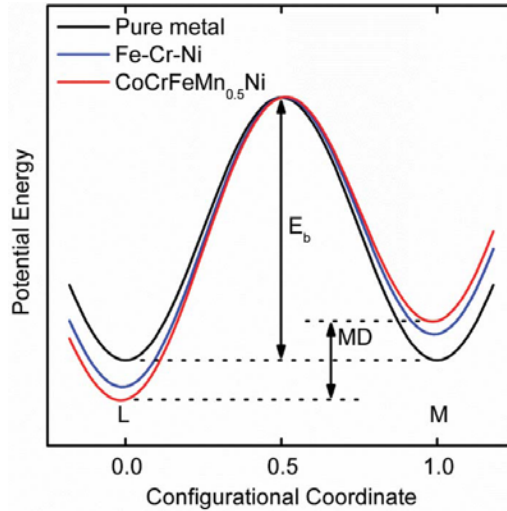


Figure 1.18: Schematic of potential energy change for migration in Ni atom in pure metal, Fe-Cr-Ni and CoCrFeMn_{0.5}Ni alloy [65].

Secondly, unlike conventional alloys, diffusion rate of each element in MPEA is different. The jumping rate of atoms to vacancies are different and thus rate determining step for phase transformation is diffusion of slowest-moving elements. The sluggish diffusion in multi-principal elements alloys allow supersaturated state and nano-precipitates, which lead to better performance of MPEAs.

But these hypothesis is mostly based on secondary observation. Formation of nano-crystalline structure and their retention of nano-crystalline structure on few system, were interpreted to indicate slow diffusion rate [1,66,67]. To support the slow diffusion rate the data available for only one alloy system. Few researcher indicated, the closer observation of the results on this respects might not have significantly different diffusion rate if they are normalized with melting temperature and questioned this hypothesis [1]. Again these hypothesis is based on very few limited study and addition work is required to test this assumption

1.2.1.3. Lattice Distortion Effect

MPEAs lattice consists of various elements with different size. The larger size atoms push

neighboring sites and smaller size atoms will have more space near the vicinity. These size differences give rise to lattice distortion. Figure 1.19 illustrates the schematic of single element FCC structure and distorted lattice structure of MPEAs [68][52]. The associated strain energy of MPEAs increase due to lattice distortion and this hinders the dislocation movement and contribute to solid solution strengthening. Lattice distortion also increases the scattering of propagating electrons and phonons, which lowers the electrical and thermal conductivity [69].

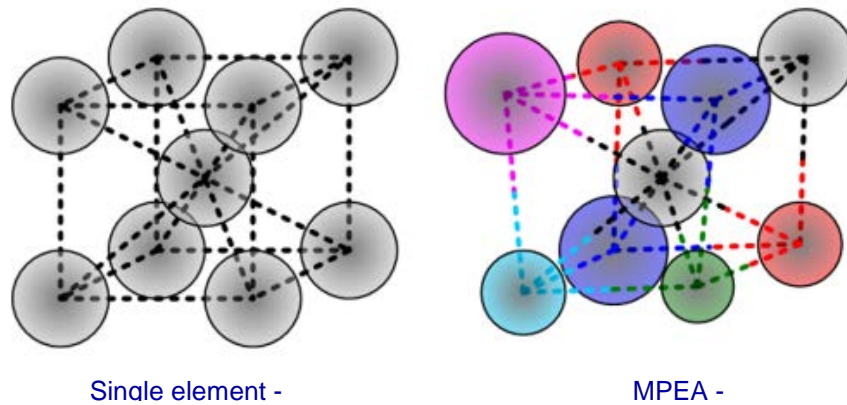


Figure 1.19: Schematic illustration of FCC structure of single element (left) and distorted FCC structure of MPEA (right) [68].

1.2.1.4. Cocktail Effect

The properties of MPEAs are related to their constituent elements but it is not merely the average value. The interaction among component elements needs to be accounted for in determining the properties of MPEAs. For instance, addition of soft and low-melting point Al increases the hardness of the MPEAs. Figure 1.20 depicts the hardness of $\text{Al}_x\text{CoCrCuFeNi}$ alloy as a function of Al content [62]. It reveals that increasing the Al content in the alloy increases the hardness. This occurs due to two reasons: (i) formation of hard BCC phase and (ii) cohesive bonding between Al and other elements.

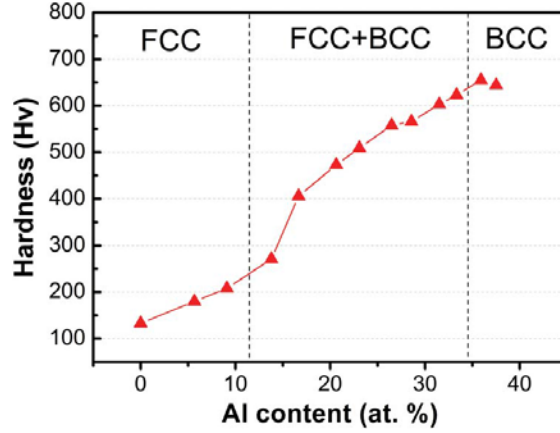


Figure 1.20: Hardness of $Al_xCoCrCuFeNi$ alloy as a function of Al content [62].

1.2.2. Enthalpy of Formation

It has been shown by many researchers that not only ΔS_{conf} but ΔH also plays an important role in formation of solid solution. Following conditions need to be fulfilled simultaneously for formation of single phase solid solution:

$$-22 \leq \Delta H_{mix} \leq 7 \text{ kJmol}, \delta \leq 8.5 \text{ and } 11 \leq \Delta S_{mix} \leq 19.5 \text{ J(Kmol)} \quad (5)$$

where ΔH_{mix} is enthalpy of mixing, ΔS_{mix} is entropy of mixing and δ is atomic size differences.

ΔH_{mix} needs to be optimum as $+\Delta H_{mix}$ will lead to phase separation and $-\Delta H_{mix}$ will help in formation of intermetallic compounds. δ need to be small enough so that strain energy is small to stabilize the solid solution phase. ΔS_{mix} needs to be large to stabilize the single phase.

1.3. Thesis Overview

Bulk metallic glasses and multi-principal element alloys (consisting of multiple principal elements) represent relatively new classes of multi-component engineering materials designed for satisfying multiple functionalities simultaneously. Correlating the microstructure with mechanical behavior (*at the microstructural length-scales*) in these materials is key to understanding their performance. In this study, the structure evolution and nano-mechanical behavior of these two

classes of materials was investigated with the objective of fundamental scientific understanding of their properties.

This dissertation is divided into eight chapters. Chapter 1 presents the introduction of bulk metallic glasses and multi-principal element alloys. The criteria for formation of these materials was discussed along with the thermodynamics and kinetic factors affecting their stability.

Chapter 2 provides experimental details of different characterization techniques including XRD, DSC, SEM, EBSD, TEM, 3DAP, nano-indentation and pico-indentation.

The structure evolution and high temperature nano-mechanical behavior during devitrification of $\text{Zr}_{41.2}\text{Ti}_{13.8}\text{Cu}_{12.5}\text{Ni}_{10.0}\text{Be}_{22}$ (Vitreloy1) are discussed in chapter 3. Devitrification was found to proceed via primary nucleation of a metastable icosahedral phase followed by eutectic mode of crystallization in the remaining supercooled liquid. The *i-phase* showed a slight increase in hardness as compared to the glass. After devitrification, the hardness increased significantly due to nano-sized grains and intermetallic compound formation.

In chapter 4, the structure evolution in two catalytic amorphous alloys, $\text{Pt}_{57.5}\text{Cu}_{14.7}\text{Ni}_{5.3}\text{P}_{22.5}$ and $\text{Pd}_{43}\text{Cu}_{27}\text{Ni}_{10}\text{P}_{20}$, are discussed. The distribution of atoms was obtained for the as-cast amorphous (metastable) state and the corresponding (thermodynamically stable) devitrified state. Owing to its atomic-scale resolution, 3DAP technique was used to identify nanometer-scale composition fluctuations and the interface between the different phases upon devitrification of the metallic glasses.

Chapter 5 is related to the high temperature nano-mechanical creep activation energy of two Zr based bulk metallic glasses $\text{Zr}_{41.2}\text{Ti}_{13.8}\text{Cu}_{12.5}\text{Ni}_{10.0}\text{Be}_{22}$ (Vitreloy1) and $\text{Zr}_{52.5}\text{Ti}_5\text{Cu}_{17.9}\text{Ni}_{14.6}\text{Al}_{10}$ (Vitreloy105). In the low temperature range, activation energy for creep

was found to be dictated by cooperative migration of atomic clusters while self-diffusion of atoms dominated the creep deformation at high temperatures.

Chapter 6 focuses on strain gradient plasticity of two equiatomic multi-principal element alloys namely CoCrNi and CoCrFeMnNi.

Chapter 7 discusses dislocation nucleation in multi-principal alloys namely CoCrNi, CoCrFeMnNi, and $\text{Al}_{0.1}\text{CoCrFeNi}$ and Ni.

Chapter 8 deals with the strain rate sensitivity of nanocrystalline $\text{Al}_{0.1}\text{CoCrFeNi}$ alloy, which was determined by *in situ* compression of nano-pillars in a Pico-indenter.

1.4. References

- [1] D. Miracle, O. Senkov, A critical review of high entropy alloys and related concepts, *Acta Materialia*. 122 (2017) 448-511.
- [2] A. Takeuchi, K. Amiya, T. Wada, K. Yubuta, W. Zhang, A. Makino, Entropies in alloy design for high-entropy and bulk glassy alloys, *Entropy*. 15 (2013) 3810-3821.
- [3] A. Inoue, A. Takeuchi, Recent development and application products of bulk glassy alloys, *Acta Materialia*. 59 (2011) 2243-2267.
- [4] D. Xu, B. Lohwongwatana, G. Duan, W.L. Johnson, C. Garland, Bulk metallic glass formation in binary Cu-rich alloy series—Cu 100— x Zr x (x= 34, 36, 38.2, 40 at.%) and mechanical properties of bulk Cu 64 Zr 36 glass, *Acta Materialia*. 52 (2004) 2621-2624.
- [5] D. Wang, Y. Li, B. Sun, M. Sui, K. Lu, E. Ma, Bulk metallic glass formation in the binary Cu—Zr system, *Appl. Phys. Lett.* 84 (2004) 4029-4031.
- [6] L. Xia, W. Li, S. Fang, B. Wei, Y. Dong, Binary Ni—Nb bulk metallic glasses. (2006).
- [7] S. Mukherjee, Study of crystallization behavior, kinetics and thermodynamics of bulk metallic glasses using noncontact electrostatic levitation technique. (2005).
- [8] C. Suryanarayana, A. Inoue, *Bulk Metallic Glasses*, CRC press Boca Raton, FL, 2011.
- [9] J. Schroers, Processing of bulk metallic glass, *Adv Mater.* 22 (2010) 1566-1597.
- [10] G. Kumar, H.X. Tang, J. Schroers, Nanomoulding with amorphous metals, *Nature*. 457 (2009) 868-872.
- [11] W. Klement, R. Willens, P. Duwez, Non-crystalline structure in solidified gold—silicon alloys, *Nature*. 187 (1960) 869-870.
- [12] H. Chen, D. Turnbull, Formation, stability and structure of palladium-silicon based alloy glasses, *Acta metallurgica*. 17 (1969) 1021-1031.

- [13] A. Inoue, T. Zhang, T. Masumoto, Al–La–Ni amorphous alloys with a wide supercooled liquid region, *Mater. Trans. JIM*. 30 (1989) 965-972.
- [14] A. Inoue, A. Kato, T. Zhang, S. Kim, T. Masumoto, Mg–Cu–Y amorphous alloys with high mechanical strengths produced by a metallic mold casting method, *Mater. Trans. JIM*. 32 (1991) 609-616.
- [15] A. Peker, W.L. Johnson, A highly processable metallic glass: Zr₄₁. 2Ti₁₃. 8Cu₁₂. 5Ni₁₀. 0Be₂₂. 5, *Appl. Phys. Lett.* 63 (1993) 2342-2344.
- [16] X. Lin, W. Johnson, Formation of Ti–Zr–Cu–Ni bulk metallic glasses, *J. Appl. Phys.* 78 (1995) 6514-6519.
- [17] J.F. Löffler, Bulk metallic glasses, *Intermetallics*. 11 (2003) 529-540.
- [18] D. Turnbull, THE 1961 INSTITUTE OF METALS DIVISION LECTURE-THE LIQUID STATE AND THE LIQUID-SOLID TRANSITION. (1961).
- [19] H. Chen, D. Turnbull, Evidence of a glass–liquid transition in a gold–germanium–silicon alloy, *J. Chem. Phys.* 48 (1968) 2560-2571.
- [20] D. Turnbull, J.C. Fisher, Rate of nucleation in condensed systems, *J. Chem. Phys.* 17 (1949) 71-73.
- [21] W.L. Johnson, Bulk glass-forming metallic alloys: Science and technology, *MRS Bull.* 24 (1999) 42-56.
- [22] A. Argon, H. Kuo, Plastic flow in a disordered bubble raft (an analog of a metallic glass), *Materials science and Engineering*. 39 (1979) 101-109.
- [23] A. Argon, Plastic deformation in metallic glasses, *Acta metallurgica*. 27 (1979) 47-58.
- [24] F. Spaepen, A microscopic mechanism for steady state inhomogeneous flow in metallic glasses, *Acta metallurgica*. 25 (1977) 407-415.
- [25] M.H. Cohen, D. Turnbull, Molecular transport in liquids and glasses, *J. Chem. Phys.* 31 (1959) 1164-1169.
- [26] D. Polk, D. Turnbull, Flow of melt and glass forms of metallic alloys, *Acta Metallurgica*. 20 (1972) 493-498.
- [27] T.H. Courtney, *Mechanical Behavior of Materials*, Waveland Press, 2005.
- [28] H. Künzi, Glassy Metals II, *Topics in Applied Physics*. 53 (1983) 169.
- [29] S. Jovanovic, C.S. Smith, Elastic modulus of amorphous nickel films, *J. Appl. Phys.* 32 (1961) 121-122.
- [30] M. Ashby, A. Nelson, R. Centamore, The mechanical properties of a glassy metal; Ni₃P, *Scripta Metallurgica*. 4 (1970) 715-717.
- [31] T. Masumoto, R. Maddin, The mechanical properties of palladium 20 at/o silicon alloy quenched from the liquid state, *Acta metallurgica*. 19 (1971) 725-741.

- [32] B. Golding, B. Bagley, F. Hsu, Soft transverse phonons in a metallic glass, *Phys. Rev. Lett.* 29 (1972) 68.
- [33] D. Weaire, M. Ashby, J. Logan, M. Weins, On the use of pair potentials to calculate the properties of amorphous metals, *Acta Metallurgica*. 19 (1971) 779-788.
- [34] X. Fu, Y. Li, C. Schuh, Contributions to the homogeneous plastic flow of in situ metallic glass matrix composites, *Appl. Phys. Lett.* 87 (2005) 241904.
- [35] M. Bletry, P. Guyot, Y. Brechet, J. Blandin, J. Soubeyroux, Homogeneous deformation of bulk metallic glasses in the super-cooled liquid state, *Materials Science and Engineering: A*. 387 (2004) 1005-1011.
- [36] J. Lu, G. Ravichandran, W.L. Johnson, Deformation behavior of the Zr 41.2 Ti 13.8 Cu 12.5 Ni 10 Be 22.5 bulk metallic glass over a wide range of strain-rates and temperatures, *Acta materialia*. 51 (2003) 3429-3443.
- [37] Y. Kawamura, T. Nakamura, A. Inoue, Superplasticity in Pd 40 Ni 40 P 20 metallic glass, *Scr. Mater.* 39 (1998) 301-306.
- [38] T. Nieh, J. Wadsworth, C. Liu, T. Ohkubo, Y. Hirotsu, Plasticity and structural instability in a bulk metallic glass deformed in the supercooled liquid region, *Acta Materialia*. 49 (2001) 2887-2896.
- [39] T. Nieh, C. Schuh, J. Wadsworth, Y. Li, Strain rate-dependent deformation in bulk metallic glasses, *Intermetallics*. 10 (2002) 1177-1182.
- [40] D. Bae, H. Lim, S. Kim, D. Kim, W. Kim, Mechanical behavior of a bulk Cu-Ti-Zr-Ni-Si-Sn metallic glass forming nano-crystal aggregate bands during deformation in the supercooled liquid region, *Acta materialia*. 50 (2002) 1749-1759.
- [41] H. Jeong, W. Kim, Hardening by Crystallization During Superplastic Flow in a Powder-metallurgy-processed Zr 65 Al 10 Ni 10 Cu 15 Glass Metallic Alloy, *J. Mater. Res.* 20 (2005) 1447-1455.
- [42] P. Steif, F. Spaepen, J. Hutchinson, Strain localization in amorphous metals, *Acta Metallurgica*. 30 (1982) 447-455.
- [43] L. Anand, C. Su, A theory for amorphous viscoplastic materials undergoing finite deformations, with application to metallic glasses, *J. Mech. Phys. Solids*. 53 (2005) 1362-1396.
- [44] C. Schuh, A. Argon, T. Nieh, J. Wadsworth, The transition from localized to homogeneous plasticity during nanoindentation of an amorphous metal, *Philosophical Magazine*. 83 (2003) 2585-2597.
- [45] R. Conner, W.L. Johnson, N. Paton, W. Nix, Shear bands and cracking of metallic glass plates in bending, *J. Appl. Phys.* 94 (2003) 904-911.
- [46] H. Leamy, T. Wang, H. Chen, Plastic flow and fracture of metallic glass, *Metallurgical Transactions*. 3 (1972) 699-708.
- [47] C.A. Schuh, T.C. Hufnagel, U. Ramamurty, Mechanical behavior of amorphous alloys, *Acta Materialia*. 55 (2007) 4067-4109.

- [48] C.A. Pampillo, Flow and fracture in amorphous alloys, *J. Mater. Sci.* 10 (1975) 1194-1227.
- [49] C.A. Schuh, A.C. Lund, T. Nieh, New regime of homogeneous flow in the deformation map of metallic glasses: elevated temperature nanoindentation experiments and mechanistic modeling, *Acta Materialia*. 52 (2004) 5879-5891.
- [50] J. Megusar, A. Argon, N. Grant, Plastic flow and fracture in Pd 80 Si 20 near T_g , *Materials Science and Engineering*. 38 (1979) 63-72.
- [51] K. Huang, J. Yeh, A study on the multicomponent alloy systems containing equal-mole elements, Hsinchu: National Tsing Hua University. (1996).
- [52] R. Mishra, N. Kumar, M. Komarasamy, Lattice strain framework for plastic deformation in complex concentrated alloys including high entropy alloys, *Materials Science and Technology*. 31 (2015) 1259-1263.
- [53] J. Yeh, S. Chen, S. Lin, J. Gan, T. Chin, T. Shun, C. Tsau, S. Chang, Nanostructured high-entropy alloys with multiple principal elements: novel alloy design concepts and outcomes, *Advanced Engineering Materials*. 6 (2004) 299-303.
- [54] Y. Jien-Wei, Recent progress in high entropy alloys, *Ann.Chim.Sci.Mat.* 31 (2006) 633-648.
- [55] C. Tong, M. Chen, J. Yeh, S. Lin, S. Chen, T. Shun, S. Chang, Mechanical performance of the $Al_xCoCrCuFeNi$ high-entropy alloy system with multiprincipal elements, *Metallurgical and Materials Transactions A*. 36 (2005) 1263-1271.
- [56] C. Tong, Y. Chen, J. Yeh, S. Lin, S. Chen, T. Shun, C. Tsau, S. Chang, Microstructure characterization of $Al_xCoCrCuFeNi$ high-entropy alloy system with multiprincipal elements, *Metallurgical and Materials Transactions A*. 36 (2005) 881-893.
- [57] L. Anmin, X. Zhang, Thermodynamic analysis of the simple microstructure of $AlCrFeNiCu$ high-entropy alloy with multi-principal elements, *Acta Metallurgica Sinica (English Letters)*. 22 (2009) 219-224.
- [58] O. Senkov, G. Wilks, D. Miracle, C. Chuang, P. Liaw, Refractory high-entropy alloys, *Intermetallics*. 18 (2010) 1758-1765.
- [59] M.F. del Grosso, G. Bozzolo, H.O. Mosca, Determination of the transition to the high entropy regime for alloys of refractory elements, *J. Alloys Compounds*. 534 (2012) 25-31.
- [60] C. Ng, S. Guo, J. Luan, S. Shi, C.T. Liu, Entropy-driven phase stability and slow diffusion kinetics in an $Al_{0.5}CoCrCuFeNi$ high entropy alloy, *Intermetallics*. 31 (2012) 165-172.
- [61] M. Lucas, G. Wilks, L. Mauger, J.A. Munoz, O. Senkov, E. Michel, J. Horwath, S. Semiatin, M.B. Stone, D.L. Abernathy, Absence of long-range chemical ordering in equimolar $FeCoCrNi$, *Appl. Phys. Lett.* 100 (2012) 251907.
- [62] M. Tsai, J. Yeh, High-entropy alloys: a critical review, *Materials Research Letters*. 2 (2014) 107-123.
- [63] C. Hsu, J. Yeh, S. Chen, T. Shun, Wear resistance and high-temperature compression strength of $Fcc\ CuCoNiCrAl_{0.5}Fe$ alloy with boron addition, *Metallurgical and Materials Transactions A*. 35 (2004) 1465-1469.

- [64] K. Cheng, C. Lai, S. Lin, J. Yeh, Recent progress in multi-element alloy and nitride coatings sputtered from high-entropy alloy targets, 31 (2006) 723-736.
- [65] K. Tsai, M. Tsai, J. Yeh, Sluggish diffusion in Co–Cr–Fe–Mn–Ni high-entropy alloys, *Acta Materialia*. 61 (2013) 4887-4897.
- [66] C. Ng, S. Guo, J. Luan, S. Shi, C.T. Liu, Entropy-driven phase stability and slow diffusion kinetics in an Al 0.5 CoCrCuFeNi high entropy alloy, *Intermetallics*. 31 (2012) 165-172.
- [67] M. Tsai, J. Yeh, J. Gan, Diffusion barrier properties of AlMoNbSiTaTiVZr high-entropy alloy layer between copper and silicon, *Thin Solid Films*. 516 (2008) 5527-5530.
- [68] S.Y. Chang, C.E. Li, Y.C. Huang, H.F. Hsu, J.W. Yeh, S.J. Lin, Structural and thermodynamic factors of suppressed interdiffusion kinetics in multi-component high-entropy materials, *Sci. Rep.* 4 (2014) 4162.
- [69] M. Tsai, Physical properties of high entropy alloys, *Entropy*. 15 (2013) 5338-5345.

CHAPTER 2

EXPERIMENTAL TECHNIQUES

For the structure evolution of BMGs and MPEAs, X-ray diffraction (XRD) was used in combination with advanced microscopy including Scanning Electron Microscopy (SEM), Transmission Electron Microscopy (TEM), and 3D Atom Probe Microscopy (3DAP). Nano-mechanical behavior was evaluated using Hysitron Nano-indenter with XSol600 heating stage for high temperature testing and creep. The working principles of the used experimental techniques are briefly described in the following sections.

2.1. X-Ray Diffraction (XRD)

X-Ray diffraction were performed in Rigaku Ultima III diffractometer with Cu-K α of 1.5418 Å wavelength. XRD studies were performed for phase identification and determination of lattice parameter for alloys. An operating voltage of 40 kV and operating current of 44 mA was maintained during XRD experiment. The data acquisition during the experiment was done in a 2θ range of 20° - 90° with a step size of 0.01° . Crystal structure and crystal lattice were determined using Bragg's law: $2d\sin\theta = n\lambda$, d is the inter planar spacing, n is the order of reflection in integer, λ is the wavelength, and θ is the incident angle. The principle of XRD and Bragg's law is shown in Figure 2.1.

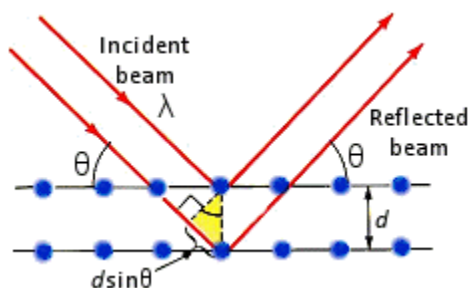


Figure 2.1: Bragg's law and principle of x-ray diffraction.

2.2. Differential Scanning Calorimetry (DSC)

Differential scanning calorimetry is technique to measure heat capacities. Measurement of enthalpy changes for phase transition can easily be calculated. All the transition temperatures (by glass transition temperature (T_g) and crystallization temperature (T_x) were determined using DSC, Netzsch. Figure 2.2 shows the inside view of DSC system.

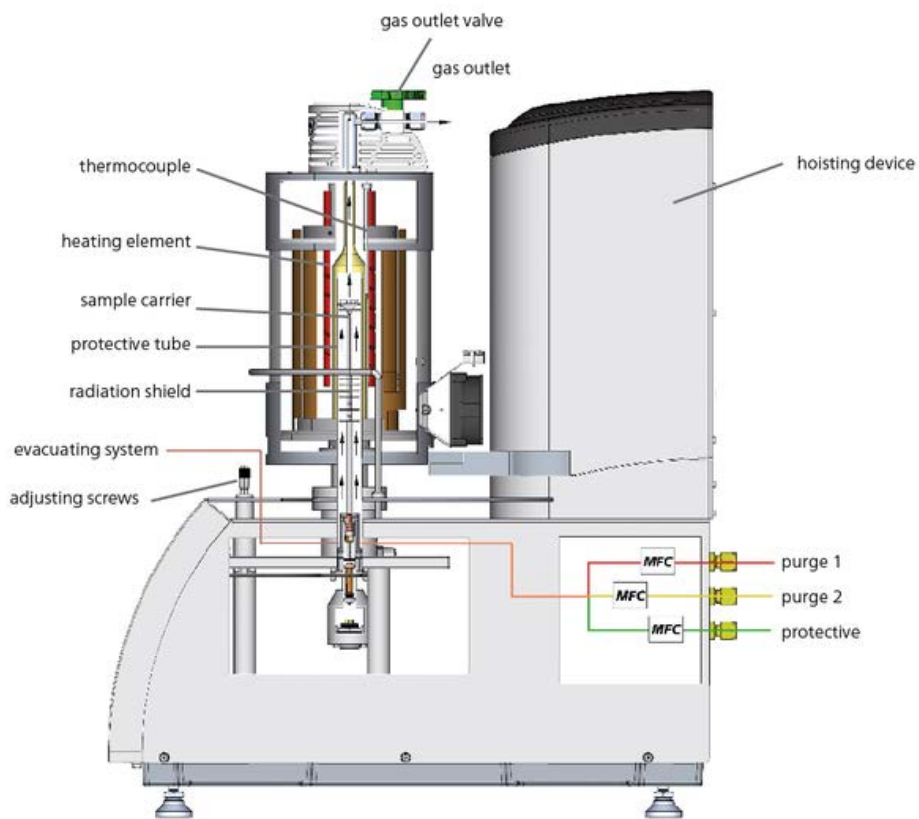


Figure 2.2: Inside view of differential scanning calorimeter.

2.3. Scanning Electron Microscopy (SEM)

Quanta 200 environmental scanning electron microscope (ESEM) was used for SEM micrographs. It has a tungsten filament based electron column and equipped with Everhardt Thornely secondary electron detectors (ETD), charged couple detectors (CCD), detachable solid

state scatter electron detectors (BSED) and SiLi energy dispersive spectrometer detectors (EDS) for the surface analysis. The size scale was measured using BSED. The EDS is used for the compositional analysis of the alloys.

2.4. Electron Backscatter Diffraction (EBSD)

The grain orientation studies were carried out using EBSD detector in FEI Nova Nano SEM 230 TM. The sample is placed on 700 tilted holder and then inserted inside the chamber with care. Figure 2.3 shows the schematic of the EBSD set up. The data acquisition was carried out using OIM data collection software. Further, analysis of data was carried out using TSL OIM Data Analysis 5.3 software.

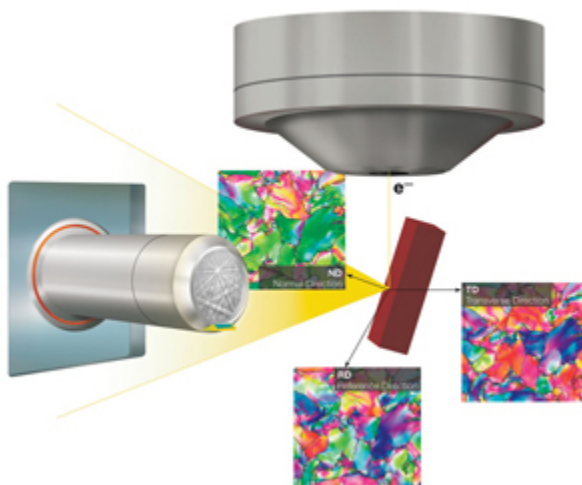


Figure 2.3: Schematic of EBSD set up.

2.5. Focused Ion Beam (FIB)

FEI Nova 200 NanoLab focused ion beam microscope was used for transmission electron microscopy (TEM) and atom probe tomography (APT) sample preparation. The FIB system is equipped with an Omniprobe Autoprobe TM nano manipulator and gas injection system to deposit platinum. It consists a field emission electron gun (FEG) column and a gallium (Ga) ion beam source. Figure 2.4 shows the schematic of FIB system and principle of FIB. The electron beam

column is perpendicular to the sample and Ga ion beam is kept at 52° angle to the normal of the sample surface.

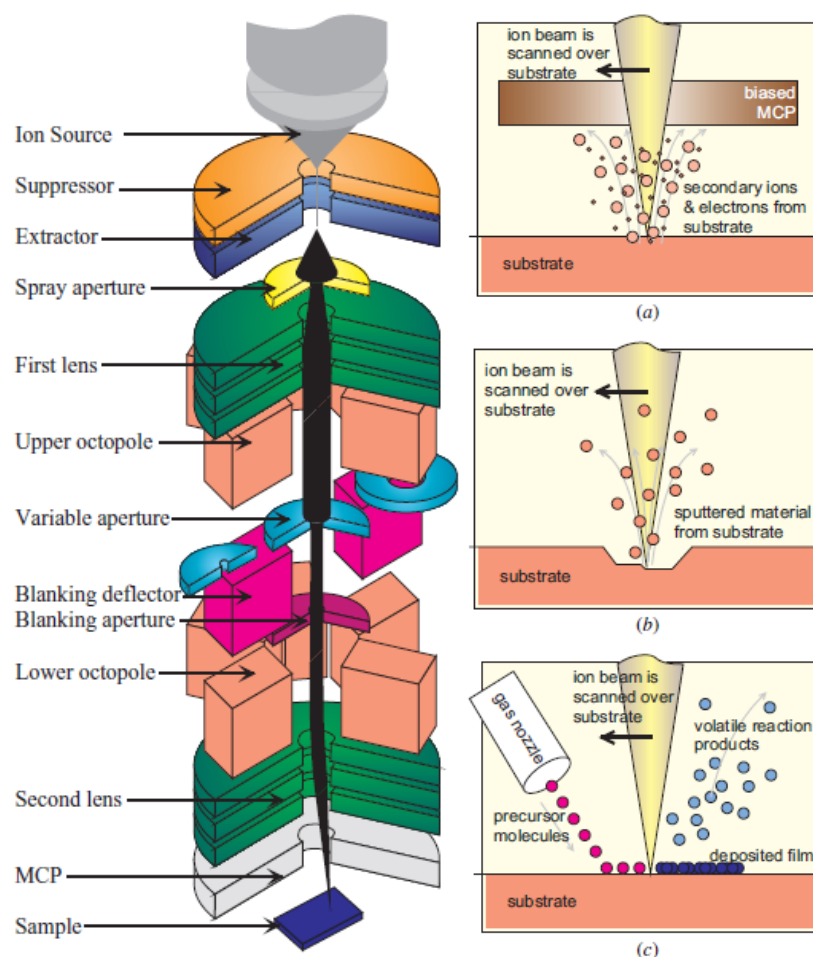


Figure 2.4: Schematic of FIB system and principles of FIB including: (a) Imaging, (b) Milling, and (c) Deposition

2.6. Transmission Electron Microscopy (TEM)

Transmission electron microscopy was carried out on two different TEMS, 200 KV FEI Tecnai G² F20 S-Twin (S) TEM and FEI TitanTM 80-300. Tecnai has 200 KV and energy spread of 0.7 eV and resolution of 0.24 nm. It has a Super-Twin objective lens with 1.2 mm chromatic (Cc) and aberration (Cs) coefficient, which allows for 80° tilt and point to point resolution of 0.16 nm. For scanning transmission electron microscopy (STEM) imaging, high angle annular dark

field (HAADF) detector is attached. TEM samples were prepared via either conventional route or FIB technique. The conventional TEM samples have 3 mm thin disc. The 3 mm disc is punched out of mechanically polished sample. The thickness of punched disc was further thinned down using Gatan Dimple GriderTM. The thinned disc is subsequently subjected to ion milling in Gatan precision ion polisher (PIPS) using 4.5 KV ion guns tilted at angle of 2.5° followed by final milling.

2.7. 3D Atom Probe (3DAP)

An Imago scientific local electrode atom probe (LEAP 3000 X HR) 3D atom probe (3DAP) was used for the present work. It has added facility of laser-pulsed evaporation technique. Figure 2.5 shows the schematic diagram of a three dimensional atom probe. The sample for the APT experiments was prepared in the FIB system. A needle shaped specimen with tip radius 20-100 nm was prepared and then laser or pulse voltage was applied to initiate field evaporation from the tip surface. The time of flight and position data were used to re-create the distribution of atoms on the needle.

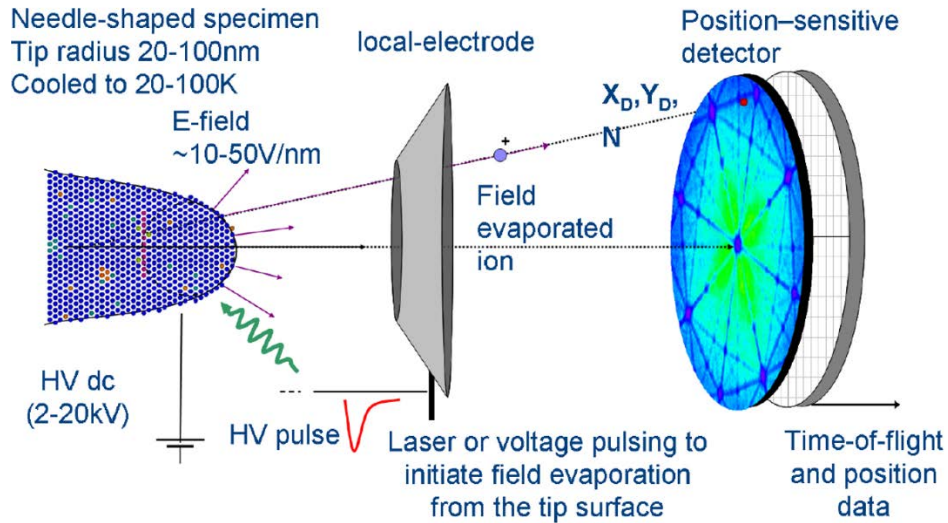


Figure 2.5: Schematic diagram of a three-dimensional atom probe.

2.8. Nano-Indentation

The depth sensing nano-indentation technique has been extensively used in recent years to

determine the hardness of material in bulk and thin film form. It has been also used to determine the hardness of individual phase in a multiphase material as the indentation size is very small and can be fit within the phase boundary. Ability to measure on deeply scaled dimensions permits identification of individual phase-wise properties. This technique has been used to measure the hardness and modulus of a metallic glass composite. Figure 2.6 (a) shows a series of indentations performed on the sample. Figure 2.6 (b) shows an isolated indentation on amorphous matrix, Figure 2.6 (c) on the crystalline dendrite and Figure 2.6 (d) on the interphase boundary of the two phases. The corresponding modulus and hardness obtained from the series of indentations shown in Figure 2.6 (a) is shown in Figure 2.6 (e) and Figure 2.6 (f) respectively. This capability permits the usage of this technique for multiple phases [1].

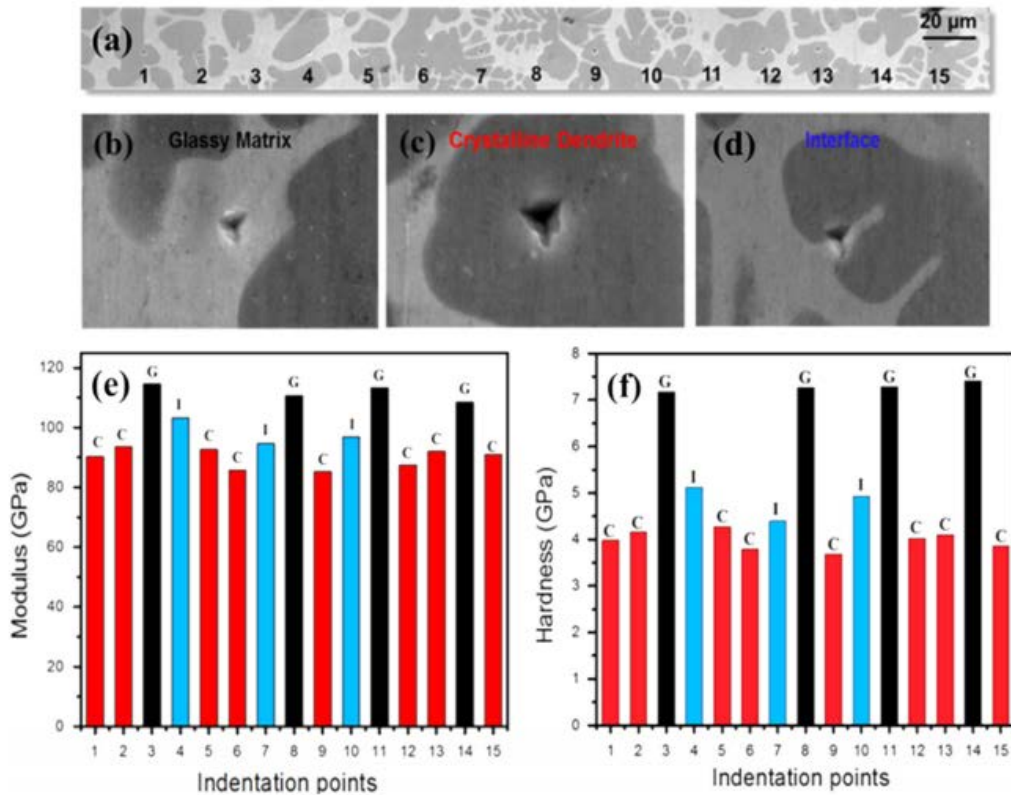


Figure 2.6: (a) shows a series of indentations performed on the sample, (b) shows an isolated indentation on amorphous matrix, (c) on the crystalline dendrite and, (d) on the interphase boundary of the two phases. The corresponding modulus and hardness obtained from the series of indentations shown in (a) is shown in (e) and (f) respectively [1].

Nano-indentation is like conventional indentation techniques like Brinell, Knoop, Vickers and Rockwell, where indentation was made on concerned material with indenter made of very strong material and known geometry. The hardness is defined as mean contact pressure and determined by dividing the maximum applied load by the projected area of the indentation. The penetration depth of the indenter is much higher in the conventional hardness measurement technique in the range of micrometer whereas the penetration depth is much smaller in nano-indentation technique in the range of nanometer. So, the residual impression made by the nano-indenter is in the nanometer and almost impossible to determine the projected area by visual inspection using an optical microscope which is usual technique in the conventional hardness measurement technique. In this technique, the depth of penetration of the indenter is measured and then using the relation between contact depth and contact area the projected area is evaluated and following the hardness is determined. In general, this technique is called depth sensing indentation or instrumented indentation.

2.8.1. Load-Displacement Curve

The nano-indentation technique involves applying load with a steady increasing load from zero to given maximum load. The instrument records the depth of penetration with applied load up to the maximum applied load (loading curve). Further, the load is steadily removed while recording the penetration depth (unloading curve). Figure 2.7 shows a typical load-displacement curve obtained from nano-indentation technique performed on fused quartz sample. When the load is removed from the sample the material tends to regain its original shape but gets prevented due to the plastic deformation in the material. The material shows some amount of recovery due to the presence of elastic strain. In Figure 2.7 the h_e indicates the elastic recovery and h_p is the permanent deformation occurred during the indentation and h_t is the total displacement. Elastic modulus of

the material can be determined via analyzing the unloading part. The modulus determined from this technique also contains a component of the tip material. Therefore, it is termed as reduce modulus.

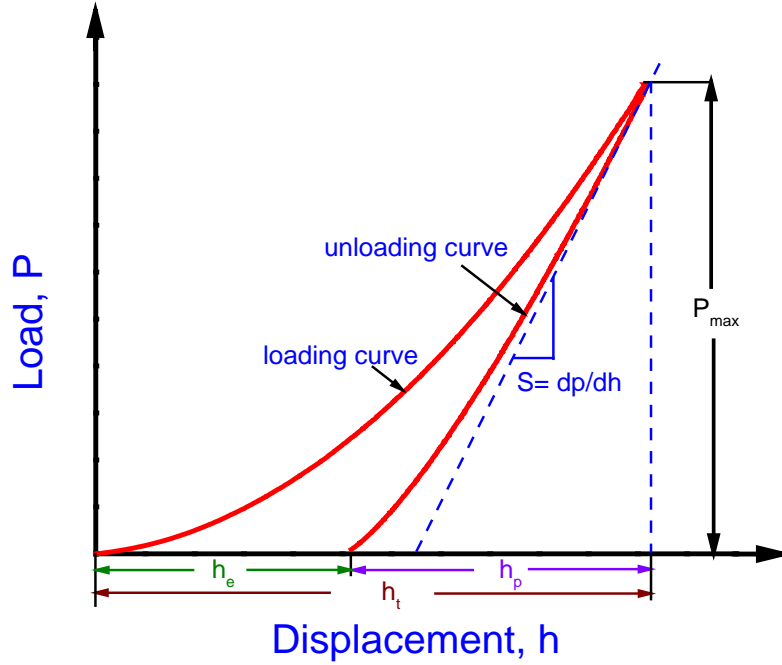


Figure 2.7: Schematic of load displacement curve.

2.8.2. Hardness and Modulus Measurement

Hardness (H) of the material can be determined using the following relation:

$$H = \frac{P_{max}}{A} \quad (1)$$

where P_{max} = maximum applied load and A = contact area.

As discussed earlier it is not possible to determine the contact area using the convention technique and it is measure of the depth of penetration during the indentation. The nano-indentation use known geometry of indenter tip. Using the geometrical relation of the measured depth and known geometry the contact area is calculated. Below the geometry of berkovich tip (Figure 2.8) and its relation with the indentation depth has been discussed.

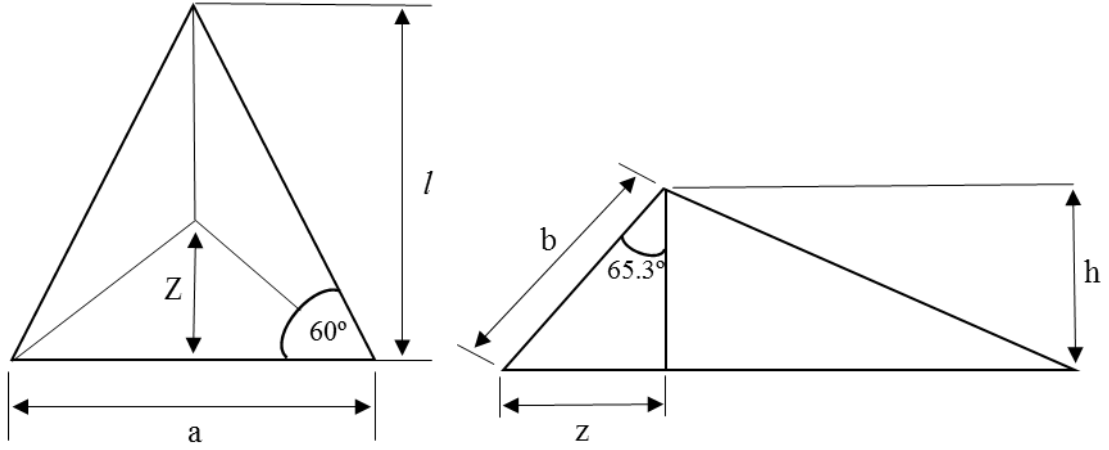


Figure 2.8: Projected area of Berkovich tip.

Projected area

$$\tan 60^\circ = \frac{l}{a/2}; l = \frac{\sqrt{3}}{2} a \quad (2)$$

$$A_{proj} = \frac{al}{2} = \frac{\sqrt{3}}{2} a^2 \approx 0.433a^2 \quad (3)$$

$$\cos 65.27^\circ = \frac{h}{b}; h = \frac{a \cos 65.27^\circ}{2\sqrt{3} \sin 65.27^\circ} = \frac{a}{2\sqrt{3} \tan 65.27^\circ} \quad (4)$$

$$a = 2\sqrt{3} h \tan 65.27^\circ \quad (5)$$

$$A_{proj} = 3\sqrt{3}h^2 \tan^2 65.27^\circ = 24.29h^2 \quad (6)$$

Surface area

$$A_{surf} = 3 \frac{ab}{2} \quad (7)$$

$$\sin 65.27^\circ = \frac{z}{b}; z = \frac{a}{2} \tan 30^\circ = \frac{a}{2\sqrt{3}} \quad (8)$$

$$b = \frac{a}{2\sqrt{3} \sin 65.27^\circ} \quad (9)$$

$$A_{surf} = 3 \frac{a^2}{4\sqrt{3} \sin 65.27^\circ} \approx 0.477a^2; a = 2\sqrt{3} \tan 65.27^\circ \quad (10)$$

$$A_{surf} = 26.98h^2 \quad (11)$$

For original berkovich indenter,

$$\text{Contact angle} = 65.033^\circ$$

$$A_{proj} = 24.29h^2 \quad (12)$$

$$A_{surf} = 26.40h^2 \quad (13)$$

The reduce modulus (E_r) is expressed as a function of contact area and slope of the unloading curve using the following relation:

$$S = \frac{dp}{dh} = \frac{2}{\sqrt{\pi}} E_r \sqrt{A} \quad (14)$$

where A is the contact area and dp/dh is slope of the unloading curve. And E_r has the following relation with the tip elastic constant and the sample elastic constant:

$$\frac{1}{E_r} = \frac{1 - \nu^2}{E} + \frac{1 - \nu_i^2}{E_i} \quad (15)$$

2.8.3. Nano-Indentation Setup

Hysitron nano-indenter with built-in XSol600 heating stage was used for room temperature and elevated temperature tests. The instrument has high resolution in load and displacement which enables the capability do the indent even with few micro newton loads. The indentation can be performed in both load and displacement control mode. Figure 2.9 shows image of the inside set up of the instrument. It has x, y and z axis motor. The stage is placed at the x-y axis motor which moves the sample in the x and y plane. And the tip can be moved in z axis. Tip is usually mounted on a transducer and then the transducer mounted on the pizo-scanner. The pizo-scanner and the optics is attached together on the z axis motor. The tip and the optic both move together in the z

axis. The optic is used to identify the sample and do the indentation on required area in the sample. Special care needs to be taken during the test to avoid damaging the tip. The pizo-scanner can also move in x-y plane without moving the stage up to small distance within 100 μm .

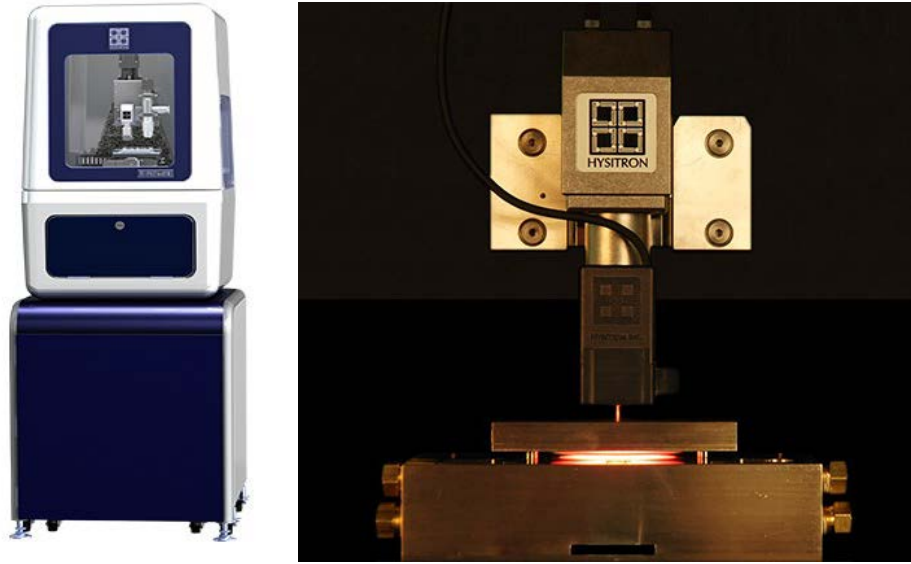


Figure 2.9: Set up of Hysitron nano-indenter and high temperature stage.

The platform or stage and the tip is different for high and room temperature indentation. The basic operation technique and the analysis is same for room and elevated temperature test as the tip geometry is same in both case. In this study diamond bekovich tip is used for all the tests.

2.8.4. Room Temperature Test Set Up

The room temperature diamond tip is attached on a small polymer holder. The length of the holder is 3-4 mm and diameter less than 1 mm. The geometry of bercovich tip is discussed in the earlier section. The stage used for room temperature test is a stainless steel incorporated with equally spaced magnet inside it. The magnets are not visible from outside. The platform is mounted on the x-y motor during the indentation. Six samples can be mounted together in the stage. A fine polished sample is first attached to magnetic steel stub using super glue. The steel stub is then placed near the magnetic place of the stage. The bond between the platform and the sample need to be very strong to perform the indent and measurement of hardness and modulus. Special care

needs to be taken during time of attaching the sample on the steel stub as trapped air between the sample and stub can lead to inaccurate result or hindered the indentation.

2.8.5. High Temperature Set Up

The tip used for high temperature test is a diamond berkovich tip attached to a long glass holder instead of a small polymer holder to withstand the elevated temperature. The length of the tip is around 20 mm and diameter less than 1 mm. The purpose of using long shaft to avoid the transducer coming very close to high temperature and the tip can go through the small hole of the stage.

The elevated temperature test was performed using a special platform which can heat the sample while doing the indentation. Maximum temperature of 600C can be achieved. Figure 2.10 shows schematic of the high temperature indentation setup. The platform consists of two-part top and bottom stage. Both parts are incorporated with heating element, thermocouple, and gas purging channel. The bottom heating element work as heater as well as the platform for indentation. The sample was placed on the bottom heating element. Further, the top plate was placed and mechanically clamped with the bottom plate to secure the proper placement of sample. Continuous flow of Ar gas was maintained during elevated temperature test to protect the sample from oxidation. The top stage is incorporated with 2.5 mm diameter hole at the center to bring tip in contact with the sample.

During indentation at elevated temperature Ar gas cause arcing in the transducer sometime, which hindered normal indentation on the sample. To avoid the arcing a positive pressure was created around the transducer by purging air. The transducer is covered with air tight shield. Constant flow of air is maintained in the air shield which creates positive pressure around the transducer.

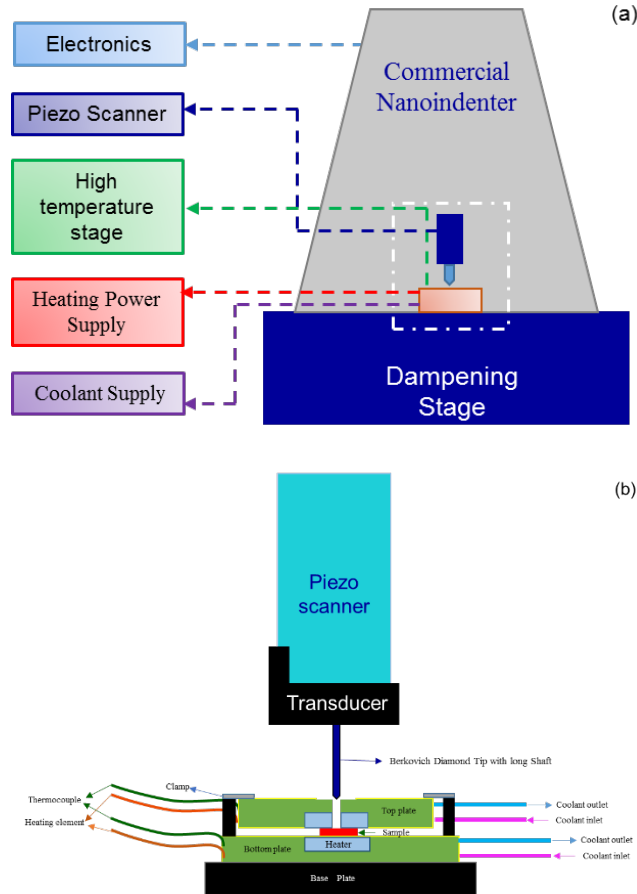


Figure 2.10: (a) Nanoindenter with high temperature stage, (b) expended view of the dashed white box.

2.8.6. Calibration

2.8.6.1. System Calibration

System calibration is performed to calibrate the transducer constant and check the noise level of the instrument. The noise level must be below a certain level to perform the instrument properly. Calibration was done by performing indent on air using a maximum load of $700 \mu\text{N}$. The system calibration needs to be performed before starting the indentation.

2.8.6.2. Tip to Optic Calibration

Tip to optic calibration is performed to calibrate the distance between the tip and the optic. Each time the tip removed from the transducer and reinstalled, there is a probability of variation

in the distance between tip and optic. Therefore, tip to optic calibration needs to perform each time the tip is installed in the transducer. It is performed by following the standard procedure.

2.8.6.3. Tip Area Function Calibration

In previous section, the relation between the depth and contact area mentioned is for an ideal berkovich tip. Although, practically it is almost impossible to make a tip with perfect geometry. Tip always have some amount of rounding at the end. The radius of curvature in a new tip lies in range of 100 - 150 nm. The rounded part of the tip effects the hardness and modulus measurement. By performing tip area function calibration relation between the depth and the contact area is developed incorporating the rounded part of the tip.

Tip area function is calibrated by performing indentation on a standard fused quartz (FQ) sample with known reduced modulus. The reduced modulus of the FQ sample is 69.6 GPa, when the indentation was performed using a diamond berkovice tip. A series of indents were performed on the FQ sample on a range of load e.g. 250-10000 μ N. Using the depth of these indents area function is created. This area function was used for determining the hardness and modulus of the sample. To create the area function the h_c is determined for each indent using the following relation:

$$h_c = h_{max} - \varepsilon \frac{P_{max}}{S} \quad (16)$$

where h_{max} is the total depth of the indent, P_{max} is the maximum applied load, ε is a geometrical constant to account the edge effects and taken as 0.75 and S is the stiffness of the unloading curve is defined by $S = dp/dh$.

The reduced modulus is defined as

$$E_r = \frac{S\sqrt{\pi}}{2\sqrt{A}} \quad (17)$$

where A is the contact area and can be express by the following relation using above equation:

$$A = \frac{\pi}{4} \left(\frac{S}{E_r} \right)^2 \quad (18)$$

For a material with known reduced modulus the A is determined using the above equation.

Hardness is determined using this contact area. The A and h_c is calculated using equation 1 and 3 for each indent performed in the FQ sample. A plot of A vs h_c is created fit the curve up to sixth order polynomial form

$$A = C_0 h_c^2 + C_1 h_c + C_2 h_c^{1/2} + C_3 h_c^{1/4} + C_4 h_c^{1/8} + C_5 h_c^{1/16} \quad (19)$$

The C_0 is kept as 24.5 as it is the ideal berkovich constant.

And the hardness is determined as

$$H = \frac{P_{max}}{A} \quad (20)$$

To determine the hardness and modulus of a sample indentation data analyzed using this tip area function. For an indent, the h_c is determined followed by evaluation of contact area of the indent. Then the hardness and modulus is determine using the determined contact area.

2.9. Pico-Indentation

Instrumented nano-indentation provided a useful platform to evaluate and understand the mechanical behavior of material, which conventional technique for bulk materials cannot achieve. Still this technique is not able to cover the wide range of material size. In recent years compression and tension test inside TEM and SEM has been presented by researchers. Using these in-situ studies, it became possible to evaluate the mechanical property of small scale sample which nano-indentation cannot perform. In addition, these techniques provide the capability to visually observe the deformation process in real time. In situ TEM based technique provide a lot of inside information but the specimen size is very small and the preparation technique is complex and

tedious. In addition, due to small scale it might not be comparable to the bulk sample. On the other hand, in-situ SEM technique is less complicated than in-situ TEM and capable of providing useful information. In addition, it provides a large field of view, sample preparation is much easier and capable to perform test on different dimension from millimeter to micro/nanometer.

In the present work, PI SEM pico-indenter (Hysitron) has been used. Figure 2.11 shows the schematic of picoindenter set up. The stage is equipped with heating stage and can achieve up to 800°C. For high temperature test closed loop, PID controlled sample and tip heating is used for isothermal contact during testing. Sample is heated by consumable resistive heater and tip is heated by special probe design which minimizes conduction through the probe shaft for maximum stability.

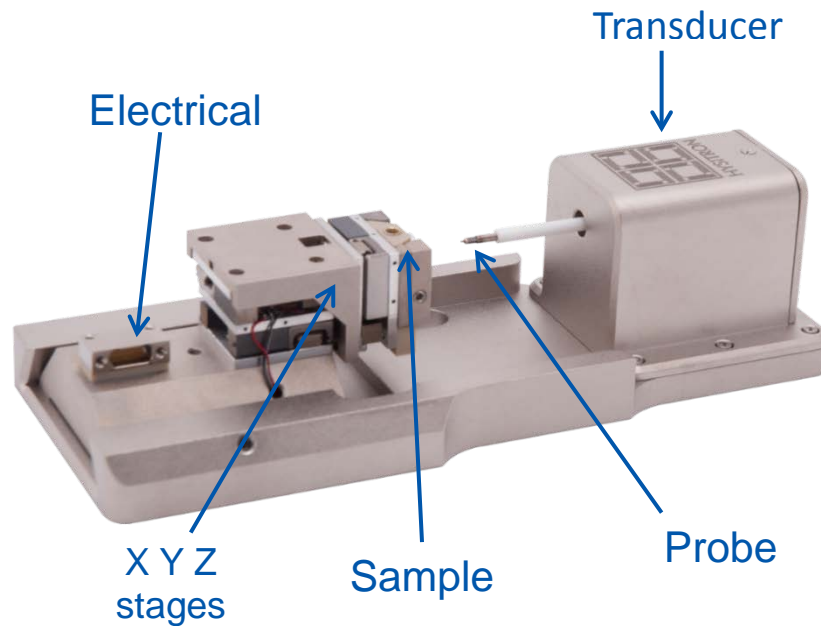


Figure 2.11: Schematic of picoindenter set up.

Figure 2.12 shows a zoomed-in view of the stage and tip for high-temperature testing. A liquid-cooled heat sink is used to remove excess heat from the microscope to maintain imaging quality. The vacuum environment inside minimizes the oxidation of the sample. The pillar-shaped sample is compressed using a flat punch diamond tip with a 2 μm length. The flat punch was fabricated

by milling out the sharp part of a Berkovich shape diamond tip using FIB. The experimental section has following steps: (i) place the concerned pillar under the microscope, (ii) calibration of indenter to microscope distance, (iii) positioning of the calibrated flat indenter tip just above the sample, and (iv) performing the compression test on the pillar at constant strain rate. Parameters such as force applied on the pillar, contact stiffness and compressive displacement are recorded. With the help of recorded data, the stiffness and modulus can be calculated. Further, the load-displacement data can be used for the stress-strain plot of the alloys.

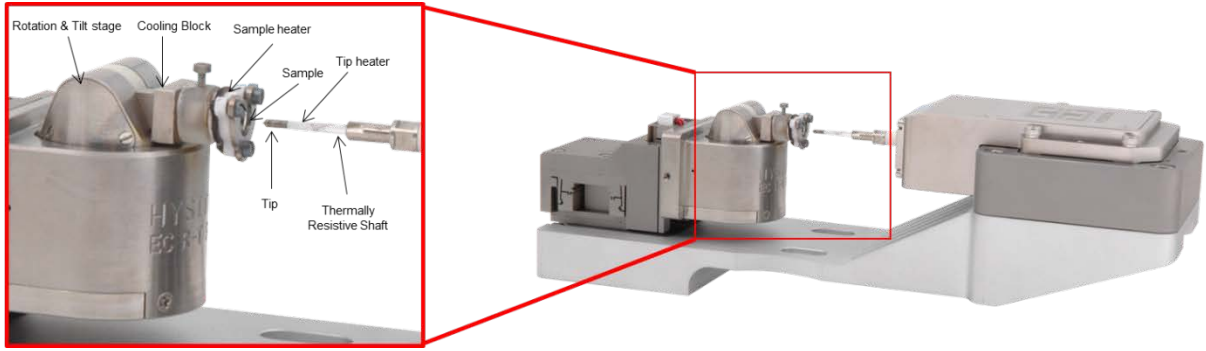


Figure 2.12: Zoomed in view of the stage and tip for high temperature test.

2.10. Data Analysis

For stress and strain calculation, a cylindrical pillar of height L_0 and cross-sectional area A_0 is assumed. After uniaxial compression, the dimension of cylinder changed to length L_p and cross-section area A_p and follow the relation $A_p L_p = A_0 L_0$. The total strain can be expressed as

$$\varepsilon_{tot}^{compressive} = \varepsilon_{el} + \varepsilon_{pl} = \frac{1}{E} \frac{P L_p}{A_0 L_0} - \ln \left(\frac{L_p}{L_0} \right) \quad (21)$$

where ε_{el} is the elastic compressive strain, ε_{pl} is the plastic compressive strain, P is the instantaneous load on the pillar, and E is the gold elastic modulus in $\langle 001 \rangle$ direction. The L_p is equal to difference between L_0 and compressive plastic displacement up. The compressive plastic displacement $u_p = u - u_{el}$, where u is the total displacement at any point on the loading curve,

u_{el} is the elastic displacement which can be derived based on Hooke's law and assuming conservation of volume during plastic flow

$$u_{el} = \frac{1}{E} \frac{P}{A_0 L_0} L_p^2 \quad (22)$$

The compressive plastic displacement can be written as

$$u_p = u - \frac{1}{E} \frac{P}{A_0 L_0} L_p^2 \quad (23)$$

After substituting u_p in the expression of $L_p = L_0 - u_p$

$$L_p = \frac{EA_0 L_0}{2P} \left(1 - \sqrt{1 - 4 \left(\frac{P}{EA_0 L_0} \right) (L_0 - u)} \right) \quad (24)$$

After calculating the compressive plastic strain, total compressive stress can be determined using Eq. (21).

The stress is evaluated by dividing the load (measured) by the plastic area

$$\sigma = \frac{P}{A_p} = \frac{PA_0 L_0}{L_p} \quad (25)$$

Figure 2.13 shows the typical load-displacement curve and corresponding stress-strain curve [7].

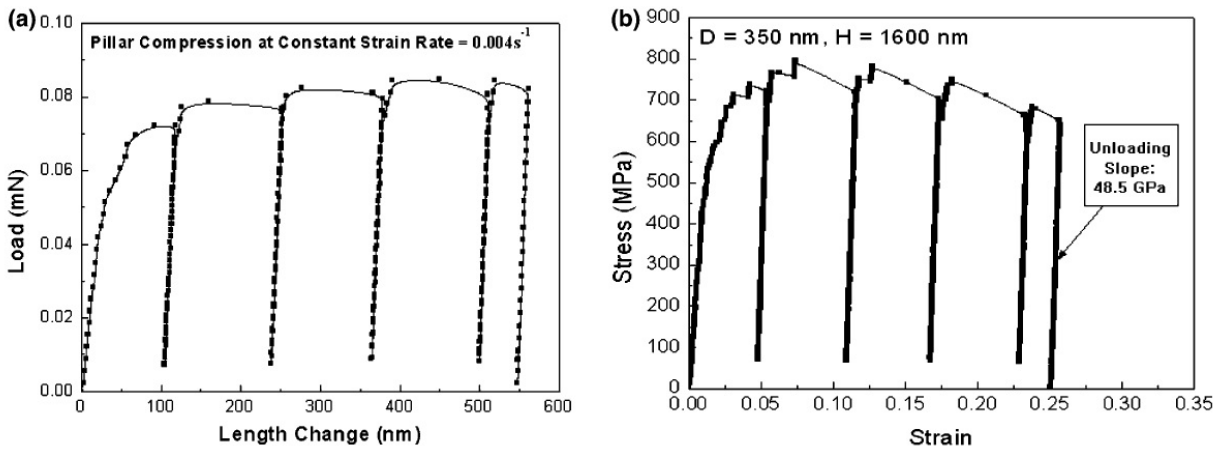


Figure 2.13: (a) Pillar compression of Au single crystal and (b) stress-strain generated plot [7].

2.11. References

- [1] A. Ayyagari, T.W. Scharf, S. Mukherjee, Dry reciprocating sliding wear behavior and mechanisms of bulk metallic glass composites, *Wear*. 350 (2016) 56-62.
- [2] S. Das, R. Santos-Ortiz, H.S. Arora, S. Mridha, N.D. Shepherd, S. Mukherjee, Electromechanical behavior of pulsed laser deposited platinum-based metallic glass thin films, *physica status solidi (a)*. (2015).
- [3] C. Schuh, J. Mason, A. Lund, Quantitative insight into dislocation nucleation from high-temperature nanoindentation experiments, *Nature Materials*. 4 (2005) 617-621.
- [4] T. Zhu, J. Li, K.J. Van Vliet, S. Ogata, S. Yip, S. Suresh, Predictive modeling of nanoindentation-induced homogeneous dislocation nucleation in copper, *J. Mech. Phys. Solids*. 52 (2004) 691-724.
- [5] D. Lorenz, A. Zeckzer, U. Hilpert, P. Grau, H. Johansen, H. Leipner, Pop-in effect as homogeneous nucleation of dislocations during nanoindentation, *Physical Review B*. 67 (2003) 172101.
- [6] K.J. Van Vliet, J. Li, T. Zhu, S. Yip, S. Suresh, Quantifying the early stages of plasticity through nanoscale experiments and simulations, *Physical Review B*. 67 (2003) 104105.
- [7] J.R. Greer, W.C. Oliver, W.D. Nix, Size dependence of mechanical properties of gold at the micron scale in the absence of strain gradients, *Acta Materialia*. 53 (2005) 1821-1830.

CHAPTER 3

EVOLUTION OF ATOMIC DISTRIBUTION DURING DEVITRIFICATION OF BULK METALLIC GLASS INVESTIGATED BY ATOM PROBE MICROSCOPY AND NANO-INDENTATION¹

3.1. Abstract

Evolution of atomic distribution during devitrification of a zirconium-based bulk metallic glass, $\text{Zr}_{41.2}\text{Ti}_{13.8}\text{Cu}_{12.5}\text{Ni}_{10.0}\text{Be}_{22.5}$, was investigated using three-dimensional atom probe microscopy. Atom probe analysis showed uniform distribution of constituent elements for the as-cast alloy, with no phase separation. The metallic glass was annealed at different temperatures to study the crystallization pathways and the length scale, distribution, and morphology of the phases formed. Devitrification was found to proceed via the formation of a metastable icosahedral phase. The devitrification pathway is explained based on “strong-liquid” behavior of this alloy. The glassy alloy with icosahedral phase shows increase in hardness and modulus, which can be attributed to the embedded icosahedral phase. The devitrified alloys exhibited significant improvement in hardness and might be resultant of nanocrystalline microstructure with multiple intermetallic compounds.

Keywords: Atomic distribution; Metallic glass; Atom probe microscopy

3.2. Introduction

The bulk metallic glass, $\text{Zr}_{41.2}\text{Ti}_{13.8}\text{Cu}_{12.5}\text{Ni}_{10.0}\text{Be}_{22.5}$, commonly referred to as Vitreloy1 is a canonical example of a good glass former [1,2]. Extensive research has been done on this alloy system to understand its excellent glass forming ability in particular and devitrification behavior of metallic glasses in general [2-8] Most of the previous studies have concluded that crystallization

¹This chapter has been largely adapted from the following journal publication with permission from publisher: “Evolution of atomic distribution during devitrification of bulk metallic glass investigated by atom probe microscopy”, Materials Letters 158 (2015): 99-103

in Vitreloy1 is preceded by liquid-liquid phase separation [2-8]. In contrast, Martin *et al* [9] demonstrated in a later study that there is no phase separation in this system and crystallization proceeds via the formation of a metastable icosahedral phase (*i-phase*). However, a detailed report and discussion of the morphology, size, and distribution of the icosahedral phase as well as the subsequent crystallized phases is lacking. Another aspect of devitrification that has been completely overlooked is the interface between the different thermodynamically stable phases. A sharp interface (few atomic layers wide) typically indicates eutectic crystallization, where interface diffusion plays a more dominant role rather than volume diffusion [10]. Three-dimensional atom probe (3DAP) microscopy represents a unique platform to probe the evolution of atomic distribution and the interfaces with sub-nanometer resolution. In addition a detailed study on nanomechanical behavior of semi glassy and devitrified microstructure has not been performed.

Here, we report on the devitrification behavior of Vitreloy1 ($\text{Zr}_{41.2}\text{Ti}_{13.8}\text{Cu}_{12.5}\text{Ni}_{10.0}\text{Be}_{22.5}$) investigated using 3DAP microscopy at different annealing temperatures. Detailed elemental mapping and phase evolution was investigated in the starting amorphous condition, early stages of devitrification as well as the fully crystallized sample. The length-scale and distribution of the metastable phases together with the interface between the thermodynamically stable phases are thoroughly analyzed to explain the devitrification mechanism. The nanomechanical behavior of the samples is studied to correlate the hardness with microstructure.

3.3. Experimental

The glass transition temperature (T_g) and crystallization temperature (T_x) were determined using differential scanning calorimetry (DSC, Netzsch) with a heating rate of 20 K/min. X-ray diffraction (XRD) analysis was done using Rigaku III Ultima X-ray diffractometer with Cu- K_α radiation of wavelength 1.54 nm. Four samples were analyzed using 3DAP: (i) as cast, (ii) annealed

at 663 K for 5 min, (iii) annealed at 673 K for 10 min, and (iv) fully crystallized (heated up to 873 K at 20 K/min). For 3DAP studies, laser-pulsed local electrode atom probe operating at a wavelength of 532 nm and 12 ps pulse duration was used. The laser pulse was used at 0.6 Joules and 35 K with 0.5% evaporation rate. Specimens for 3DAP were prepared using focused ion beam (FIB) lift-out technique. 3DAP analysis was carried out to obtain concentration profiles and elemental distribution at different locations/interfaces of the annealed and crystallized specimens. The high temperature nanoindentation was performed using the Hysitron TI premier with the build in high temperature test set up. The test was performed with 8000 μ N load at different temperature. A diamond berkovich tip attached to 20 mm shaft was used for indentation.

3.4. Results and Discussion

DSC of as-cast metallic glass is shown in Figure 3.1(a). The glass transition temperature was found to be 633 K and crystallization temperature found to be 723 K. The first crystallization peak (T_{p1}) indicates the formation of a metastable icosahedral phase (*i-phase*) [9]. The second crystallization peak (T_{p2}) indicates transformation of the amorphous phase to stable crystallization phases. XRD data for all the samples is shown in Figure 3.1(b). The as-cast sample shows a broad peak indicating its fully amorphous structure. The sample annealed at 673 K shows small peaks at 2θ values of nearly 35° and 38° corresponding to the previously reported *i-phase* [11]. XRD analysis of the fully crystallized sample shows six different crystalline phases and a few peaks that could not be identified (Figure 3.1(b)).

Figure 3.1(c) and (d) show the 3DAP reconstruction of the as-cast sample and the corresponding elemental distribution respectively. Uniform spatial distribution for all the elements in the as-cast sample is observed. The elemental composition determined using 3DAP is close to the nominal composition (Table 3.1). Composition analysis of the sample annealed at 663 K

obtained by 3DAP is also give in Table 3.1. Similar to the as-cast sample, 3DAP analysis of the sample annealed at 663 K shows uniform distribution of elements without any evidence of devitrification or phase separation (not shown because it is very similar to Figure 3.1(c)).

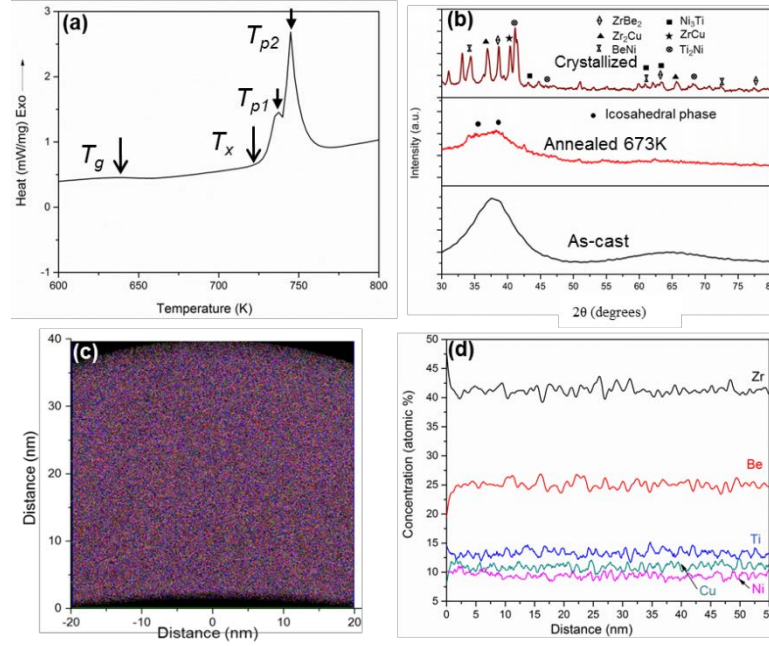


Figure 3.1: (a) DSC curve obtained by heating as-cast Vitreloy1 at a rate of 20 K/min; (b) XRD for as-cast metallic glass, metallic glass annealed at 673 K for 10 min, and fully crystallized metallic glass; (c) Atom probe 3D reconstruction and (d) concentration profile for as-cast metallic glass. The glass transition and crystallization temperatures are indicated by T_g and T_x respectively. T_{p1} and T_{p2} are the first and second crystallization peaks respectively. XRD shows fully amorphous structure for the as-cast sample and sample annealed at 663 K for 5 minutes. The sample annealed at 673 K for 10 min shows the formation of metastable *i*-phase, while the fully crystallized sample shows six different binary phases [12].

3DAP results for the sample annealed at 673 K are shown in Figure 3.2. 3D reconstruction Figure 3.2 (a) and (b) clearly show the formation of secondary phases in the amorphous matrix. In Figure 3.2(b), the amorphous matrix has been suppressed to clearly show the morphology and size distribution of *i*-phase. The composition profile across one isolated precipitate (Figure 3.2(c)) shows that it is rich in Ti and depleted in Be (Figure 3.2(d)). The matrix in turn gets enriched in Be and depleted in Ti. This indicates that *i*-phase forms a transient equilibrium with Be rich glassy matrix. Fig. 2(e) shows HRTEM image of sample annealed at 673 K for 10 min. Short range

icosahedra-like atomic clusters are seen, marked by white dashed line as guide to the eye. The clusters range in size from 2 nm to 10 nm, very similar to the 3DAP results (Fig. 2(a) and (b)).

Table 3.1: Elemental composition in the as-cast Vitreloy1, $Zr_{41.2}Ti_{13.8}Cu_{12.5}Ni_{10.0}Be_{22.5}$ (As-cast), metallic glass annealed at 663K for 5 min, metallic glass annealed at 673K for 10 min and fully crystallized metallic glass, as determined by 3D atom probe microscopy. Phases “A”, “B”, “C”, and “D” in the fully crystallized sample are shown in Figure 3.3. [12]

Samples	Phases	Composition (atomic %)				
		Zr	Ti	Ni	Cu	Be
As Cast	Amorphous	41.0±1.70	13.5±1.16	10.0±0.96	10.9±1.08	24.6±1.49
663K, 5 min annealed	Amorphous	41.5±1.69	13.4±1.17	9.4±1.02	11.0±1.08	24.8±1.50
673K, 10 min annealed	Matrix	41.8±0.96	13.3±0.87	8.6±0.53	11.3±0.53	24.8±0.45
	Isolated particle	39.9±0.82	26.7±0.73	11.2±0.49	10.8±0.54	11.3±0.47
Fully Crystallized	A	35.4±0.42	29.7±0.33	12.7±0.27	14.8±0.28	7.3±0.32
	B	43.3±0.31	8.5±0.24	8.9±0.19	8.7±0.20	30.6±0.24
	C	57.9±0.35	9.3±0.26	3.8±0.25	27.7±0.23	1.3
	D	35.4±0.24	1.0	0.0	0.0	63.6±0.29

To analyze growth of the icosahedral phase (*i-phase*) nuclei, composition of particles in different size range was determined on the sample annealed at 673 K for 10 min. Table 3.2 shows the volume range of particles and the corresponding composition. Large fraction of the particles (79 %) is in the size range of 0-100 nm³. The composition of the particles is almost identical with minor variation across all the different sizes, which indicates that *i-phase* nucleates with a significantly different composition within the starting liquid and continues to grow with the same composition.

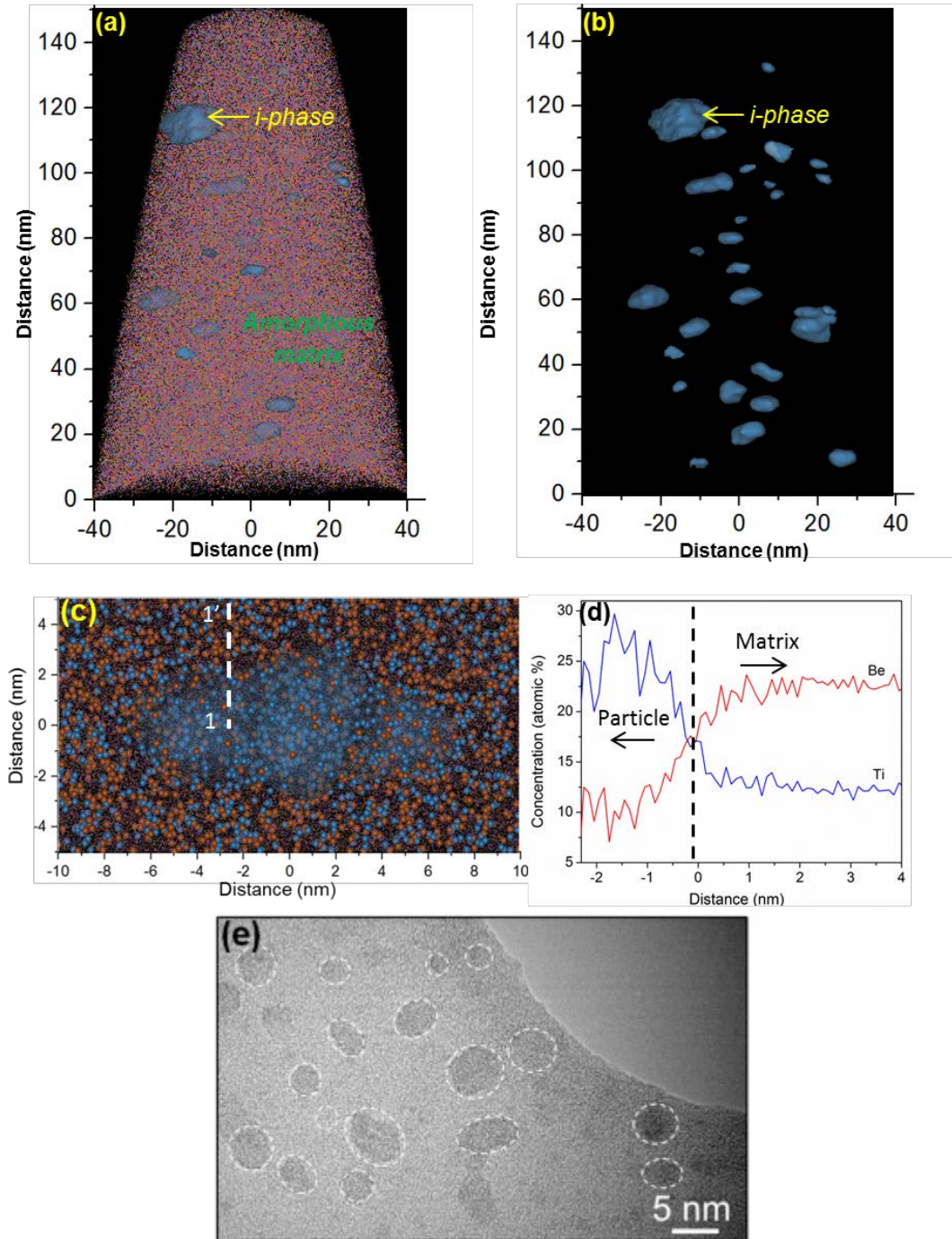


Figure 3.2: Atom probe 3D reconstruction for sample annealed at 673 K for 10 min showing (a) *i*-phase particle and amorphous matrix and (b) *i*-phase particle with the matrix suppressed; (c) An isolated *i*-phase particle and (d) concentration profile along the line 1-1' shown in (c), HRTEM image showing icosahedra-like short range clusters in an amorphous matrix. White dashed lines around the clusters are added as a guide to the eye. [12].

Table 3.2: Volume fraction and chemical composition of icosahedral phase as a function of size for Vitreloy1 ($Zr_{41.2}Ti_{13.8}Cu_{12.5}Ni_{10.0}Be_{22.5}$), annealed at 673 K for 10 minutes. [12]

Volume nm ³	No. of particles	% of particles	Composition (atomic %)				
			Zr	Ti	Ni	Cu	Be
0-100	37	78.7	39.6±1.7	26.3±1.6	10.9±1.1	11.1±1.1	11.6±1.1
100-200	5	10.6	38.2±2.1	26.5±1.9	11.4±1.4	11.1±1.1	11.8±1.4
200-300	3	6.3	39.6±1.5	26.5±1.4	11.7±1.0	10.8±0.9	10.8±0.9
300-400	1	2.1	39.5±1.9	25.3±1.8	11.3±1.3	11.2±1.3	12.0±1.3
400-500	1	2.1	38.4±2.2	25.8±2.1	12.1±1.5	12.3±1.5	11.3±1.4

The 3DAP results for fully crystallized sample (obtained by heating to 873 K) are shown in Figure 3.3. This reconstruction indicates the formation of four distinct phases marked “A”, “B”, “C” and “D”. The elemental composition for all these phases is given in Table 3.1. The phase “A” is Ti rich and Be depleted with a composition close to the metastable *i-phase*, indicating that the icosahedral phase facilitates nucleation of subsequent crystalline phases without itself transforming during crystallization. Phase “D” corresponds to $ZrBe_2$ and phase “C” corresponds to a mixture of Zr_2Cu and Ti_2Ni . These phases are consistent with the XRD results for fully crystallized sample given in Figure 3.1(b). Phase “B” shows a composition close to the nominal composition of the starting alloy, with increase in Zr and Be and decrease in Ti, Cu, and Ni. It is likely to be a mixture of several complex intermetallics. Figure 3.3(c) shows composition profile across the interface of phases “A” and “B”. The interface width between any two phases was found to be less than 5 nanometers. A scanning electron micrograph of the fully devitrified sample shows nano-crystallites in the size range of 10 nm to 100 nm (Figure 3.3(d)).

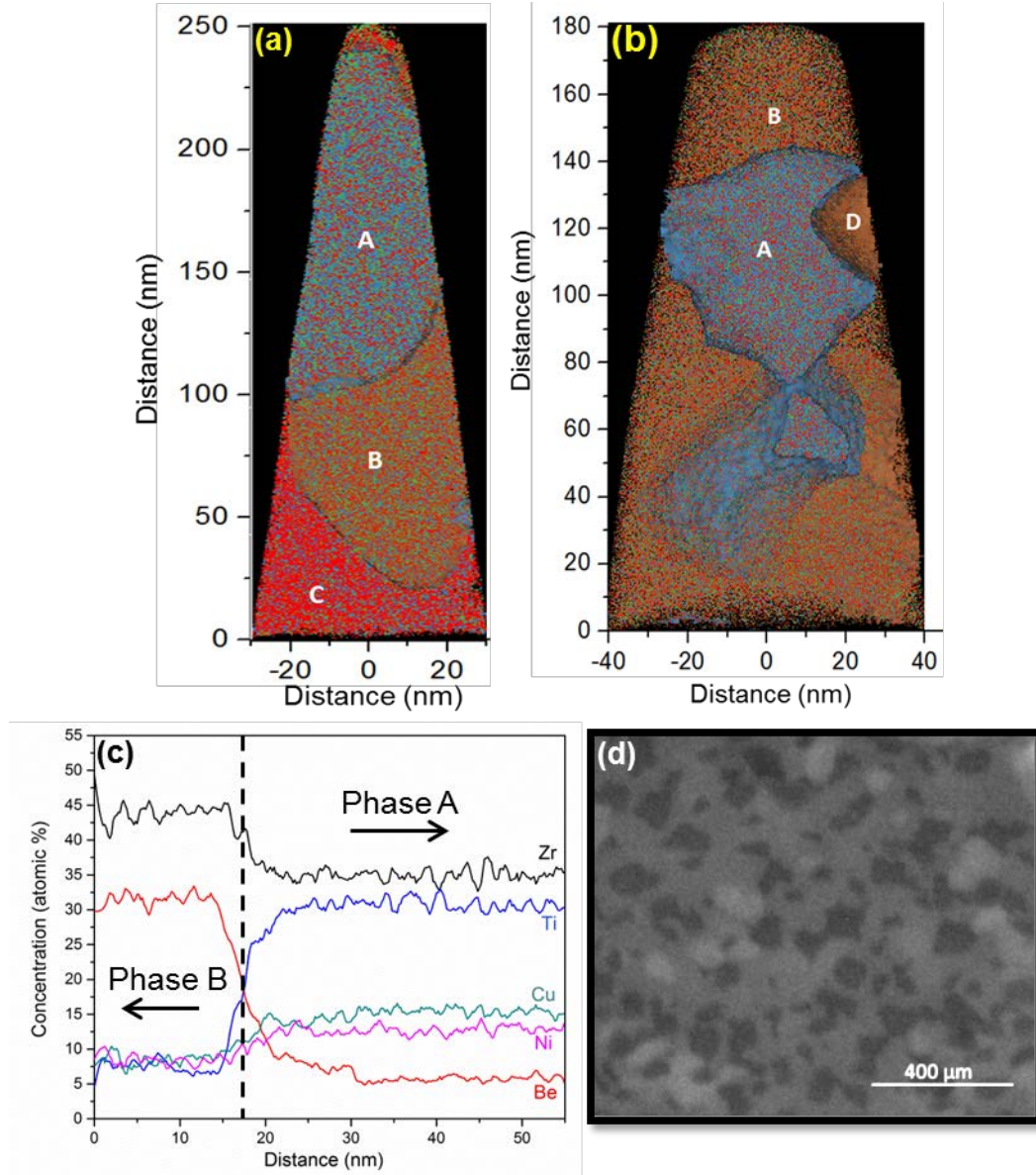


Figure 3.3: (a) and (b) Atom probe 3D reconstruction for fully crystallized metallic glass; (c) concentration profile between phases A and B; (d) SEM image showing the microstructure of the crystallized metallic glass. Atom probe results show the formation of four distinct regions marked by “A”, “B”, “C” and “D”. SEM shows nanocrystalline phases in the size range of 10 nm to 100 nm [12].

In the current study, there was no evidence of liquid-liquid phase-separation for Vitreloy1 prior to crystallization. The microstructure in phase separated metallic glasses shows a typical “core-shell” or “Spinodal” type characteristic [13]. In contrast, the crystallized sample in the current study (Figure 3.3(d)) showed uniform distribution of nano-crystallites. The presence of

short-range-order (SRO) has been reported in many metallic glass compositions with high glass forming ability [13]. Icosahedral clusters are one of the typical short-range-orders formed in metallic glasses [14]. Zirconium based metallic glasses are typically “stronger” liquids and have high value of fragility parameter, due to which the liquid properties do not show drastic changes with temperature [15,16]. “Strong” liquids do not show rapid rearrangement of atomic species, thereby favoring short range icosahedral ordering in the undercooled liquid [15]. The chemistry and size distribution analysis shows that *i-phase* nucleates with a distinctly different composition from the starting amorphous alloy. The icosahedral phase and the undercooled liquid maintain equilibrium for short period. Subsequently, the remaining undercooled liquid transforms to multiple crystalline phases by eutectic crystallization as indicated by the second crystallization peak in DSC. The interface between the different crystallized phases as shown in Figure 3.3 was found to be very sharp (< 5 nm). Sharp interfaces are typically characteristic of eutectic mode of crystallization, where interface diffusion plays a more dominant role [10]. This is consistent with good glass forming ability of this alloy because deep eutectics stabilize the liquid phase.

The mechanical property of glass embedded with quasi-crystalline Particle and the devitrified glass has been studied using nano-indentation technique. *Table 3.3* shows the vicker hardness and hardness and modulus obtained from nano-indentation. It can be observed formation of *i-phase* increase the strength of the material. The sample also shows higher modulus than the as cast glass which indicates the atomic configuration is closely packed than the as cast glass. The devitrified alloy shows significant increase in hardness but slight increase in modulus. Observed result indicates the microstructure and phases formed significantly effect on increase in hardness of the alloy. It has been discussed above the glass form nano grains and different intermetallic

compound. Both plays important role in improving strength of a material. But it is not clear which one is dominant strengthening factor in the alloy.

Table 3.3: Vicker hardness and Nano-indentation hardness and modulus for as-cast glass, glass embedded with quasi-crystal and devitrified glass

Samples	Vicker Hardness (Hv)	Nano Hardness (GPa)	Modulus (GPa)
Glass	497±20	6.95±0.17	115±2.1
Glass + <i>i-phase</i>	515±30	8.00±0.21	126±3.5
Crystallized	607±15	10.48±0.34	135±5.8

Figure 3.4 shows the hardness (Figure 3.4 (a)) and modulus (Figure 3.4 (b)) of three samples with changing temperature. It can be observed the hardness decreases with increasing the temperature for all the samples. In the as cast the glass the hardness drops linearly till 673 K which in $.85T_g$ for the alloy. Above that the temperature drops exponentially with increasing the temperature. The similar behavior reported in earlier work also. At T_g endothermic transformation occur in the glass. The glass transforms into highly viscous solid which possess very strength. Using this property, the glass can be given any complicated shape. This results indicates the strength decreases gradually before T_g (for this alloy $.85T_g$) with a high decreasing rate. At T_g this glass showed a hardness of 1.5 GPa. Above that glass transforms to highly viscous solid and almost makes it impossible to evaluate the hardness using nano-indentation technique. The change in the rate of decrease in strength may be due to change in deformation mechanism. The annealed glass also showed similar behavior with increase in temperature. It also shows sharp decrease in hardness with increasing temperature. Which indicates the formation of *i-phase* does not change the glassy property. Devitrified alloy show less dependence on temperature which is quite unusual for nano-crystalline material. It has been reported that nano-crystalline alloys show higher rate

sensitivity which indicates a deformation mechanism related with atomic diffusion and highly effected by temperature. Modulus of the sample shows similar trend as it showed in the hardness.

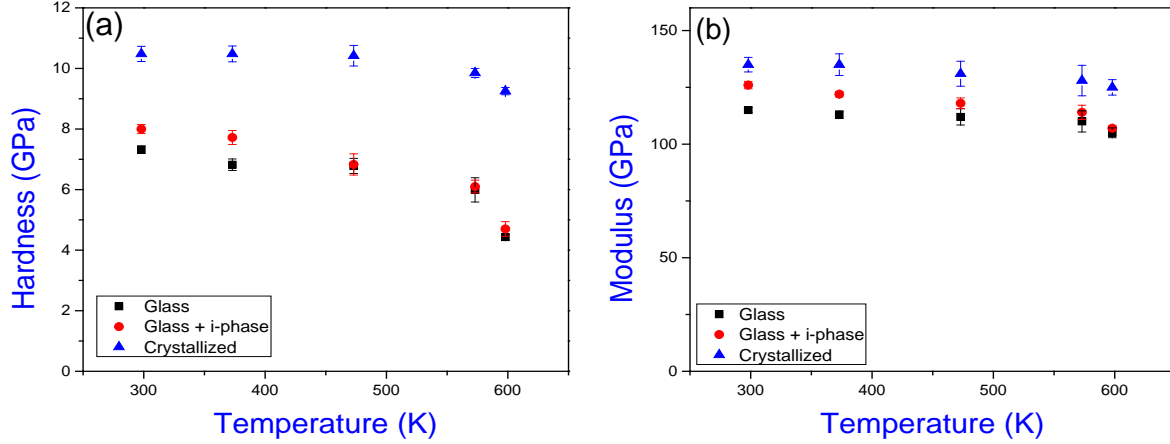


Figure 3.4: (a) Hardness and (b) modulus of glass, glass+i-phase and crystallized at different temperatures.

Figure 3.5 shows the loading curve of the samples at different temperature. The as cast sample shows non-uniform plastic flow in the loading curve characterized by the displacement at constant load (pop in event). Each single event of pop in is designated as formation of shear band which is the unit of plastic deformation in the glass like dislocation in crystalline material. From the plot in Figure 3.5, it can be observed the as cast glass shows maximum frequency of shear band formation and increases with increasing the temperature till 473K then decreases. At 598K the loading curve indicates a uniform deformation. This indicates change in deformation mechanism. The serrated flow is designated as heterogeneous deformation characterized by linear elastic flow followed by shear band formation whereas uniform plastic flow as homogeneous deformation which occur by Newtonian or non-Newtonian flow of the material. Rate of change in hardness also can be attributed to the change in deformation mechanism.

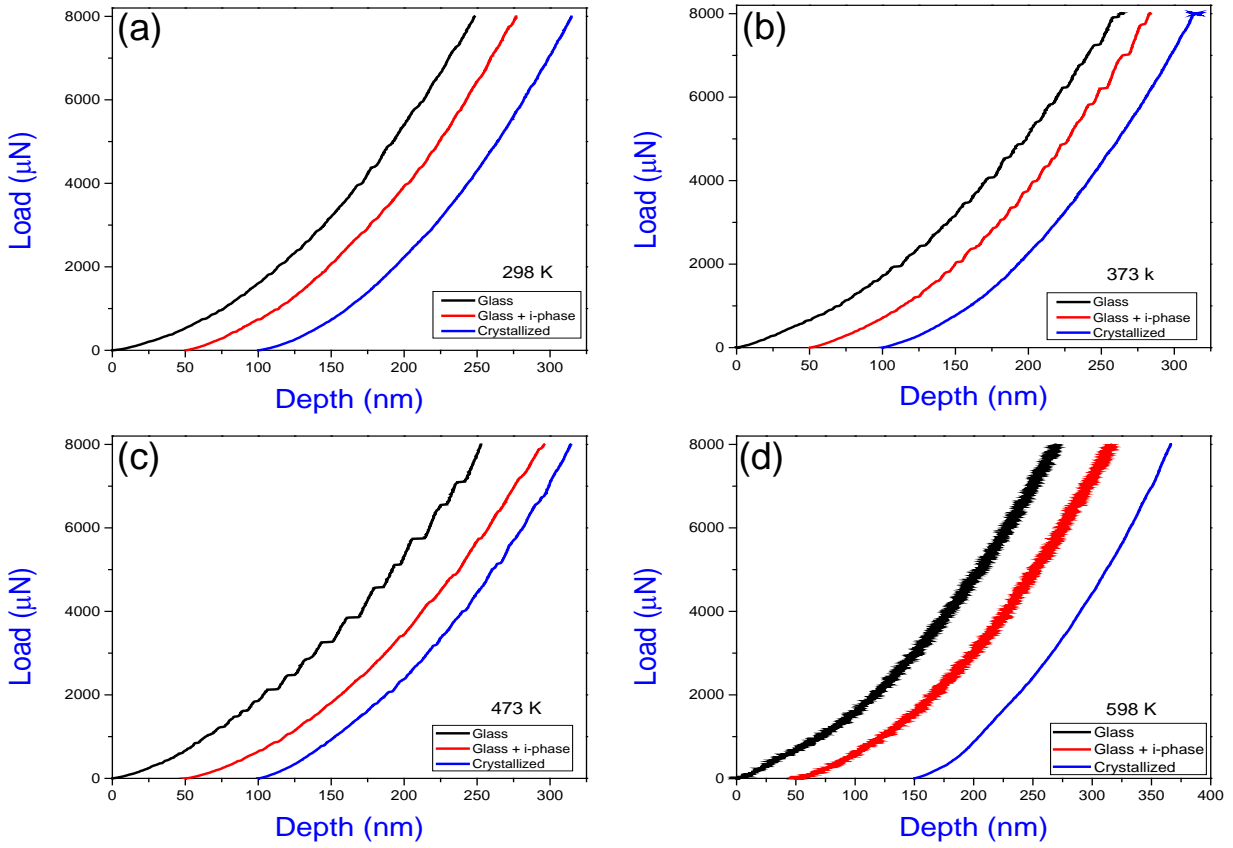


Figure 3.5: Loading curve of glass, glass+i-phase, and crystallized sample at (a) 298K, (b) 373K, (c) 473K, and (d) 598K.

Annealed glass also shows discrete displacement burst in the loading curve like the as cast glass but the frequency is lesser at all the temperature. The glass with i-phase particle shows maximum frequency at 373 K (Figure 3.5) whereas the as cast glass shows maximum frequency at 473 K. which indicates the change in deformation occurred at lower temperature compared to the glass could be due to the free volume associated with the glass in as cast condition and get eliminated when the glass is annealed.

3.5. Conclusions

The current study demonstrates that devitrification in one of the best known metallic glass formers, Vitreloy1 ($\text{Zr}_{41.2}\text{Ti}_{13.8}\text{Cu}_{12.5}\text{Ni}_{10.0}\text{Be}_{22.5}$), proceeds via primary nucleation of a metastable icosahedral phase followed by eutectic mode of crystallization in the remaining supercooled liquid. The icosahedral phase is richer in Ti and depleted in Be compared to the starting amorphous alloy. The remaining Be-enriched and Ti-depleted supercooled liquid transforms to thermodynamically stable crystalline phases including ZrBe_2 , Zr_2Cu , and Ti_2Ni . The sharp interfaces (< 5 nm) between the different crystallized phases support the eutectic mode of crystallization. The devitrification pathway via the formation of icosahedral phase is attributed to the “strong-liquid” behavior of this alloy. The *i-phase* showed a slight increase in hardness as compared to the glass. After devitrification, the hardness increased significantly due to nano-sized grains and intermetallic compound formation.

3.6. References

- [1] A. Peker, W.L. Johnson, A highly processable metallic glass: $\text{Zr}_{41.2}\text{Ti}_{13.8}\text{Cu}_{12.5}\text{Ni}_{10.0}\text{Be}_{22.5}$, Appl. Phys. Lett. 63 (1993) 2342-2344.
- [2] R. Busch, S. Schneider, A. Peker, W. Johnson, Decomposition and primary crystallization in undercooled $\text{Zr}_{41.2}\text{Ti}_{13.8}\text{Cu}_{12.5}\text{Ni}_{10.0}\text{Be}_{22.5}$ melts, Appl. Phys. Lett. 67 (1995) 1544-1546.
- [3] M. Macht, N. Wanderka, A. Wiedenmann, H. Wollenberger, Q. Wei, H.J. Fecht, S. Klose, Decomposition of the supercooled liquid of the bulk amorphous alloy $\text{Zr}_{41}\text{Ti}_{14}\text{Cu}_{12.5}\text{Ni}_{10}\text{Be}_{22.5}$, 225 (1996) 65-70.
- [4] S. Schneider, P. Thiyagarajan, W. Johnson, Formation of nanocrystals based on decomposition in the amorphous $\text{Zr}_{41.2}\text{Ti}_{13.8}\text{Cu}_{12.5}\text{Ni}_{10.0}\text{Be}_{22.5}$ alloy, Appl. Phys. Lett. 68 (1996) 493-495.
- [5] R. Busch, Y. Kim, S. Schneider, W.L. Johnson, Atom probe field ion microscope and levitation studies of the decomposition and crystallization of undercooled Zr-Ti-Cu-Ni-Be melts, 225 (1996) 77-82.
- [6] W. Wang, Q. Wei, S. Friedrich, Microstructure, decomposition, and crystallization in $\text{Zr}_{41}\text{Ti}_{14}\text{Cu}_{12.5}\text{Ni}_{10}\text{Be}_{22.5}$ bulk metallic glass, Physical Review B. 57 (1998) 8211.
- [7] J. Pelletier, Van de Moortele B. J Non-cryst Solids. 325 (2003) 187.

- [8] Y. Gao, J. Shen, J. Sun, D. Chen, G. Wang, H. Wang, D. Xing, H. Xian, B. Zhou, Nanocrystallization of Zr–Ti–Cu–Ni–Be bulk metallic glass, *Mater Lett.* 57 (2003) 2341-2347.
- [9] I. Martin, T. Ohkubo, M. Ohnuma, B. Deconihout, K. Hono, Nanocrystallization of Zr 41.2 Ti 13.8 Cu 12.5 Ni 10.0 Be 22.5 metallic glass, *Acta Materialia.* 52 (2004) 4427-4435.
- [10] U. Köster, U. Herold, Crystallization of metallic glasses, *Glassy Metals I*, Springer, 1981, pp. 225-259.
- [11] X. Tang, J. Löffler, W. Johnson, Y. Wu, Devitrification of the Zr 41.2 Ti 13.8 Cu 12.5 Ni 10.0 Be 22.5 bulk metallic glass studied by XRD, SANS, and NMR, *J. Non Cryst. Solids.* 317 (2003) 118-122.
- [12] S. Mridha, D.L. Jaeger, H.S. Arora, R. Banerjee, S. Mukherjee, Evolution of atomic distribution during devitrification of bulk metallic glass investigated by atom probe microscopy, *Mater Lett.* 158 (2015) 99-103.
- [13] D. Kim, W. Kim, E. Park, N. Mattern, J. Eckert, Phase separation in metallic glasses, *Progress in materials science.* 58 (2013) 1103-1172.
- [14] K. Kelton, G. Lee, A.K. Gangopadhyay, R. Hyers, T. Rathz, J. Rogers, M. Robinson, D. Robinson, First X-ray scattering studies on electrostatically levitated metallic liquids: demonstrated influence of local icosahedral order on the nucleation barrier, *Phys. Rev. Lett.* 90 (2003) 195504.
- [15] C.A. Angell, Formation of glasses from liquids and biopolymers, *Science.* 267 (1995) 1924.
- [16] S. Mukherjee, J. Schroers, Z. Zhou, W. Johnson, W. Rhim, Viscosity and specific volume of bulk metallic glass-forming alloys and their correlation with glass forming ability, *Acta materialia.* 52 (2004) 3689-3695.

CHAPTER 4

ATOMIC DISTRIBUTION IN CATALYTIC AMORPHOUS METALS²

4.1. Abstract

The atomic distribution in catalytically active metallic glass alloys, Pd₄₃Cu₂₇Ni₁₀P₂₀ and Pt_{57.5}Cu_{14.7}Ni_{5.3}P_{22.5}, was investigated using three-dimensional atom probe microscopy. Atom probe analysis showed uniform distribution of constituent elements for both the starting amorphous alloys, with no phase separation. Both the crystallized alloys showed eutectic microstructure with a very sharp interface (~ 0.5 nm as determined from atom probe). The atomic distribution in the devitrified state is explained based on the “fragile liquid” behavior for these noble-metal glassy alloys.

Keywords: Atomic distribution; Metallic glass; Atom probe microscopy; Catalysis

4.2. Introduction

Noble-metal based glassy alloys have attracted lot of interest in recent years due to their high electro-catalytic activity and durability compared to conventional pure metal catalysts [1,2]. Excellent thermo-plastic formability of these alloys allows synthesis of self-supporting nano-wire architecture for energy storage/conversion applications [1,2]. This circumvents the need for support materials (e.g. carbon nano-tubes) that dissolve/degrade under normal operating conditions of electrochemical devices. Further, the chemistry of these alloy systems has been shown to be very active for several electro-catalytic reactions [3,4]. Mapping and controlling the atomic distribution in these novel catalysts will facilitate significant progress in terms of performance, cost and durability of state-of-the-art electrochemical devices. Given their metastable nature, the active species in these bulk metallic glasses (BMGs) can be strategically

²This chapter has been largely adapted from the following journal publication with permission from publisher: “Atomic distribution in catalytic amorphous metals”, Journal of Nanomaterials 16.1 (2015): 438

tailored to achieve further enhancement in their catalytic properties. The type, distribution and length-scale of crystallites formed during controlled devitrification of metallic glasses may be utilized as a toolbox to engineer transformative catalysts for energy storage and conversion.

Pure platinum and palladium in various (nano-) morphologies dispersed on low/high aspect-ratio supports make up majority of electro-catalysts now. Two catalytically active amorphous systems based on these late transition metals include $\text{Pt}_{57.5}\text{Cu}_{14.7}\text{Ni}_{5.3}\text{P}_{22.5}$ and $\text{Pd}_{43}\text{Cu}_{27}\text{Ni}_{10}\text{P}_{20}$. The palladium alloy, $\text{Pd}_{43}\text{Cu}_{27}\text{Ni}_{10}\text{P}_{20}$, is one of the best-known bulk metallic glass (BMG) formers with a critical cooling rate of glass formation as low as 0.1 K/s [5]. Alloy development efforts to replace Pd with Pt led to $\text{Pt}_{57.5}\text{Cu}_{14.7}\text{Ni}_{5.3}\text{P}_{22.5}$ metallic glass, with critical cooling rate of 20 K/s [6] and high thermo-plastic formability [1]. There are no studies till date on the atomic distribution in these catalytically active alloy systems in the (metastable) amorphous or (thermodynamically stable) devitrified state. Thermodynamic studies suggest a transition from nucleation-controlled to growth-controlled mechanism of crystallization for $\text{Pd}_{43}\text{Cu}_{27}\text{Ni}_{10}\text{P}_{20}$ alloy [7], while devitrification studies in platinum-based BMG has not been reported so far. Detailed investigation of the atomic distribution, composition fluctuations (due to possible phase separation), length-scale of the crystalline phases, and the interface between the crystallites is lacking.

In the current study, we report on the atomic distribution of the two noble-metal based BMGs, $\text{Pd}_{43}\text{Cu}_{27}\text{Ni}_{10}\text{P}_{20}$ and $\text{Pt}_{57.5}\text{Cu}_{14.7}\text{Ni}_{5.3}\text{P}_{22.5}$, investigated using three-dimensional atom-probe (3DAP) microscopy. The distribution of atoms was obtained for the as-cast amorphous (metastable) state and the corresponding (thermodynamically stable) devitrified state. Owing to its atomic-scale resolution, 3DAP technique was used to identify nanometer-scale composition fluctuations and the interface between the different phases upon devitrification of the metallic

glasses. Atom probe analysis was combined with scanning electron microscopy (SEM) and X-ray diffraction (XRD) to study the morphology, chemistry, and distribution of the crystallized phases.

4.3. Experimental

Bulk metallic glasses with nominal composition of $\text{Pd}_{43}\text{Cu}_{27}\text{Ni}_{10}\text{P}_{20}$ and $\text{Pt}_{57.5}\text{Cu}_{14.7}\text{Ni}_{5.3}\text{P}_{22.5}$ were prepared by melting high-purity constituents in vacuum-sealed glass tubes followed by water quenching from a temperature of 1000 °C after appropriate B_2O_3 fluxing. Glass transition (T_g) and crystallization temperature (T_x) for both the alloys were determined using differential scanning calorimetry (DSC) at a heating rate of 20 K/min. The samples were devitrified by heating at rate of 20 K/min above their respective crystallization temperatures in DSC in argon atmosphere. Microstructure analysis was done using Scanning Electron Microscopy (FEI QUANTA 200). X-ray diffraction (XRD) analysis was done using Rigaku III Ultima X-ray diffractometer with Cu-K_α radiation of wavelength 1.54 nm. 3DAP analysis was done to obtain concentration profiles and elemental distribution at different locations/interfaces of the starting amorphous and the crystallized specimens. For 3DAP studies, laser-pulsed local electrode atom probe (LEAP 3000X HR) operating at a wavelength of 532 nm and 12 ps pulse duration was used. Specimens for 3DAP were prepared using focused ion beam (FIB) lift-out technique (FEI Nova 200 dual beam). Atom probe tips were prepared using 30 kV ion beam with annular milling patterns followed by final tip shaping using 5 kV ion beam.

4.4. Results and Discussion

Differential scanning calorimetry (DSC) curves for both the as-cast metallic glasses are shown in Figure 4.1(a) and (b). The glass transition temperature (T_g) and crystallization temperature (T_x) for Pd-based metallic glass was found to be 305 °C and 390 °C respectively, whereas for Pt-based metallic glass, the values were 225 °C and 290 °C respectively. A large

supercooled liquid region ($\Delta T = T_x - T_g$) of 85 °C and 65 °C was found for the Pd alloy and Pt alloy respectively. The wide supercooled liquid region allows thermoplastic forming of these alloys down to a few nanometers. SEM micrographs for the fully crystallized Pd and Pt alloys are shown in Figure 4.1(c) and (d) respectively. The Pt alloy has an acicular eutectic structure whereas Pd alloy has a lamellar eutectic structure with sub-micron length-scale. The difference in the structures may be attributed to the difference in critical cooling rates for the two alloy systems. The critical cooling rate for $\text{Pd}_{43}\text{Cu}_{27}\text{Ni}_{10}\text{P}_{20}$ is two orders of magnitude lower compared to $\text{Pt}_{57.5}\text{Cu}_{14.7}\text{Ni}_{5.3}\text{P}_{22.5}$ metallic glass. Due to the higher cooling rate required for vitrifying $\text{Pt}_{57.5}\text{Cu}_{14.7}\text{Ni}_{5.3}\text{P}_{22.5}$, it is likely to be further away from its corresponding equilibrium structure compared to the Pd alloy. The acicular structure for the Pt alloy is likely due to its tendency to reduce excess free energy by dissociating into smaller features. Fragmentation of lamellar structure to smaller acicular structure has been reported previously [8]. XRD results for the as-cast and fully crystallized samples of both alloys are shown in Figure 4.2(a) and (b). The as-cast samples show a broad peak indicating fully amorphous structure. It is seen from XRD results that the crystalline products formed in both the alloys are very similar, consisting mostly of metal-metalloid binary phases.

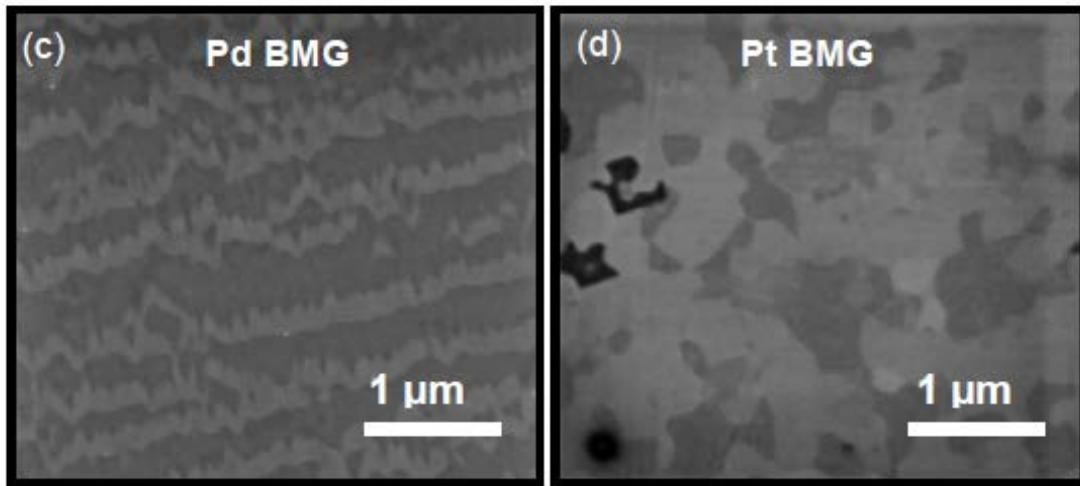
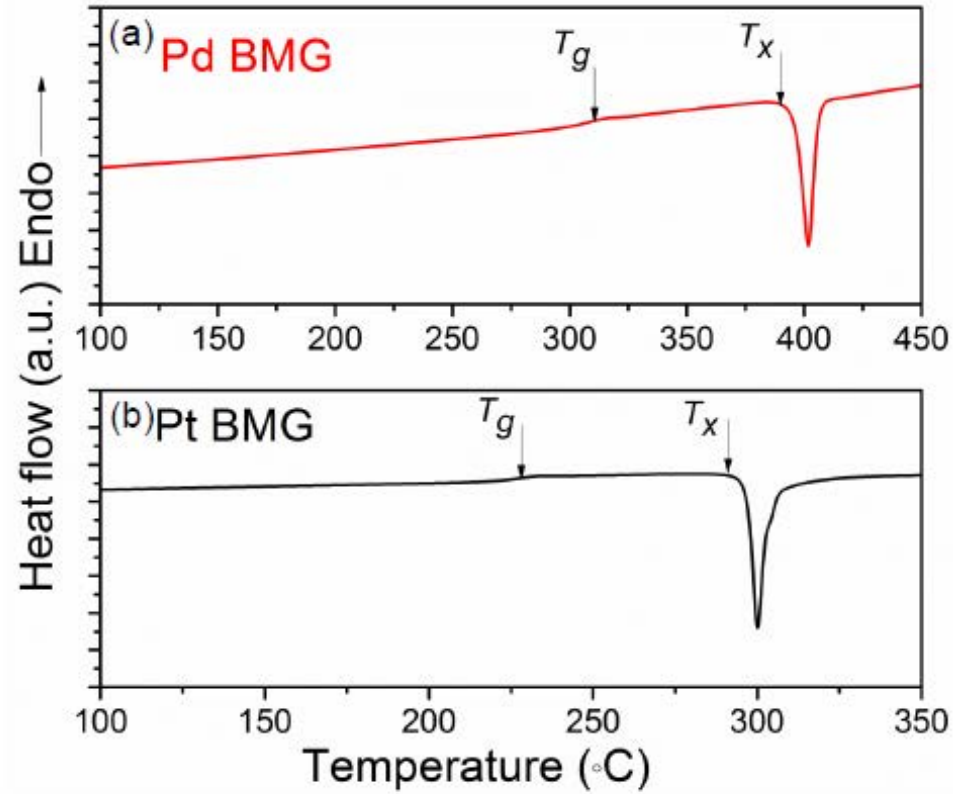


Figure 4.1: DSC curves for (a) $\text{Pd}_{43}\text{Cu}_{27}\text{Ni}_{10}\text{P}_{20}$ metallic glass and (b) $\text{Pt}_{57.5}\text{Cu}_{14.7}\text{Ni}_{5.3}\text{P}_{22.5}$ metallic glass; (c) SEM micrograph for the crystallized $\text{Pd}_{43}\text{Cu}_{27}\text{Ni}_{10}\text{P}_{20}$ alloy; (d) SEM micrograph for the crystallized $\text{Pt}_{57.5}\text{Cu}_{14.7}\text{Ni}_{5.3}\text{P}_{22.5}$ alloy. The glass transition and crystallization temperatures are indicated by T_g and T_x respectively. Pd alloy has a lamellar eutectic structure compared to an acicular eutectic structure for the Pt alloy [9].

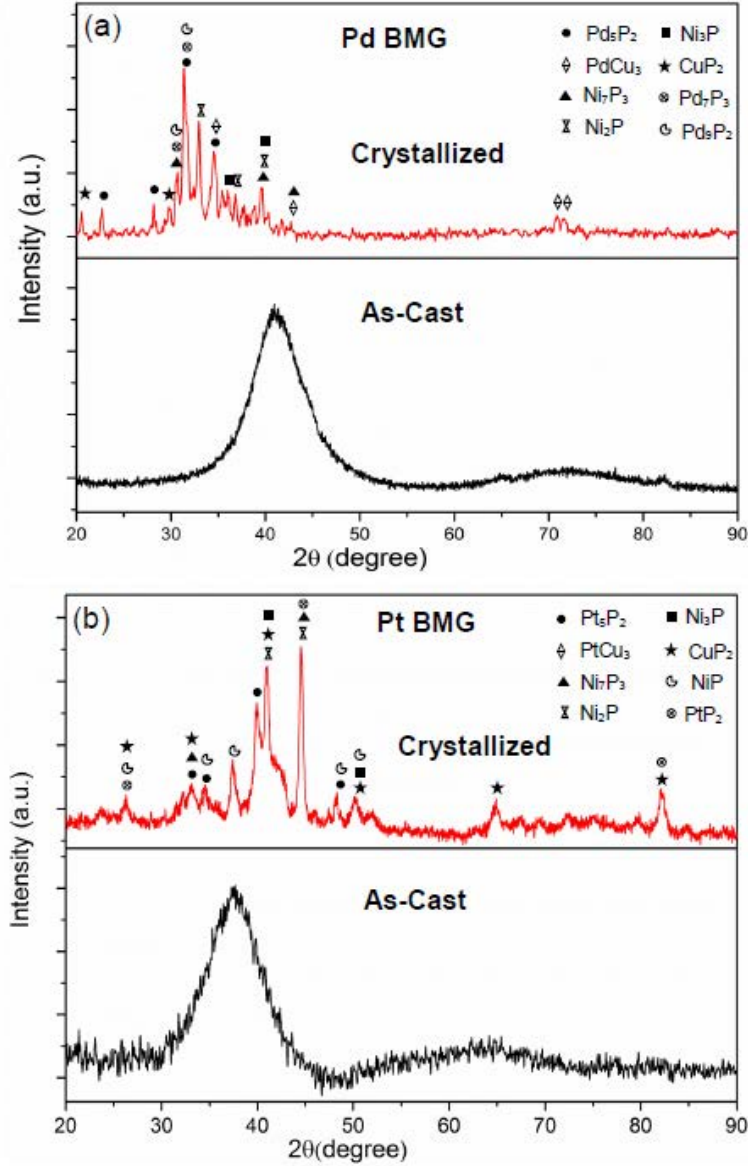


Figure 4.2: XRD analysis curves for (a) $Pd_{43}Cu_{27}Ni_{10}P_{20}$ metallic glass and (b) $Pt_{57.5}Cu_{14.7}Ni_{5.3}P_{22.5}$ metallic glass in as-cast amorphous and crystallized form. The different crystalline phases are marked alongside the XRD peaks [9].

To investigate any nano-scale composition fluctuations in the as-cast metallic glass, atom probe studies were carried out comprising 3D reconstruction and elemental distribution (Figure 4.3). The as-cast structure for both the alloys shows uniform distribution of different elements, without any indication of phase separation. Cyclic voltammetry on these amorphous metal

compositions showed increase in electrochemical surface area (ECSA), which was attributed to de-alloying of less noble constituents [1]. The random mixture of noble/less-noble atoms in the starting amorphous alloy without preferential surface segregation favors dealloying induced surface area enhancement. No evidence of short range ordering is seen, indicating compositional homogeneity down to the atomic scale.

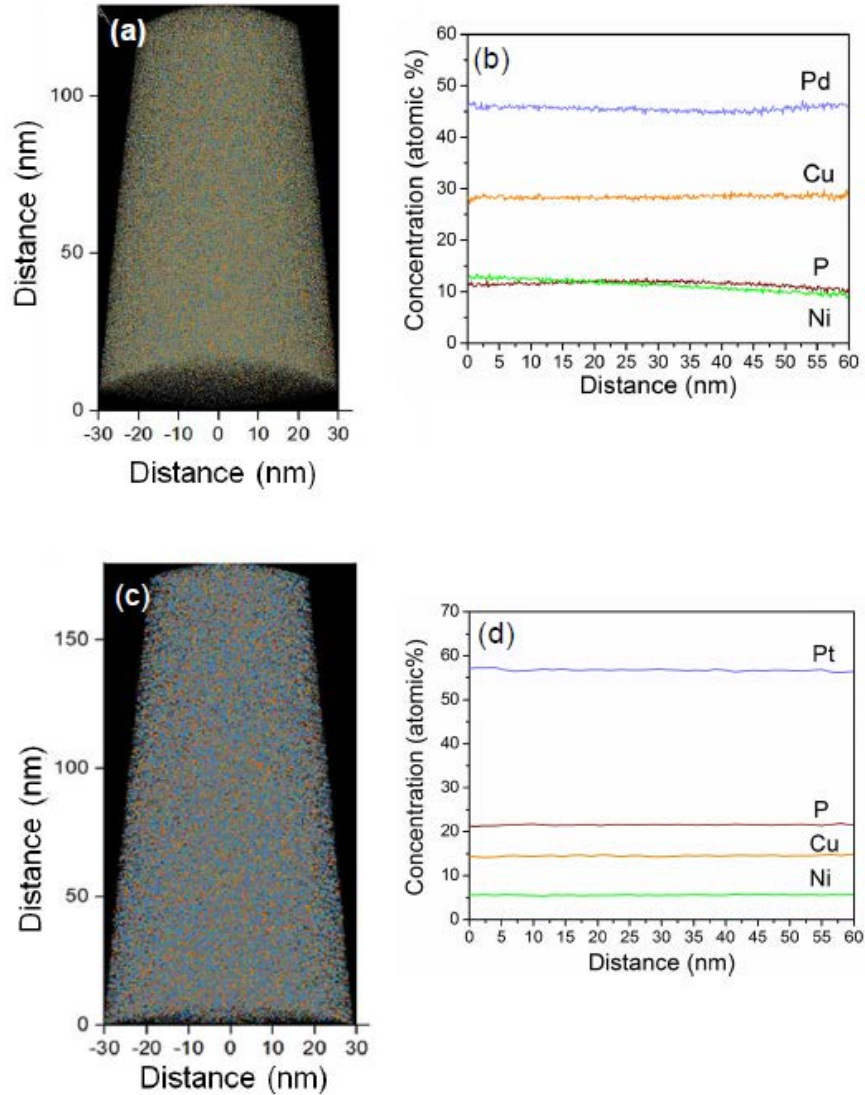


Figure 4.3: (a) 3DAP reconstruction and (b) elemental distribution for as cast $\text{Pd}_{43}\text{Cu}_{27}\text{Ni}_{10}\text{P}_{20}$ metallic glass; (c) 3DAP reconstruction and (d) elemental distribution for as cast $\text{Pt}_{57.5}\text{Cu}_{14.7}\text{Ni}_{5.3}\text{P}_{22.5}$ metallic glass. Atom probe results show homogeneous distribution of all the elements in the as-cast structure of both the alloys [9].

The atom probe results for the crystallized Pd-based metallic glass are shown in Figure 4.4 and summarized in Table 4.1. The LEAP analysis of the fully crystallized alloy showed seven distinct phases - Pd₅P₂, Cu₃Pd, Pd₄Ni₃P₃ and small volume fraction of four complex quaternary phosphides. Earlier reports on crystallization in Pd-Cu-Ni-P alloys also showed the formation of binary, ternary and higher order phosphides [10-13]. The corresponding phases could not be identified in XRD because of lack of database on complex higher order phosphides. The 3DAP reconstruction as well as elemental distribution for crystallized Pt-based metallic glass was very similar to Pd alloy (Figure 4.5). The 3DAP results for crystallized Pt alloy are summarized in Table 4.2. The crystallized microstructure for Pt-based metallic glass comprises of three distinct regions (i) Pt-rich (Pt₃PCu), (ii) P-rich (PtP₂) and (iii) a quaternary phase of Pt-Cu-Ni-P.

Table 4.1: Elemental composition (at. %) obtained using atom probe microscopy of different phases identified in crystallized Pd₄₃Cu₂₇Ni₁₀P₂₀ metallic glass [9]

Elements (atomic %)	Phase 1	Phase 2	Phase 3	Quaternary phosphide phase
Pd	69.9	20.84	39.59	Pd _{48.9} Cu _{16.2} Ni _{8.4} P _{26.7} + Pd _{37.3} Cu _{26.9} Ni _{12.2} P _{23.6} + Pd _{32.4} Cu _{16.3} Ni _{23.1} P _{28.2} + Pd _{44.4} Cu _{24.0} Ni _{9.6} P _{21.9}
Cu	2.0	77.45	0.74	
Ni	0.9	0.00	27.45	
P	27.1	1.7	32.22	
Likely phase	Pd ₇ P ₃	PdCu ₃	Pd ₄ Ni ₃ P ₃	Mixture of quaternary Pd-rich phosphides

Table 4.2: Elemental composition (at. %) obtained using atom probe microscopy of different phases identified in crystallized Pt_{57.5}Cu_{14.7}Ni_{5.3}P_{22.5} metallic glass [9]

Elements (atomic %)	Phase 1	Phase 2	Phase 3
Pt	60.20	33.41	44.52
Cu	17.28	0.06	13.87
Ni	2.05	0.00	19.03
P	20.47	66.54	22.58
Likely phases	Pt ₃ CuP	PtP ₂	Pt-Cu-Ni-P

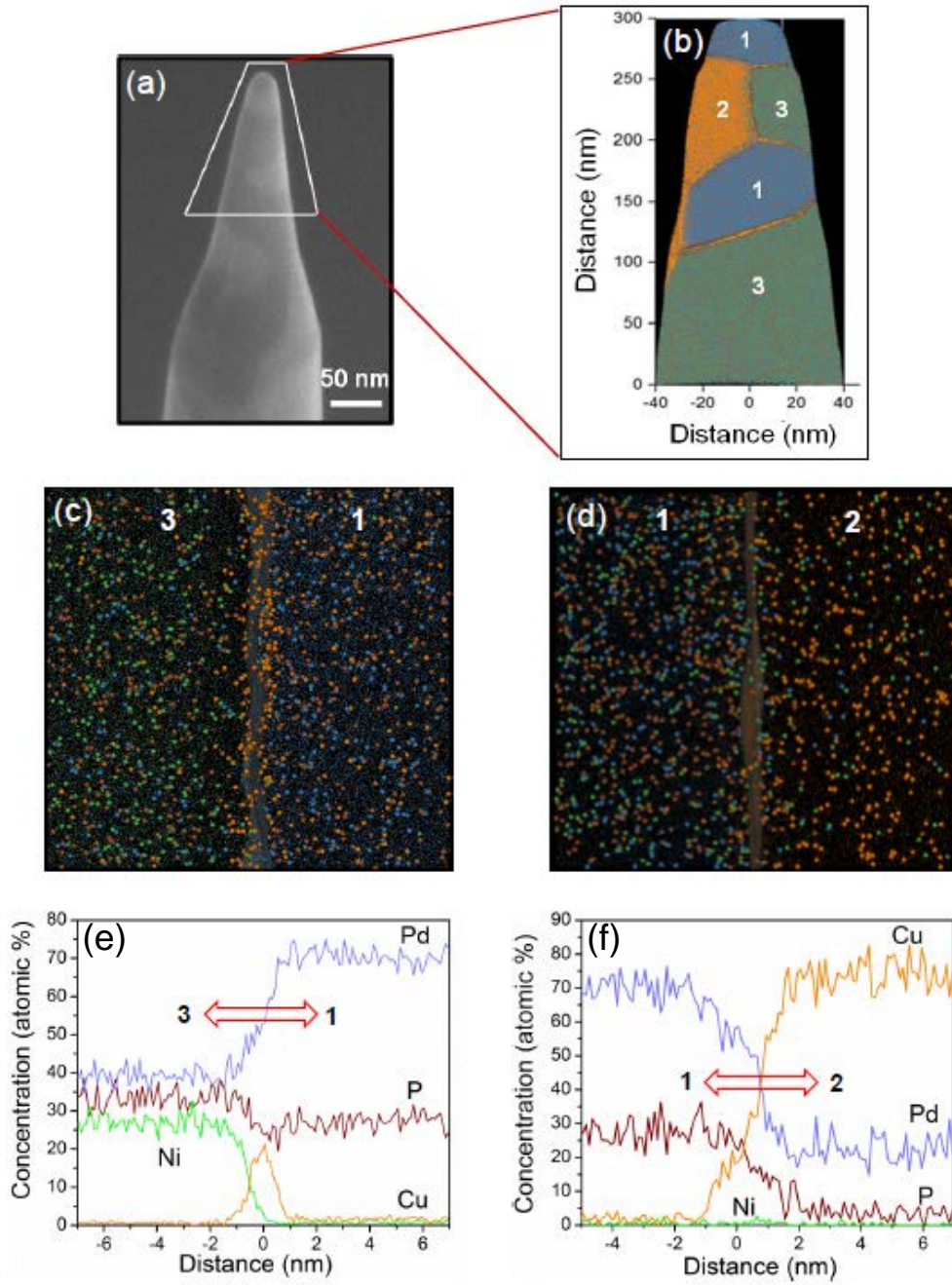


Figure 4.4: (a) SEM image of crystallized $\text{Pd}_{43}\text{Cu}_{27}\text{Ni}_{10}\text{P}_{20}$ metallic glass used for atom-probe microscopy; (b) 3DAP reconstruction for $\text{Pd}_{43}\text{Cu}_{27}\text{Ni}_{10}\text{P}_{20}$ metallic glass crystallized at 450 °C; (c) elemental map and (d) composition profile across the interface between phases “1” and “3”; (e) elemental map and (f) composition profile across the interface between phases “1” and “2”; Phases marked 1, 2 and 3 corresponds to Pd_7P_2 , PdCu_3 and $\text{Pd}_4\text{Ni}_3\text{P}_3$ respectively. The thickness of all the interfaces was found to be less than 0.5 nm [9].

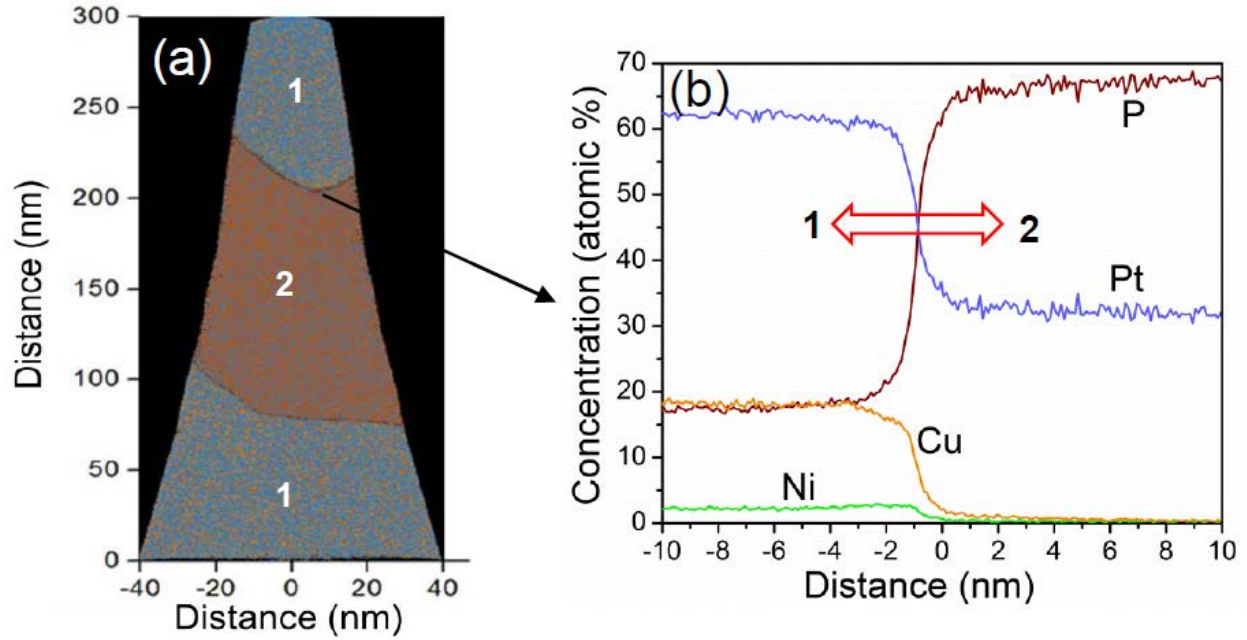


Figure 4.5: (a) 3DAP reconstruction for $Pt_{57.5}Cu_{14.7}Ni_{5.3}P_{22.5}$ metallic glass crystallized at 450 °C; (b) elemental distribution and composition profile across the interface between phases “1” and “2”; Phases marked 1 and 2 corresponds to Pt_3PCu and PtP_2 respectively [9].

The presence of multiple crystalline phases in each of the two metallic glasses (Table 4.1 and 4.2) demonstrate the complexity of phase formation in these alloys. DSC shows a single sharp devitrification peak (Figure 4.1), characteristic of eutectic crystallization, which is seen in microstructure as well. Phase-separation induced crystallization has been reported for a number of different metallic glasses [14]. However, there is no evidence of phase separation in the starting amorphous structure of the metallic glasses investigated in this study. Many of the zirconium-based metallic glasses show two-stage devitrification - primary nucleation of metastable quasi-crystalline phases, followed by transformation of the remaining supercooled liquid to thermodynamically stable phases via secondary crystallization [14,15]. These are typically “stronger” liquids (higher value of fragility parameter), which show significant degree of icosahedral ordering in the undercooled liquid [16,17]. On the contrary, “fragile” glasses [16] such

as $\text{Pd}_{43}\text{Cu}_{27}\text{Ni}_{10}\text{P}_{20}$ and $\text{Pt}_{57.5}\text{Cu}_{14.7}\text{Ni}_{5.3}\text{P}_{22.5}$, show drastic change in liquid properties with change in temperature, particularly close to the glass transition. This favors rapid rearrangement of the smaller metalloid atoms resulting in the formation of multi-component phosphide phases up on devitrification. Multiple phosphide phases formed for both alloys support the “fragile” liquid behavior.

From the atom probe studies, it is seen that the interface between different crystallized regions is very sharp, with a width of less than 0.5 nanometers. It has been reported previously that a sharp interface (atomically thin) between the different crystallized phases indicate eutectic mode of crystallization, where interface diffusion plays a more dominant role compared to volume diffusion [18]. From the elemental distribution in $\text{Pd}_{43}\text{Cu}_{27}\text{Ni}_{10}\text{P}_{20}$ (Figure 4.4(c) through (f)), it is seen that Cu preferentially segregates at the interface between $\text{Pd}_4\text{Ni}_3\text{P}_3$ (region marked “3”) and Pd_7P_3 (region marked “1”). Therefore, Cu not only forms Cu_3Pd but also segregates to the interface between the non-Cu containing phases. Solid solubility of Pd and Ni in Cu is high, whereas that of P is low [19]. Therefore, copper segregation (between $\text{Pd}_4\text{Ni}_3\text{P}_3$ and Pd_7P_3) is likely due to its low solubility with phosphorus and high diffusivity. Copper segregation at the interface has been reported during crystallization of some other metallic glass compositions as well [20]

4.5. Conclusions

Atomic distribution in catalytically active BMGs, $\text{Pd}_{43}\text{Cu}_{27}\text{Ni}_{10}\text{P}_{20}$ and $\text{Pt}_{57.5}\text{Cu}_{14.7}\text{Ni}_{5.3}\text{P}_{22.5}$, was studied using three-dimensional atom-probe microscopy in as-cast amorphous and fully crystallized state. The following conclusions may be drawn based on the obtained results:

- 1) Both the alloys show uniform distribution of constituent elements in the starting amorphous structure, indicating no phase separation.

- 2) The Pt alloy showed an acicular eutectic microstructure while the Pd alloy showed a lamellar eutectic structure, which may be attributed to the difference in their critical cooling rates.
- 3) A very sharp interface (~ 0.5 nm as determined from atom probe) was found between the different crystallized phases, which support the eutectic mode of crystallization, where interface diffusion plays a more dominant role compared to volume diffusion.
- 4) The formation of mostly metal-metalloid phosphide phases may be attributed to the “fragile” liquid behavior of both the alloys.

4.6. References

- [1] M. Carmo, R.C. Sekol, S. Ding, G. Kumar, J. Schroers, A.D. Taylor, Bulk metallic glass nanowire architecture for electrochemical applications, *Acs Nano*. 5 (2011) 2979-2983.
- [2] S. Mukherjee, R.C. Sekol, M. Carmo, E.I. Altman, A.D. Taylor, J. Schroers, Tunable Hierarchical Metallic-Glass Nanostructures, *Advanced Functional Materials*. 23 (2013) 2708-2713.
- [3] R. Jiang, D.T. Tran, J.P. McClure, D. Chu, A class of (Pd–Ni–P) electrocatalysts for the ethanol oxidation reaction in alkaline media, *ACS Catalysis*. 4 (2014) 2577-2586.
- [4] L. Ding, A. Wang, G. Li, Z. Liu, W. Zhao, C. Su, Y. Tong, Porous Pt–Ni–P composite nanotube arrays: highly electroactive and durable catalysts for methanol electrooxidation, *J. Am. Chem. Soc.* 134 (2012) 5730-5733.
- [5] J. Schroers, W.L. Johnson, R. Busch, Crystallization kinetics of the bulk-glass-forming Pd 43 Ni 10 Cu 27 P 20 melt, *Appl. Phys. Lett.* 77 (2000) 1158-1160.
- [6] J. Schroers, W.L. Johnson, Highly processable bulk metallic glass-forming alloys in the Pt–Co–Ni–Cu–P system, *Appl. Phys. Lett.* 84 (2004) 3666-3668.
- [7] J. Schroers, Y. Wu, R. Busch, W. Johnson, Transition from nucleation controlled to growth controlled crystallization in Pd 43 Ni 10 Cu 27 P 20 melts, *Acta Materialia*. 49 (2001) 2773-2781.
- [8] R. Goetzinger, M. Barth, D. Herlach, Mechanism of formation of the anomalous eutectic structure in rapidly solidified Ni–Si, Co–Sb and Ni–Al–Ti alloys, *Acta materialia*. 46 (1998) 1647-1655.
- [9] S. Mridha, D.L. Jaeger, H.S. Arora, R. Banerjee, S. Mukherjee, Atomic distribution in catalytic amorphous metals, *Journal of Nanomaterials*. 16 (2015) 438.

- [10] C. Ma, N. Nishiyama, A. Inoue, Phase Equilibria and Thermal Stability of Pd-Cu-Ni-P Alloys. *Materials Transactions*. 43 (2002) 1161-1165.
- [11] J. Kim, S. Kim, A. Inoue, In situ observation of solidification behavior in undercooled Pd-Cu-Ni-P alloy by using a confocal scanning laser microscope, *Acta materialia*. 49 (2001) 615-622.
- [12] N. Nishiyama, A. Inoue, Nucleation and Growth Behavior of Undercooled Pd₄₂. 5Cu₃₀Ni₇. 5P₂₀ Melt. *Materials Transactions*. 43 (2002) 1247-1249.
- [13] I. Lu, G. Wilde, G. Görler, R. Willnecker, Thermodynamic properties of Pd-based glass-forming alloys, *J. Non Cryst. Solids*. 250 (1999) 577-581.
- [14] D. Kim, W. Kim, E. Park, N. Mattern, J. Eckert, Phase separation in metallic glasses, *Progress in materials science*. 58 (2013) 1103-1172.
- [15] I. Martin, T. Ohkubo, M. Ohnuma, B. Deconihout, K. Hono, Nanocrystallization of Zr 41.2 Ti 13.8 Cu 12.5 Ni 10.0 Be 22.5 metallic glass, *Acta Materialia*. 52 (2004) 4427-4435.
- [16] C.A. Angell, Formation of glasses from liquids and biopolymers, *Science*. 267 (1995) 1924.
- [17] S. Mukherjee, J. Schroers, Z. Zhou, W. Johnson, W. Rhim, Viscosity and specific volume of bulk metallic glass-forming alloys and their correlation with glass forming ability, *Acta materialia*. 52 (2004) 3689-3695.
- [18] U. Köster, U. Herold, Crystallization of metallic glasses, *Glassy Metals I*, Springer, 1981, pp. 225-259.
- [19] J.R. Davis, *Copper and Copper Alloys*, ASM international, 2001.
- [20] T. Kulik, Nanocrystallization of metallic glasses, *J. Non Cryst. Solids*. 287 (2001) 145-161.

CHAPTER 5

HIGH TEMPERATURE NANO-MECHANICAL BEHAVIOR OF BULK METALLIC GLASSES

5.1. Abstract

High temperature nano-mechanical behavior of two Zr-based bulk metallic glasses (BMGs) was investigated in the range of room temperature (RT) to glass transition. The hardness decreased slightly until $0.9T_g$ (reduction by $\sim 15\%$ compared to RT) followed by a drastic drop (by a factor of three) beyond that until T_g . There was slight reduction in elastic modulus over the same range. The deformation mechanism changed from inhomogeneous or serrated flow to homogenous flow near $0.9T_g$. The creep activation energy for Vitreloy1 and Vitreloy105 were 144 kJ/mol and 125 kJ/mol, respectively in the range of room temperature to $0.75T_g$. The apparent activation energy increased drastically to 192 kJ/mol for Vitreloy1 and 215 kJ/mol for Vitreloy105 in the range of $0.9T_g$ to T_g , indicating a change in creep mechanism. In the low temperature range, activation energy for creep is likely dictated by cooperative migration of atomic clusters while self-diffusion of atoms dominates the creep deformation at high temperatures.

Keywords: Nanoindentation; Bulk metallic glass; Creep; Characterization

5.2. Introduction

Bulk metallic glasses (BMGs) are emerging structural materials due to their high strength, large elastic deflection, good corrosion resistance, and excellent thermo-plastic processing ability [1-4]. The deformation mechanism of metallic glass can be homogenous or inhomogeneous depending on temperature and strain rate [5,6]. BMGs show serrated flow, which reflects the dominance of shear band nucleation kinetics at low-temperatures [6-8]. Recently, several researchers have been studying the deformation mechanism of BMGs using nano-indentation. The

instrument records the displacement with respect to the applied load while performing the experiment.

However, most studies on mechanical behavior of BMGs are narrowed to a low-temperature range well below the glass transition temperature. Additionally, creep studies on BMGs using nano-indentation are rare [9-11]. It is important to examine creep behavior at a sub-micrometer level for application of MEMS, NEMS, and associated practical engineering challenges. Furthermore, the apparent activation energy of amorphous structure is dependent upon temperature. Thus, high temperature nano-indentation studies of BMGs is important to gain further insight into deformation behavior.

In this study, we investigated nano-mechanical behavior of BMGs over a variety of temperatures, Vitreloy 1 with the composition and vitreloy 105 with the composition $\text{Zr}_{52.5}\text{Ti}_5\text{Cu}_{17.9}\text{Ni}_{14.6}\text{Al}_{10}$ were chosen. We discussed the hardness and elastic modulus variation with increasing temperature for both the alloys. We also investigated the creep behaviors of the two alloys. Furthermore, the apparent activation energy of creep was evaluated at different levels of temperature zones. The deformation mechanisms of BMGs are discussed.

5.3. Experimental

Amorphous alloy with composition $\text{Zr}_{41.2}\text{Ti}_{13.8}\text{Cu}_{12.5}\text{Ni}_{10}\text{Be}_{22.5}$ was produced using arc melting technique followed by Cu mold suction casting. Glass transition and crystallization temperatures were determined using DSC with a heating rate of 20K/min. The hardness, modulus, and minimum creep rate of the amorphous alloys were determined using nano-indentation technique (Hysitron). The room temperature and elevated temperature indentations were performed on Hysitron xsol-stage, which is incorporated with top and bottom heating plates. The indentations were performed using a berkovich tip. The tip has a pyramidal shape and is embedded

in a 20 mm long glass holder to keep the transducer away from the elevated temperature. The indentations were performed at 8000 μN and temperatures up to 623 K. Two different load functions were used, 5s loading-2s holding-5s unloading and 5s loading -10s holding – 0.5s unloading. Samples for nano-indentation were prepared from the as-cast sample. The samples were cut from the cast amorphous alloy with the desired shape and were subsequently rough polished with SiC, followed by final polishing in 1 μm diamond suspension. Then the samples were polished in the Vibromet for 24h in a 0.04 μm colloidal silica suspension.

5.4. Results and Discussion

The DSC analysis was performed for the amorphous alloys with the composition $\text{Zr}_{41.2}\text{Ti}_{13.8}\text{Cu}_{12.5}\text{Ni}_{10}\text{Be}_{22.5}$, commercially known as Vitreloy 1, and $\text{Zr}_{52.5}\text{Ti}_5\text{Cu}_{17.9}\text{Ni}_{14.6}\text{Al}_{10}$, known as Vitreloy 105. The DSC analysis indicates an endothermic glass transition followed by exothermic peak, indicating crystallization of the glass phase. The calorimetric glass transition were found to be 623 K for Vitreloy 1 and 673 K for Vitreloy 105.

Figure 5.1 shows the hardness and modulus of the two glass as function of T_g in Kelvin (K) scale. It can be observed that both the alloys show very slight changes in hardness and modulus up to $0.9T_g$, below that the hardness decreases sharply whereas the modulus shows very small decrease. The load-displacement curve of the alloys are closely inspected to gain insight on the deformation mechanism.

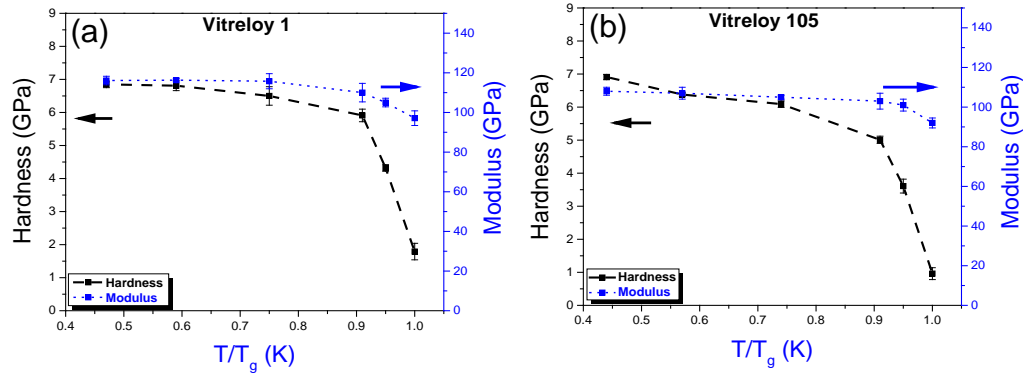


Figure 5.1: The hardness and modulus of the (a) Vitreloy 1 and (b) Vitreloy 105 as function of T_g . Both the glass show decrease in hardness and modulus with increasing temperature.

Figure 5.2 shows the loading part of the load-displacement curve. The origin of the curves have been shifted for clarity of presentation. The same loading rate has been used for indentation at all temperatures. The nature of load-displacement curves varies with temperature. It can be observed that the room temperature curves show serrated plastic flow, which can contribute to the formation of shear bands. The shear band is responsible for plastic deformation in metallic glass.

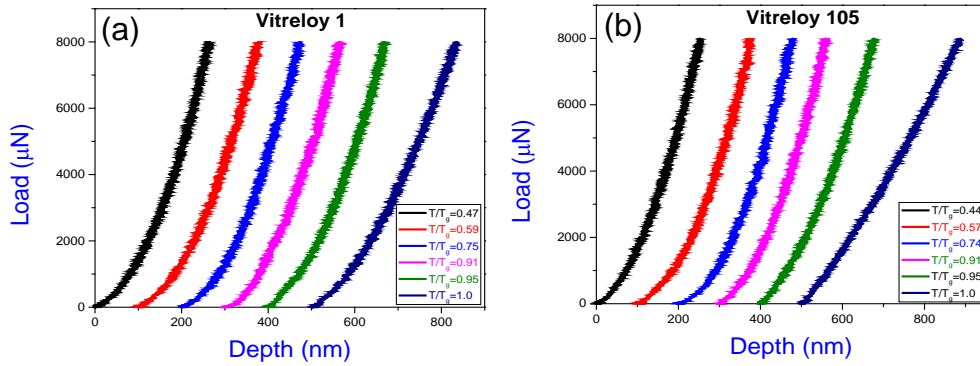


Figure 5.2: Loading curve of (a) Vitreloy 1 and (b) Vitreloy 105 at different at different temperature as function of T_g . Both the glass show serrated plastic deformation at lower temperature (up to $0.91T_g$) due to formation of shear band. At higher temperature ($0.95T_g$) the glass shows uniform plastic deformation as the glass behave as Newtonian fluid at higher temperature.

At $0.91T_g$ the curve shows smooth deformation indicating a change in deformation mechanism from shear band formation to homogenous Newtonian flow. The $0.91T_g$ can be marked as the transition temperature with respect to deformation behavior. But below that temperature, it is observed that increase in serration frequency are accompanied with increase in temperature. In earlier studies, it has been reported that increase in serration step is contributed to the kinetics of the shear band formation [12]. At $0.44T_g$ the nucleation rate of shear band is very high which leads to formation of multiple shear bands at a time; whereas, with an increase in temperature up to transition temperature, the nucleation rate of shear band decreases leading to formation of single shear band at a time. The serration steps in the loading curve are associated to formation of each single shear band at intermediate temperatures. Whereas it has been concluded at $0.44T_g$ each single step represents formation of multiple shear bands together. It has by earlier study the strain required to nucleate a shear band increase with increase in temperature [12].

The creep displacement and creep rate plot versus time for Vitreloy 1 and Vitreloy 105 are shown in Figure 5.3. The plots show the variation in displacement and strain rate in temperature range of $0.4T_g$ to T_g . The displacement in both the alloys increases with time. There is a positive correlation between displacement increase rate and temperature. The rate of increase in displacement is not much up to $0.75T_g$. As the temperature increases at 0.9 and $0.95T_g$, the displacement significantly increases, and a sharp increase at T_g . The observed creep displacement in Vitreloy 105 is more than Vitreloy 1. The creep strain rate also confirms the high displacement rate at higher T_g for both the alloys. The minimum creep rate of Vitreloy 1 and Vitreloy 105 has a range of 10^{-14} to 10^{-5} s^{-1} for 0.4 to $0.75 T_g$. The minimum creep rate of Vitreloy 1 is 0.006 which is lower than minimum creep rate of 0.009 for Vitreloy 105 at T_g (shown in Figure 5.4). Further, minimum creep rate can be expressed as

$$\dot{\epsilon} = A \exp(-Q_{app}/kT) \sigma^n \quad (1)$$

where A is the pre-exponent constant, Q_{app} is the apparent activation energy of creep, k is the Boltzmann constant, and T is the absolute temperature. The apparent activation energy of creep is calculated by experimental data of creep tests at different temperatures by keeping the same stress level, as shown in *Figure 5.5*. The apparent activation energy of creep estimated from the slope of minimum creep rate versus temperature is classified in two sections based on the fitting straight line for both Vitreloy 1 and Vitreloy 105. In the $0.4T_g$ to $0.75T_g$ range, the obtained apparent activation energy for Vitreloy 1 and Vitreloy 105 are 144 kJ/mol and 125 kJ/mol, respectively. In addition, the apparent activation energy increased to 192 kJ/mol for Vitreloy 1 and 215 kJ/mol for Vitreloy 105 in the $0.91T_g$ to T_g range. The change in activation energy at a higher temperature range can be attributed to a change in deformation mechanism. The lower values of activation energy at low temperature range maybe explained from the movement of small atomic clusters and deformation occurs via cooperative migration of these clusters. In contrast, at high temperature self-diffusion of atoms dominates the creep deformation and results in higher activation energy. Therefore, the creep mechanism near glass transition is different compared to the dominating processes at low temperatures.

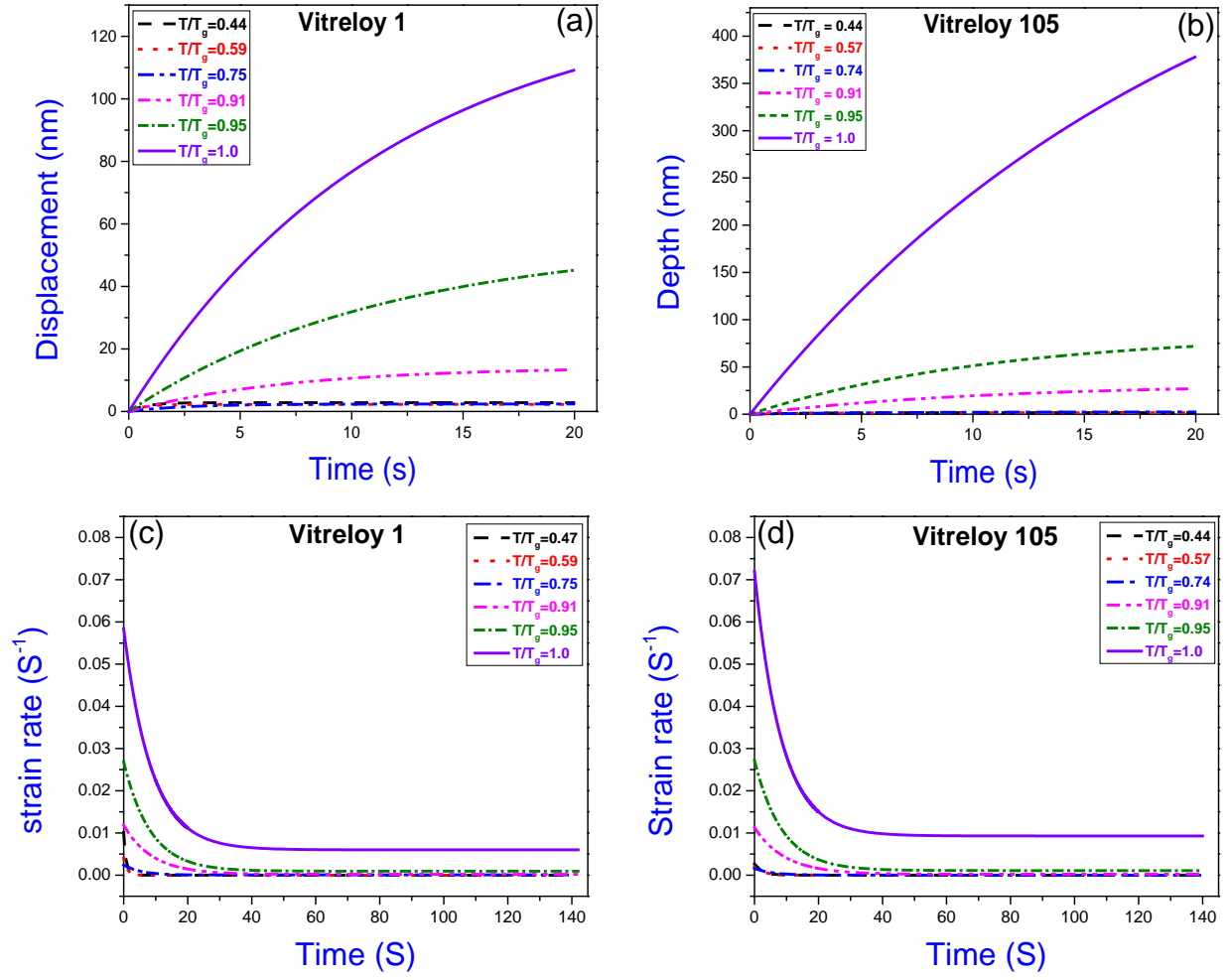


Figure 5.3: Displacement vs time plot at constant load of 8000 μN at different temperature as a function of T_g for (a) Vitreloy 1 (b) Vitreloy 105 shows an increase in displacement rate at higher temperature (above $0.91T_g$).

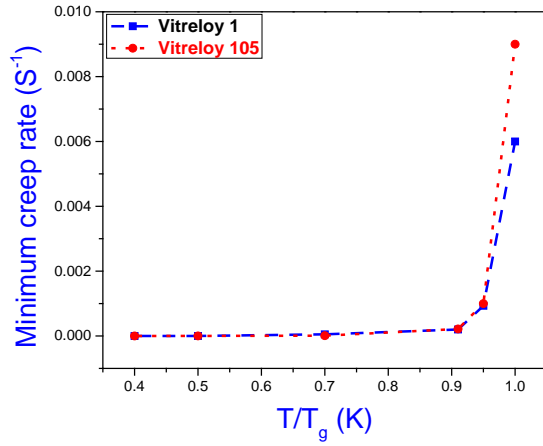


Figure 5.4: Minimum creep rate of Vitreloy 1 and Vitreloy 105 at different temperature as function of T_g . Vitreloy 1 shows lower minimum creep than Vitreloy 105 at all temperature.

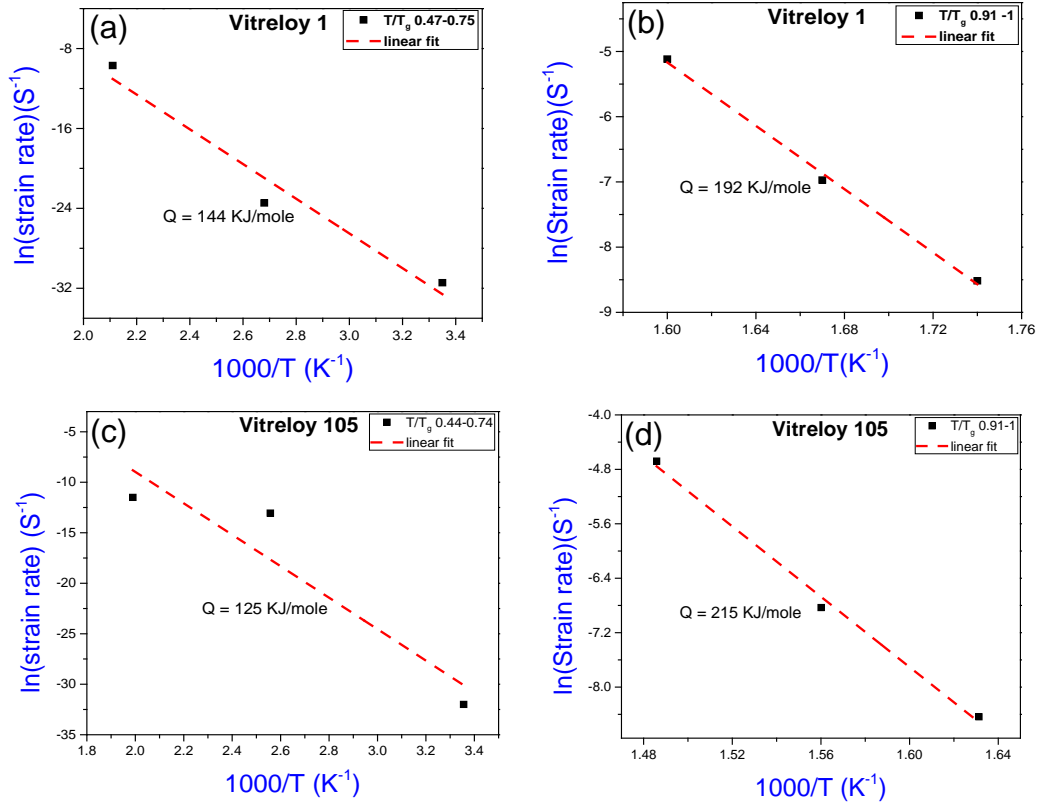


Figure 5.5: $\ln(\text{strain rate})$ vs T plot to evaluate the apparent activation energy of creep for the glass. As the deformation mechanism changes the activation energy also get changed. (a) Vitreloy 1 $0.4-0.74T_g$, (b) Vitreloy 1 $0.91T_g - T_g$, (c) Vitreloy 105 $0.4-0.74T_g$, and (d) Vitreloy 105 $0.91T_g - T_g$.

5.5. Conclusions

Nano-mechanical studies of Vitreloy 1 and vitreloy 105 bulk metallic glasses were carried out over a wide range of temperatures. The creep behavior of Vitreloy 1 and Vitreloy 105 was investigated well below and near the glass transition temperature. Hardness was found to significantly decrease at T_g while elastic modulus decreased slightly with increasing temperature. The deformation mechanism changes from inhomogeneous or serrated flow to homogeneous flow near $0.9T_g$. In the low temperature range, activation energy for creep is likely dictated by cooperative migration of atomic clusters while self-diffusion of atoms dominates the creep deformation at high temperatures.

5.6. References

- [1] A.L. Greer, Metallic glasses, *Science*. 267 (1995) 1947.
- [2] W.L. Johnson, Bulk glass-forming metallic alloys: Science and technology, *MRS Bull.* 24 (1999) 42-56.
- [3] A. Inoue, Stabilization of metallic supercooled liquid and bulk amorphous alloys, *Acta materialia*. 48 (2000) 279-306.
- [4] J. Schroers, Processing of bulk metallic glass, *Adv Mater.* 22 (2010) 1566-1597.
- [5] F. Meng, K. Tsuchiya, I. Seichiro, Y. Yokoyama, Reversible transition of deformation mode by structural rejuvenation and relaxation in bulk metallic glass, *Appl. Phys. Lett.* 101 (2012) 121914.
- [6] C.A. Schuh, A.C. Lund, T. Nieh, New regime of homogeneous flow in the deformation map of metallic glasses: elevated temperature nanoindentation experiments and mechanistic modeling, *Acta Materialia*. 52 (2004) 5879-5891.
- [7] C. Schuh, T. Nieh, A nanoindentation study of serrated flow in bulk metallic glasses, *Acta Materialia*. 51 (2003) 87-99.
- [8] C.A. Schuh, T.C. Hufnagel, U. Ramamurty, Mechanical behavior of amorphous alloys, *Acta Materialia*. 55 (2007) 4067-4109.
- [9] A. Concustell, J. Sort, A. Greer, M. Baró, Anelastic deformation of a Pd 40 Cu 30 Ni 10 P 20 bulk metallic glass during nanoindentation, *Appl. Phys. Lett.* 88 (2006) 171911.
- [10] W. Li, K. Shin, C. Lee, B. Wei, T. Zhang, Y. He, The characterization of creep and time-dependent properties of bulk metallic glasses using nanoindentation, *Materials Science and Engineering: A*. 478 (2008) 371-375.

- [11] B. Wei, T. Zhang, W. Li, D. Xing, L. Zhang, Y. Wang, Indentation creep behavior in Ce-based bulk metallic glasses at room temperature, *Materials transactions*. 46 (2005) 2959-2962.
- [12] C.A. Schuh, A.C. Lund, T. Nieh, New regime of homogeneous flow in the deformation map of metallic glasses: elevated temperature nanoindentation experiments and mechanistic modeling, *Acta Materialia*. 52 (2004) 5879-5891.
- [13] J. Lu, G. Ravichandran, W.L. Johnson, Deformation behavior of the Zr 41.2 Ti 13.8 Cu 12.5 Ni 10 Be 22.5 bulk metallic glass over a wide range of strain-rates and temperatures, *Acta materialia*. 51 (2003) 3429-3443.

CHAPTER 6

STRAIN GRADIENT PLASTICITY IN MULTI-PRINCIPAL ELEMENT ALLOYS

6.1. Abstract

Strain gradient plasticity effects that become important during deformation in small volumes have not been reported for multi-principal element alloys. Strain gradient plasticity of two alloys, CoCrFeMnNi and CoCrNi, was investigated in work hardened, and annealed conditions by nano-indentation. The three-component alloy exhibited higher hardness and modulus as compared to the five-component alloy, and the hardness of both the alloys demonstrated significant dependence on indentation depth. This depth dependence was explained by geometrically necessary dislocations (GND) that result from the high strain gradients due to the shape of the indenter. The characteristic length scale of GNDs for multi-principal element alloys was found to be smaller compared pure Ni for both the work hardened and annealed conditions.

Keywords: Multi-principal element alloy; geometrically necessary dislocation; Nano-indentation.

6.2. Introduction

Multi-Principal Element alloys (MPEAs) represent a new generation of material system with multiple principal elements in equimolar (or near equimolar) proportions and very promising engineering properties [1-6]. They form simple solid solutions due to high mixing entropy, which suppresses the formation of complex intermetallic compounds [5]. The mechanical properties of MPEAs have been widely studied in recent years over a range of temperatures for potential applications in nuclear and aerospace industries. These include tensile/compressive properties, fatigue behavior and fracture toughness. [6-8]. However, strain gradient plasticity effects that become important during deformation in small volumes have not been reported for MPEAs. In crystalline metals and alloys, dislocations dominate the plastic deformation behavior. Total

dislocation density during deformation is the sum of those created from the effective strain in the material and the ones resulting from geometrical confinement. [9-15]. How dislocations are created and interact in a geometrically confined environment provides valuable insights into the strain hardening behavior of the material along with strain gradient plasticity mechanisms. Nano-indentation hardness of a material is typically used as a measure of its resistance to plastic deformation. For crystalline metals, nano-indentation hardness shows an inverse relation with indentation depth, typically referred to as indentation size effect (ISE). [9-15] This is attributed to geometrically necessary dislocations that result from large strain gradients during shallow indentation (of the order of nanometers). Investigating indentation size effects is critical in understanding dislocation interactions in the highly-disordered crystal lattices of MPEAs.

Here, we report on strain gradient plasticity and nano-indentation size effects for two equimolar alloys, namely CoCrNi and CoCrFeMnNi, which form face centered cubic (FCC) solid solutions. Nano-mechanical behavior of the two alloys was studied in dislocation-free annealed condition as well as after work hardening. Comparisons of the two equimolar alloys were made with a pure metal, Ni, to understand solid solution strengthening effects.

6.3. Experimental

The equimolar CoCrNi and CoCrFeMnNi alloys were prepared by arc-melting followed by drop casting. The equimolar alloys and pure Ni (99.99%) were subsequently subjected to 70% thickness reduction by cold rolling. The cold rolled samples were annealed at 900 °C for 20 hours. The work hardened and annealed samples were prepared for microstructure and nano-mechanical studies by polishing with SiC paper followed by final polishing with 1 μm diamond suspension and 0.04 μm colloidal silica suspension. Crystal structure and phase identification were done using Rigaku III Ultima X-ray diffractometer (XRD Rigaku Corporation, Tokyo Japan) with CuK_α

radiation of wavelength of 1.54 Å. Scanning electron microscopy (SEM) was done using FEI Quanta ESEM (FEI Company, Hillsboro, OR). In addition, electron backscatter diffraction (EBSD) technique was employed to analyze grain size and grain orientation for the alloys. Nano-indentation was performed using Hysitron Triboindenter (Hysitron, Inc., Minneapolis, MN) at room temperature using a diamond Berkovich tip. Indentation was done at various loads ranging from 350 μN to 8000 μN with a constant loading time of 5 s, holding time of 2 s, and unloading time of 5 s. The distance between two neighboring indents was maintained greater than 10 μm to avoid overlap of their plastic zones.

6.4. Results

X-ray diffraction patterns of both the equimolar alloys in work hardened and annealed conditions are shown in Figure 6.1 of the supplemental section. All the peaks were indexed as face centered cubic (FCC), indicating no secondary phase formation during mechanical or thermomechanical processing. The lattice parameter for both the equimolar alloys was measured using Bragg's relation to be 3.57 Å for CoCrNi and 3.59 Å for CoCrFeMnNi. Both the alloys showed slightly larger lattice parameter compared to pure Ni (3.52 Å).

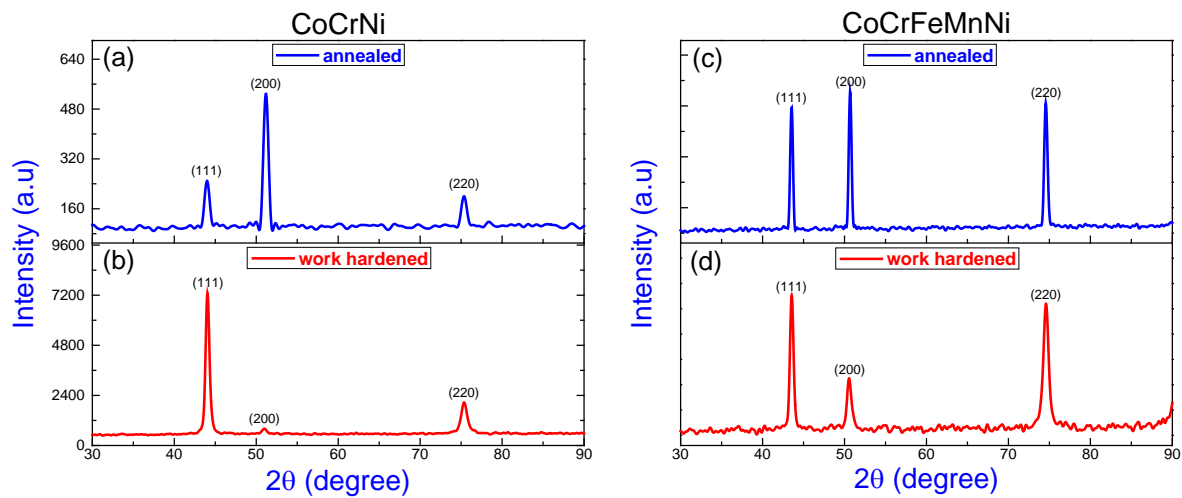


Figure 6.1: X-ray diffraction for annealed and rolled condition for CoCrNi and CoCrFeMnNi.

Backscattered scanning electron microscopy (SEM) images for the two alloys are shown in Figure 6.2.

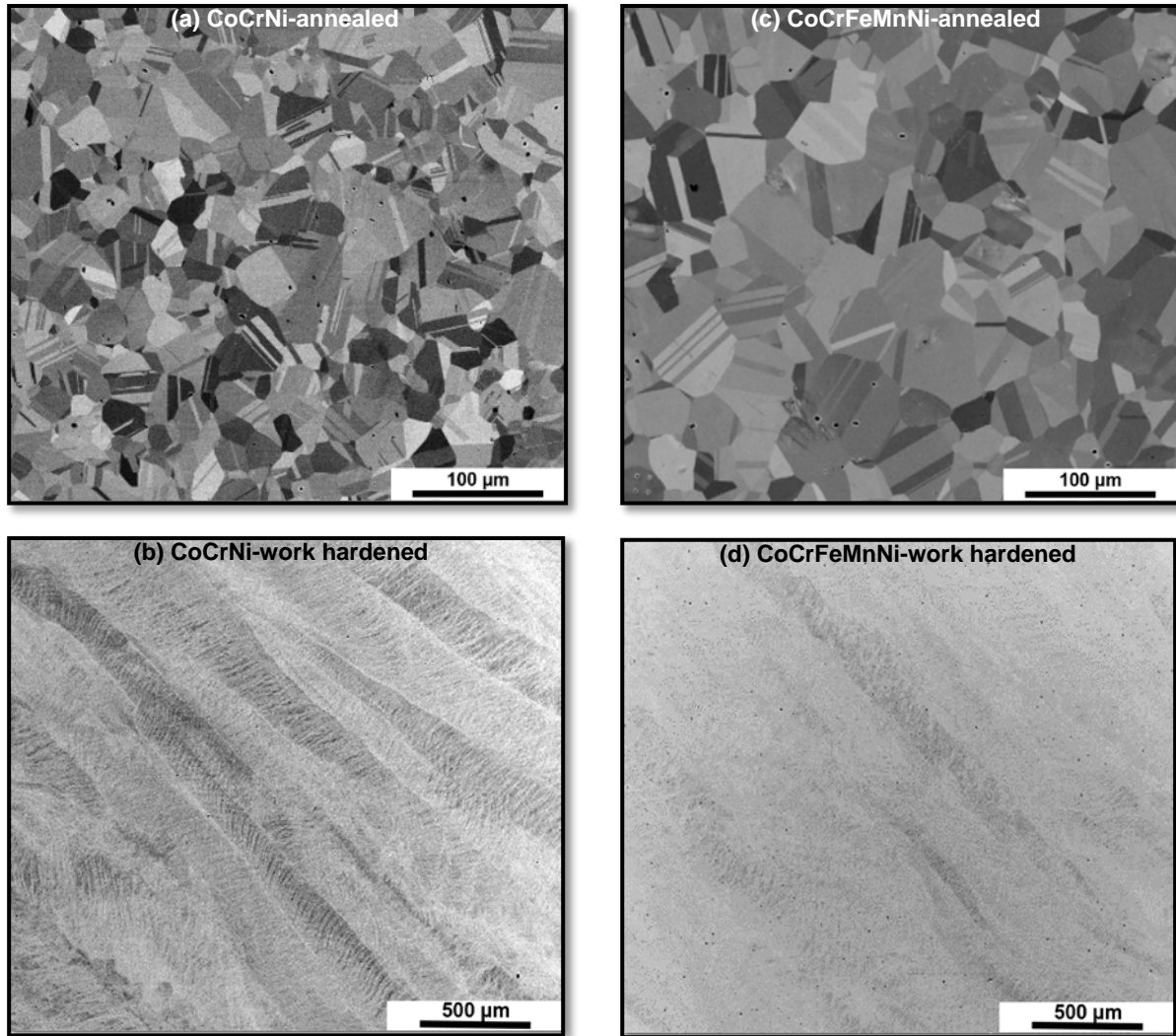


Figure 6.2: SEM backscattered micrographs of CoCrNi alloy (a) annealed and (b) work hardened and CoCrFeMnNi alloy (c) annealed and (d) work hardened condition.

The work hardened alloys showed elongated grains with deformation lines typical of rolled structures. The annealed microstructure consisted of recrystallized equiaxed grains with significant amount of annealing twins. Annealing twin are typically observed in FCC metals and alloys with low stacking fault energy [16]. Electron backscattered diffraction (EBSD) analysis of the two alloys in annealed condition are showed in Figure 6.3, with grain size in the range of 10 μm - 40

μm . Misorientation angle analysis showed that the fraction of low angle grain boundaries ($< 15^\circ$) was about 20% in both the alloys. A significant fraction of $\Sigma 3$ boundaries was also seen ($> 50\%$), which indicates very low stacking fault energy for these alloys and supports the observed annealing twins.

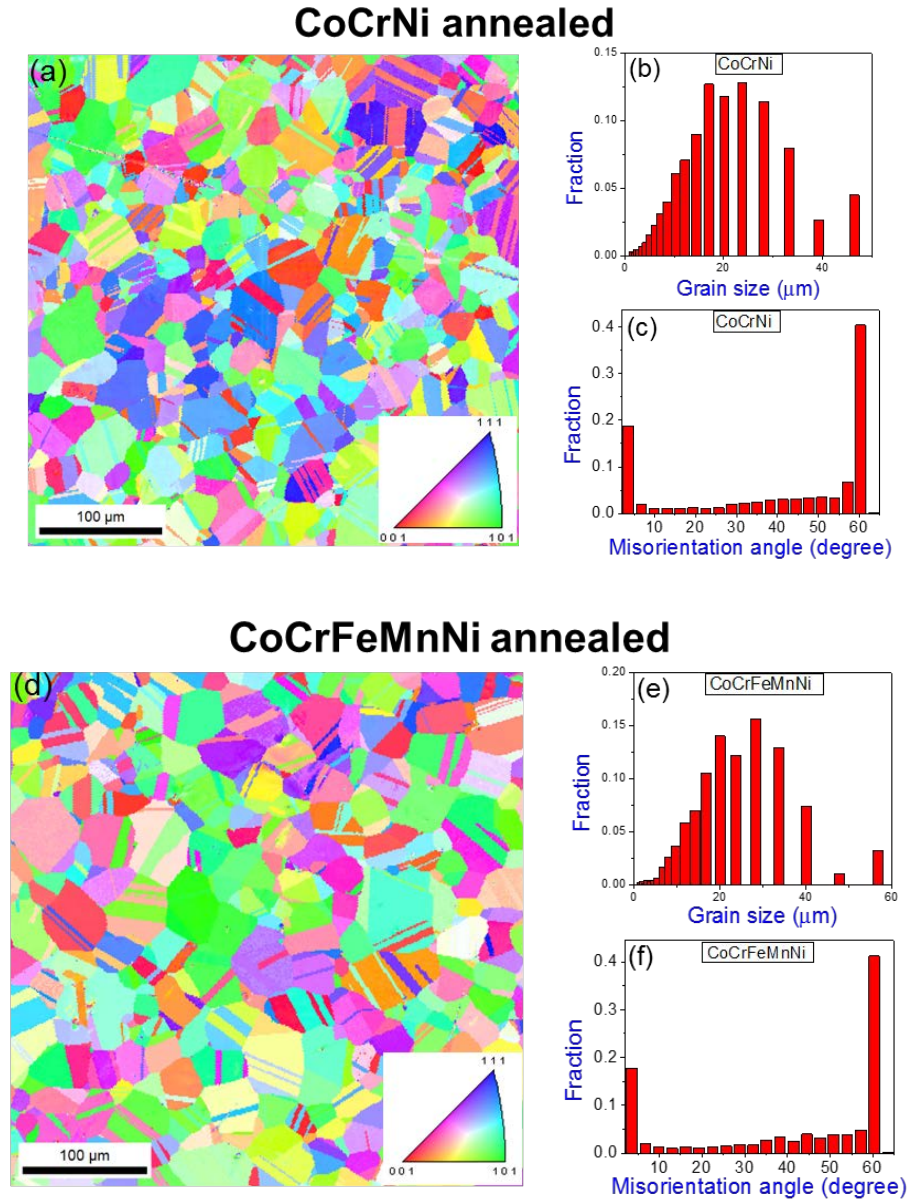


Figure 6.3: EBSD map of (a) CoCrNi alloy and (d) CoCrFeMnNi alloy of annealed sample, (b) and (e) grain size distribution and (c) and (f) misorientation angle for both the annealed sample.

The three component CoCrNi alloy was found to be harder compared to the five component CoCrFeMnNi alloy as shown in Figure 6.4 of the supplemental section. The corresponding load-displacement curves obtained during nano-indentation are also shown in Figure 6.4.

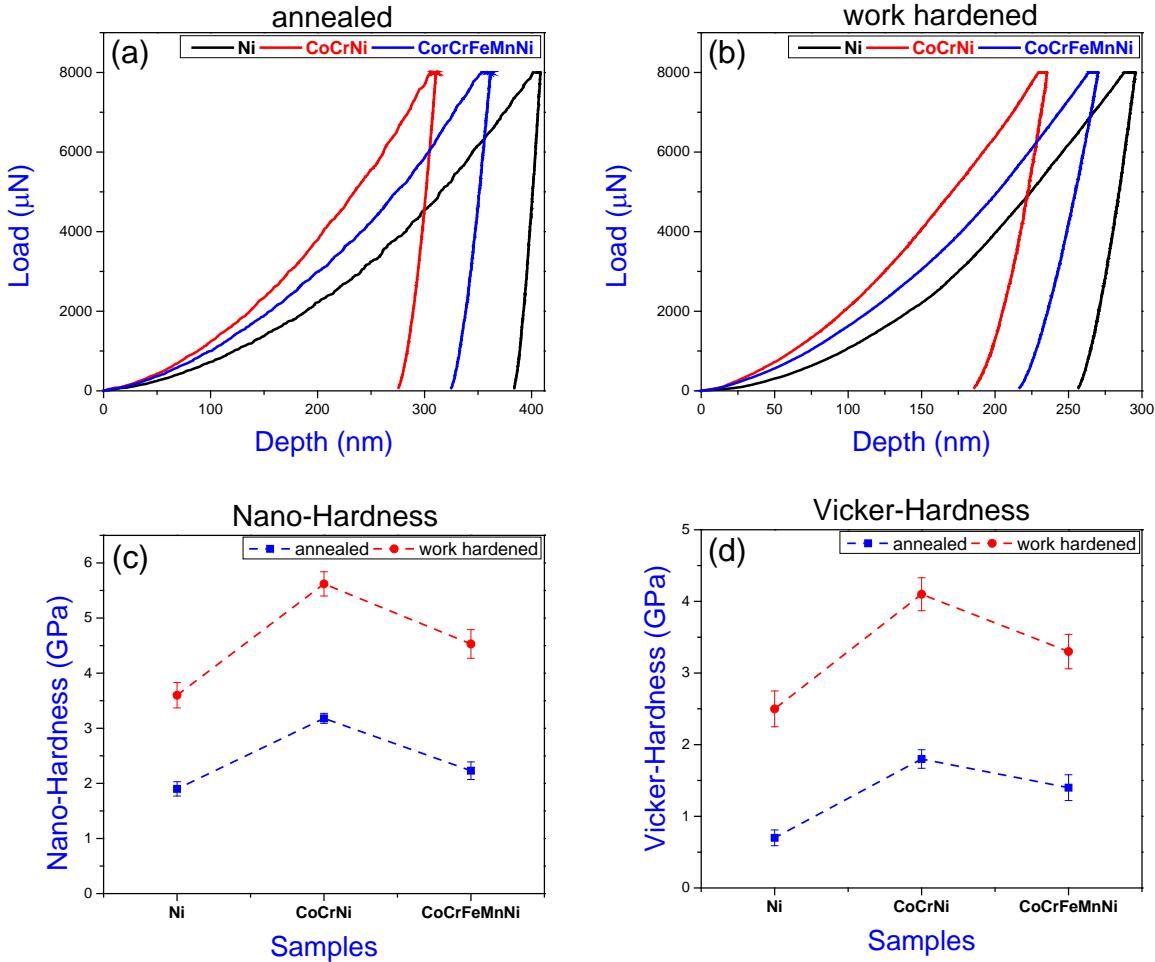


Figure 6.4: (a) and (b) Load-displacement plots at a load of $8000 \mu\text{N}$; (c) and (d) Nano-Hardness and Vicker-Hardness plot for the different processing conditions at a load of $8000 \mu\text{N}$ for Ni, CoCrNi and CoCrFeMnNi.

Increasing number of constituents in solid solution typically results in a strengthening effect. However, our results are to the contrary. An alloy's hardness also depends on nature of the constituent elements and their mutual interaction. For equimolar alloys, solid solution strength

($\Delta\sigma_{SSH}$) based on the assumption of small interaction among solute atoms may be expressed as [17]:

$$\Delta\sigma_{SSH} = \sum_i (B_i^{3/2} X_i)^{2/3} \quad (1)$$

where, X_i is the solute content and B_i is a parameter that depends on the shear modulus (μ) of the alloy, the mismatch factor ϵ_i , and constant Z as [18]:

$$B_i = 3\mu\epsilon_i^{4/3}Z; \quad \epsilon_i = \xi(\eta_i'^2 + \alpha^2\delta_i^2)^{1/2} \quad (2)$$

$$\eta_i' = \frac{\eta_i}{1 + 0.5|\eta_i|}; \quad \eta_i = \frac{d\mu}{dX_i} \frac{1}{\mu}; \quad \delta_i = \frac{ds}{dX_i} \frac{1}{s} \quad (3)$$

where, η_i' is elastic misfit, δ_i is atomic size misfit, and α is a parameter with values in the range of $3 < \alpha < 16$ for screw dislocations and $\alpha > 16$ for edge dislocations, $\xi=1$ for FCC systems and $\xi=4$ for BCC systems. In equation (3), s is interatomic spacing and $\frac{\delta s}{\delta X_i}$ may be expressed as [18]:

$$\frac{\delta s}{\delta X_i} = s_{ii} - X_{k \neq i} S_k X_{k \neq i}' \frac{1}{\bar{X}_{k \neq i}^2} \quad (4)$$

where, s_{ii} is the solvent-solvent interatomic spacing. From the equations, it may be concluded that the atomic size misfit ($\frac{\delta s}{\delta X_i} \frac{1}{s}$) is the principal factor responsible for solid solution strengthening in equimolar alloys. It was observed from $\frac{\delta s}{\delta X_i} \frac{1}{s}$ versus X_i plots, that addition of Fe had a softening effect in CoCrNi alloy [18]. The lower hardness of CoCrFeMnNi in comparison to CoCrNi may be attributed of lattice misfit reduction from addition of Fe compared to Mn.

For depth dependence of hardness, nano indentation was done at loads ranging from 350 μN to 8000 μN . Hardness was found to decrease significantly with increasing load for both the annealed and work hardened alloys as shown in Figure 6.5.

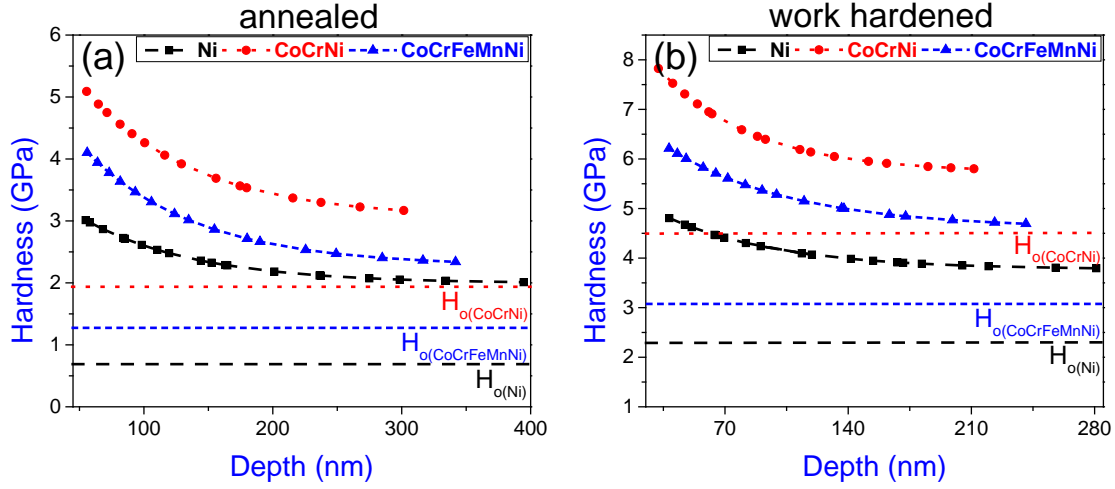


Figure 6.5: Hardness as a function of depth for (a) annealed samples (b) work hardened samples of Ni, CoCrNi and CoCrFeMnNi alloys

The lattice curvature generated during non-uniform plastic deformation by nano-indentation is accommodated by geometrically necessary dislocations (GNDs) [12,19,20]. GNDs restrict the motion of statistically stored dislocations and lead to strain hardening effect [13]. The density of GNDs (ρ_G) in a circular loop around the indenter may be expressed as [9]:

$$\rho_G = \frac{3}{2bh_c} \tan^2 \theta \quad (5)$$

where, b is the Burgers vector, $\tan \theta = h_c/a$, a is the contact radius, and h_c is the contact depth. The shear strength (τ) of a material is related with total density of dislocations and may be expressed as [9]:

$$\tau = \alpha \mu b \sqrt{\rho_T} = \alpha \mu b \sqrt{\rho_G + \rho_s} \quad (6)$$

where ρ_T is the total dislocation density, ρ_s is the statistically stored dislocation density, μ is the shear modulus, and α is a constant. Shear stress (τ) can be converted to hardness (H) using von Mises rule and Tabor's factor as [9]:

$$\sigma = \sqrt{3} \tau; H = 3\sigma \quad (7)$$

Using equations (5) through (7), hardness (H) can be expressed as [9]:

$$\frac{H}{H_0} = \sqrt{1 + \frac{h^*}{h}} \quad (8)$$

$$\text{where } H_0 = 3\sqrt{3}\alpha\mu b\sqrt{\rho_s} \quad (9)$$

$$\text{and } h^* = \frac{81}{2}b\alpha^2 \tan^2 \theta \left(\frac{\mu}{H_0}\right)^2 \quad (10)$$

h^* is the length that characterizes the strain gradient plasticity of a material. h^* is not constant for material and indenter geometry rather depends on the H_0 of the material [9].

Equation (8) suggest the slope of the $(H/H_0)^2$ vs $1/h_c$ plot of a sample will yield the characteristic length h^* of the sample. Figure 6.6 shows the $(H/H_0)^2$ vs $1/h_c$ plots of Ni, CoCrNi and CoCrFeMnNi alloys in annealed and work hardened condition with respective h^* value of the samples. It can be observed the Ni and other alloys, the h^* value in work hardened sample is much lower than the annealed sample and can be contributed to high density of statistical stored dislocation density. In annealed condition the alloys show significant reduction in h^* values compared to the pure Ni. The ternary alloy shows lowest h^* value indicating the hardness of the alloy has lower dependence on the depth whereas the hardness of Ni depends largely on depth. In recent study, it has been shown that depth dependence of the material increases with increasing the solute content [14]. They demonstrated the load dependence for pure Ni, Ni-5Fe and Ni-28Fe alloy. They have found the experimental h^* parameter increased for Ni-5Fe but decreased for Ni-28Fe in comparison to Ni-5Fe. They have contributed this anomaly to the storage volume of GNDs. The solute atom decreases the storage volume of GNDs leading to higher hardness at lower depth [14]. To get the storage the volume of GNDs they used modified N/G model and factor f is

used to relate the volume with N/G model. The modified N/G model consider the density of GNDs as [14,15]

$$\rho_G = \frac{3}{2bh_c} \tan^2 \theta \left(\frac{1}{f^3} \right) \quad (11)$$

$f=1$ represent the original N/G model. According to recent model initially the GNDs form near the surface then can move on any given slip plane. Thus, the storage volume of GNDs is going to include the area where the strain level is high enough for plastic deformation [15]. The determined f value for the material in current study has shown a value of 2.0 for Ni, 1.6 for CoCrNi and 1.7 for CoCrFeMnNi.

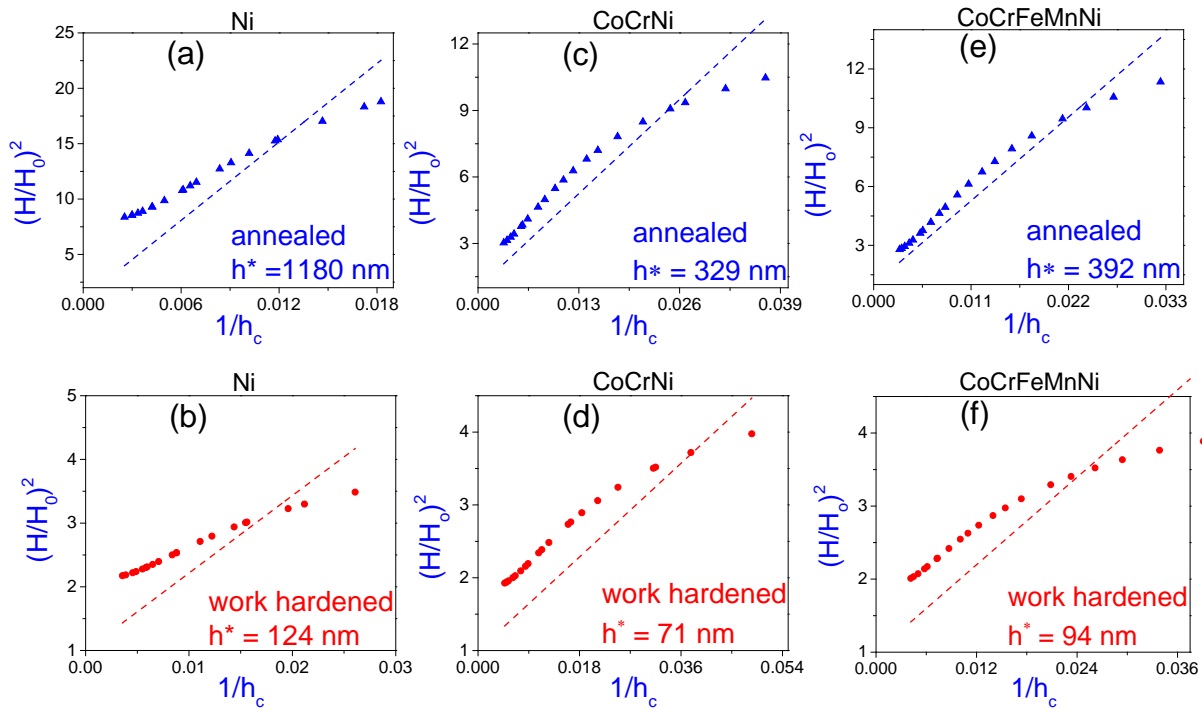


Figure 6.6: $(H/H_0)^2$ versus $1/h_c$ plot to show the depth dependence of hardness for Ni (a) annealed and (d) work hardened, CoCrNi alloy (c) annealed and (d) work hardened and CoCrFeMnNi alloy (e) annealed and (f) work hardened samples.

The storage volume in the ternary and quinary alloys are less than the Ni and can be attributed to internal friction in the alloy. The ternary and quinary alloy show lesser depth dependence which indicate low GNDs density even though storage volume is less. It contradicts the previously proposed conclusion about solid solution alloys. It could be possible the total dislocation generated to accommodate the shape of indenter is much less in the multi-principal alloys compared to the other pure and solid solution material. Several researchers have been proposed a highly distorted lattice in the multi-principal alloys and can be shown by the high lattice misfit in the alloys. It has shown by previous study the CoCrNi has higher lattice misfit compared to the CoCrFeMnNi which contribute to the higher strength of the ternary alloy. It could possible the highly distorted lattice helps in accommodating the indenter shape and leads to formation of less number of GNDs. Even the storage volume is less, as the total line length of the GNDs is less in the multi-principal alloys the depth dependence of the hardness in these alloys is less compared to pure metals and traditional solid solution alloys.

6.5. Conclusions

1. The microstructure evolution and nano-mechanical behavior of single phase FCC five-component and three-component alloys were studied in work hardened and annealed condition. The three-component alloy has higher solid solution hardening effect as compared to the five-component alloy due to higher lattice misfit.
2. Both the alloys showed change in hardness with indentation size due to formation of GNDs to accommodate the plastic deformation occurred by the indenter geometry. Length scale parameter h^* of GNDs was evaluated using Nix and Gao model.

3. Multicomponent alloys showed lower characteristic length scale of GNDs as compared to Ni, which indicates that higher lattice misfit effects in the equi-atomic multicomponent alloys lowers the density of GNDs and reduces the indentation size effect of the alloys.

6.6. References

- [1] M.C. Gao, Progress in high-entropy alloys, JOM. 65 (2013).
- [2] R. Kozak, A. Sologubenko, W. Steurer, Single-phase high-entropy alloys—an overview, Zeitschrift für Kristallographie-Crystalline Materials. 230 (2015) 55-68.
- [3] M. Tsai, J. Yeh, High-entropy alloys: a critical review, Materials Research Letters. 2 (2014) 107-123.
- [4] J.W. Yeh, Y.L. Chen, S.J. Lin, S.K. Chen, High-entropy alloys—a new era of exploitation, 560 (2007) 1-9.
- [5] J. Yeh, S. Chen, S. Lin, J. Gan, T. Chin, T. Shun, C. Tsau, S. Chang, Nanostructured High-Entropy Alloys with Multiple Principal Elements: Novel Alloy Design Concepts and Outcomes, Advanced Engineering Materials. 6 (2004) 299-303.
- [6] Y. Zhang, T.T. Zuo, Z. Tang, M.C. Gao, K.A. Dahmen, P.K. Liaw, Z.P. Lu, Microstructures and properties of high-entropy alloys, Progress in Materials Science. 61 (2014) 1-93.
- [7] B. Gludovatz, A. Hohenwarter, K.V. Thurston, H. Bei, Z. Wu, E.P. George, R.O. Ritchie, Exceptional damage-tolerance of a medium-entropy alloy CrCoNi at cryogenic temperatures, Nature communications. 7 (2016).
- [8] A. Gali, E.P. George, Tensile properties of high-and medium-entropy alloys, Intermetallics. 39 (2013) 74-78.
- [9] W.D. Nix, H. Gao, Indentation size effects in crystalline materials: a law for strain gradient plasticity, J. Mech. Phys. Solids. 46 (1998) 411-425.
- [10] W. Poole, M. Ashby, N. Fleck, Micro-hardness of annealed and work-hardened copper polycrystals, Scr. Mater. 34 (1996) 559-564.
- [11] Q. Ma, D.R. Clarke, Size dependent hardness of silver single crystals, J. Mater. Res. 10 (1995) 853-863.
- [12] A. Arsenlis, D. Parks, Crystallographic aspects of geometrically-necessary and statistically-stored dislocation density, Acta Materialia. 47 (1999) 1597-1611.
- [13] H. Gao, Y. Huang, Geometrically necessary dislocation and size-dependent plasticity, Scr. Mater. 48 (2003) 113-118.
- [14] K. Durst, O. Franke, A. Böhner, M. Göken, Indentation size effect in Ni-Fe solid solutions, Acta Materialia. 55 (2007) 6825-6833.

- [15] K. Durst, B. Backes, O. Franke, M. Göken, Indentation size effect in metallic materials: Modeling strength from pop-in to macroscopic hardness using geometrically necessary dislocations, *Acta Materialia*. 54 (2006) 2547-2555.
- [16] H. Carpenter, S. Tamura, The formation of twinned metallic crystals, *Proceedings of the Royal Society of London. Series A, Containing Papers of a Mathematical and Physical Character*. 113 (1926) 161-182.
- [17] L. Gypen, A. Deruyttere, Multi-component solid solution hardening, *J. Mater. Sci.* 12 (1977) 1028-1033.
- [18] I. Toda-Caraballo, P.E. Rivera-Díaz-del-Castillo, Modelling solid solution hardening in high entropy alloys, *Acta Materialia*. 85 (2015) 14-23.
- [19] J. Nye, Some geometrical relations in dislocated crystals, *Acta metallurgica*. 1 (1953) 153-162.
- [20] M. Ashby, The deformation of plastically non-homogeneous materials, *Philosophical Magazine*. 21 (1970) 399-424.

CHAPTER 7

DISLOCATION NUCLEATION IN MULTI-PRINCIPAL ELEMENT ALLOYS

7.1. Abstract

The nature of incipient plasticity was investigated for multi-principal element alloys, $\text{Al}_{0.1}\text{CoCrFeNi}$, CoCrFeMnNi and CoCrNi , by nano-indentation. The tests were performed at a loading rate of $70 \mu\text{N/s}$ in the temperature ranging of 25°C to 200°C . The activation energy and activation volume were determined using a statistical approach of analyzing the “pop-in” load marking incipient plasticity. The small calculated values of activation energy and activation volume indicate heterogeneous dislocation nucleation mechanism. Based on the analysis, the pop-in event was attributed to heterogeneous dislocation nucleation at surface defects like ledges, vacancy clusters, and hot spots.

Keywords: Dislocation nucleation; Activation volume; Activation energy

7.2. Introduction

Traditional alloy design employs combining secondary elements to the primary element to attain improved mechanical and other properties. These alloys mostly possess complex microstructure with multiple phases. In recent years, there have been multiple development in alloy design, including structure with multiple primary elements in equimolar or near equimolar concentration. Despite the large concentration of composite elements, the resulting alloys demonstrate the formation of single phase solid solutions with simple crystal structures like FCC and BCC. These new class of solid solution alloys have recently attracted substantial amounts of research interest, particularly regarding the enhanced properties of these composites.[1-6]. Hence, a substantial amount of research is currently being conducted to understand these composites' enhanced mechanical properties. It has been hypothesized that this class of alloy has distorted

lattice structure which makes dislocations movement difficult and non-traditional and hence show good strength [7-10]. The dislocation nucleation mechanism in these alloys remains elusive: although some researchers have attributed the nucleation of dislocation in the crystal to incipient plasticity, there are still numerous discrepancies, such as the activation volume associated with dislocation nucleation, in the published studies. [11,12].

Experimentally, incipient plasticity is prominent in the nano-indentation load displacement curve as a displacement burst (pop-in). Nano-indentation technique has been extensively used to observe the elastic to plastic transition in metals and alloys. During nano-indentation the instrument record the displacement with the applied load. Researchers witnessed a distinct displacement burst in the load displacement curve during the elastic-to-plastic transition when a shallow indent in a dislocation-free material was created [13-20]. Since the stress associated with the pop-in (Since the mechanical stress the alloy endured during the pop-in) is approximately equal to the theoretical strength of the material, most investigators have defined the pop-in event as (a mechanism behind?) homogenous dislocation nucleation[15,17,21-27].

Recently, Mason *et al* [28] proposed that pop-in event are vacancy assisted heterogeneous dislocation nucleation. The researchers demonstrated that the pop-in event during nano-indentation is time and temperature dependent, a kinetically limiting process that requires activation energy. According to this theory the pop-in event occurs in thermally and mechanically favorable position which makes it a probabilistic event. They evaluated the activation volume and activation energy associated with the pop-in event, and since the activation energy of the process was too small for homogenous nucleation, they concluded the event is a heterogeneous dislocation nucleation

In this study, we have adopted the statistical approach developed by Mason *et al* [28] to evaluate the activation volume and activation energy associated with dislocation nucleation in multi-principal alloy. For this study five component alloys with composition of CoCrFeMnNi, Al_{0.1}CoCrFeNi (0.1 is the mole fraction of the element) and an equiatomic three component alloys with composition CoCrNi is selected. The evaluated activation volume and activation energy were used to elucidate the mechanism responsible for the composites dislocation nucleation mechanism.

7.3. Experimental

Alloys were prepared with composition CoCrFeMnNi, Al_{0.1}CoCrFeNi and CoCrNi with 99.99% pure element using vacuum arc melting technique in Ar atmosphere. As-Cast alloys were then rolled up to 70% reduction in thickness. The rolled materials were annealed at 900°C for 20h to get equiaxed dislocation free grain. The annealed samples were polished in SiC paper followed by polishing in microfiber cloth with 1µm diamond suspension. The polished samples were then put in vibromet with 0.04 µm colloidal silica suspension a technique that produces a surface finish equivalent in texture to a sample that has been electropolished.

Nano-indentation was performed using Triboindenter (Hysitron Inc, Minneapolis). Elevated temperature indentation was performed in xsol stage with bottom and top heating stage. The stage can go up to 600°C. To avoid oxidation of the sample continuous flow of Ar+5% H₂ gases with a flow rate of 1 lit/min was maintained. The indentation was performed using berkovich diamond tip mounted on low thermal conductivity shaft. The indentation was at maximum load of 200 µN at 25°C, 100°C, and 200°C. 100 indentations were performed at each temperature. 10 µm distance was maintained between two consecutive indentations. The indentation was performed in load control mode with constant loading rate of 70 µN/s.

7.4. Results and Discussion

Figure 1 shows the XRD pattern with peak indexed as FCC for all the alloys. This confirms that the alloys form simple solid solution with FCC crystal structure and free of any intermetallic compound or second phase particle. It has already been reported in several earlier works that these alloys form single phase solid solution and demonstrate excellent thermal stability at high temperature.

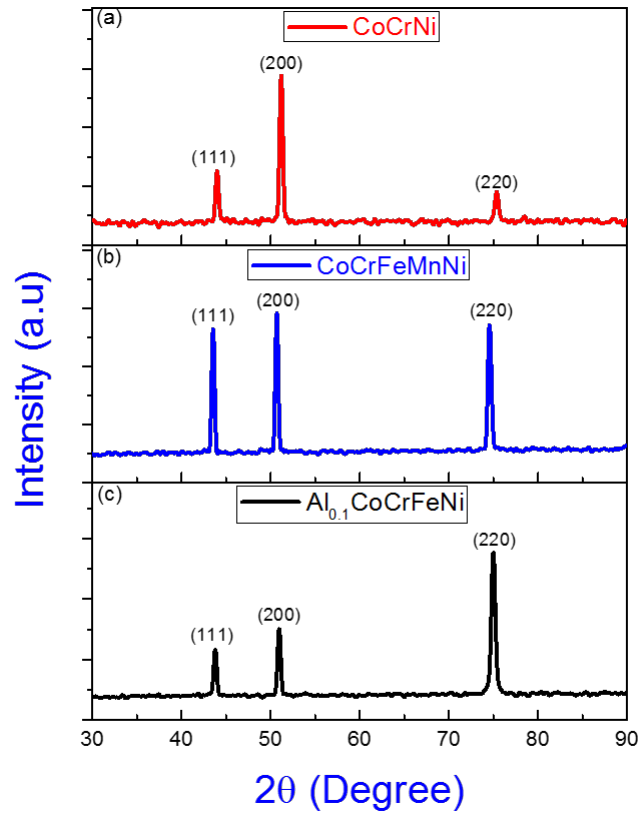


Figure 7.1: XRD pattern of multi-principal CoCrFeMnNi, Al_{0.1}CoCrFeNi, and CoCrNi alloys after rolling and annealing for 20h. The XRD peaks corresponds to single phase FCC structure

Figure 7.2 shows the backscattered SEM image of the alloys. All three of the alloys show equiaxed structure with average grain size of 30-60 μm . All three alloys showed significant amount of annealing twin which indicates low stacking fault energy of these alloys.

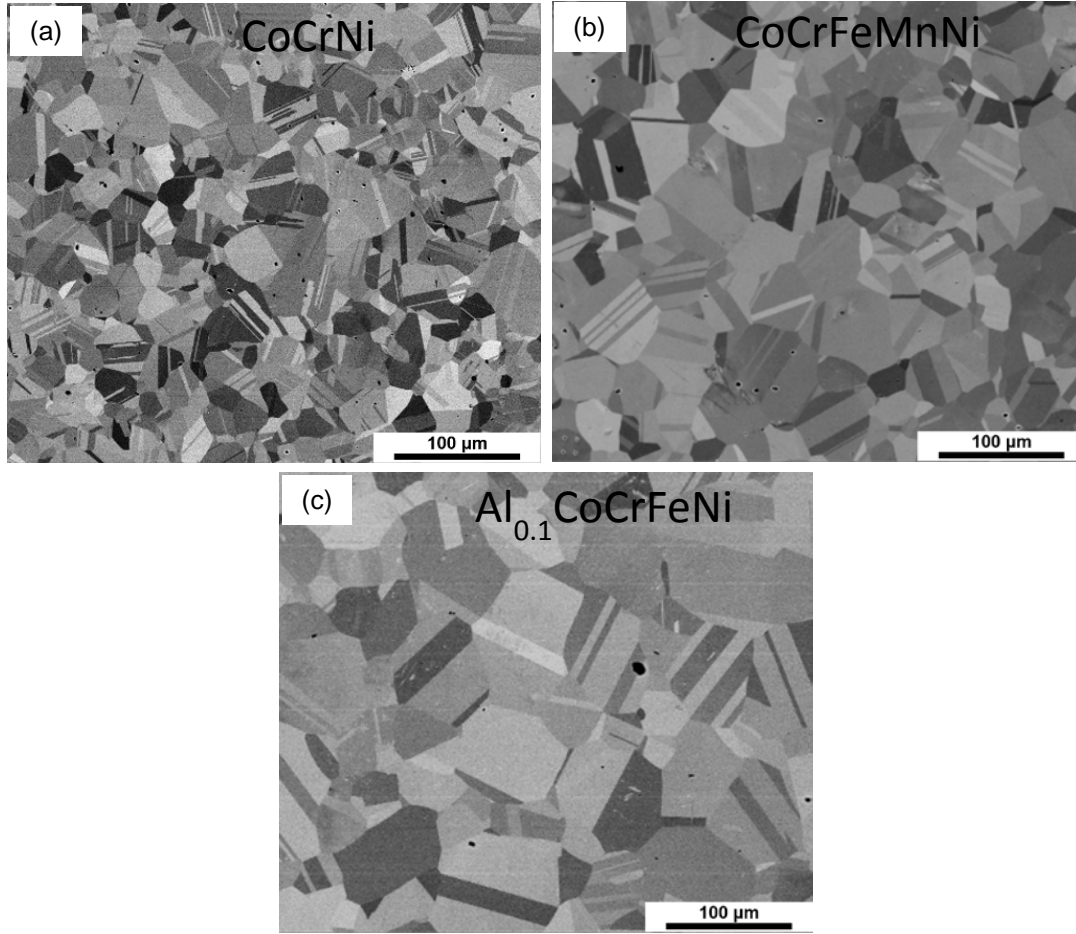


Figure 7.2: Backscattered SEM image of the annealed samples (a) $Al_{0.1}CoCrFeNi$, (b) $CoCrFeMnNi$, (c) $CoCrNi$. Shows equiaxed grain in the alloys after annealing with grain size 30-60 μm .

It has been well documented that the elastic deformation of material during nano-indentation follows the Hetzian contact theory, which states a relation between a circular contact area and planer surface area. The relation between the indenter and sample follow the equation:

$$P = \frac{4}{3} E_r R^{\frac{1}{2}} h^{\frac{3}{2}} \quad (1)$$

where, P is the load applied by the indenter, E_r is the reduce modulus, R is radius of the tip, and h is the indentation depth. Figure 7.3 (a) shows the load-displacement curve obtained from nano-indentation along with the Hetzian equation. The E_r of the alloys are obtained from the slope of

the unloading part of the load-displacement curve and presented in Table 7.1. The obtained modulus is in line with earlier reported results [29,30]. The initial part of the loading load-displacement curve matches with the Hertzian relation and then however, the relation subsequently deviates, indicating a mode of deformation, including plastic deformation or elastic-to-plastic transition, and has been hypothesized to be a homogenous nucleation of dislocation. The load and displacement at the deviation point is determined from the plot for each indent. Figure 7.3 (a) is representative of the curves for different alloys and indentations. Figure 7.3 (b) shows the temperature dependence of the pop-in load for the CoCrFeMnNi alloy. The load at the first pop-in was found to decrease with increasing temperature. Other alloys also showed a similar trend. The temperature and time dependence of pop-in load has been reported for other materials.

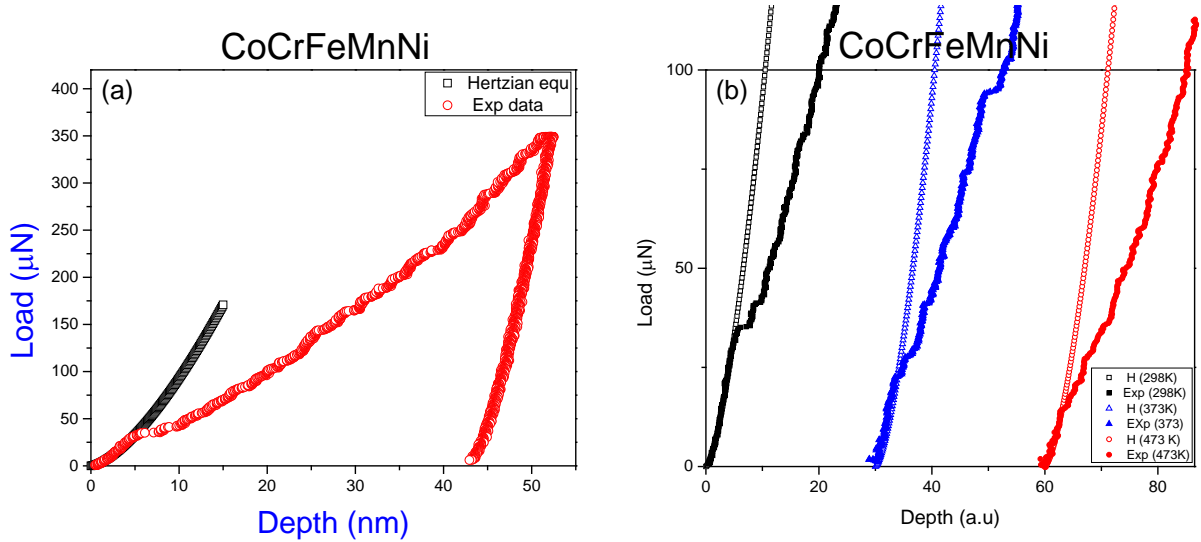


Figure 7.3: (a) representative load-displacement curve of CoCrFeMnNi alloy for single indent performed at room temperature along with the Hertzian. Green circle shows the “pop-in” event in the load-displacement curve. (b) load-displacement curve of CoCrFeMnNi alloy at different temperature along with the Hertzian equation.

Table 7.1: Reduced modulus, activation volume, and activation enthalpy of three alloys.

Alloys	E_r	Activation vol (\AA^3)	Activation energy (eV)
Al _{0.1} CoCrFeNi	190 \pm 5	8.04	0.47 \pm 0.009
CoCrFeMnNi	180 \pm 4	9.01	0.50 \pm 0.007
CoCrNi	195 \pm 6	4.69	0.27 \pm 0.01
Ni	195 \pm 7	6.80	0.39 \pm 0.008

Temperature dependence of the pop-in event conclude it as thermally activated mechanism. The pop-in load show a distribution of the values over a range indicating its stochastic and probabilistic nature. Figure 4 shows statistical distribution of the pop-in load at room temperature and 200°C for Ni, CoCrNi, CoCrFeMnNi, and Al_{0.1}CoCrFeNi. The experimentally obtained data at 100°C follow the same trend. It has not been included in the figure for clarity. It is evident from Figure 7.4 that the pop-in load decreases with increasing temperature. It can be concluded that the temperature dependence of displacement burst in multi-principal alloys indicates a stress- biased thermally activated mechanism behind similar to pure metals.

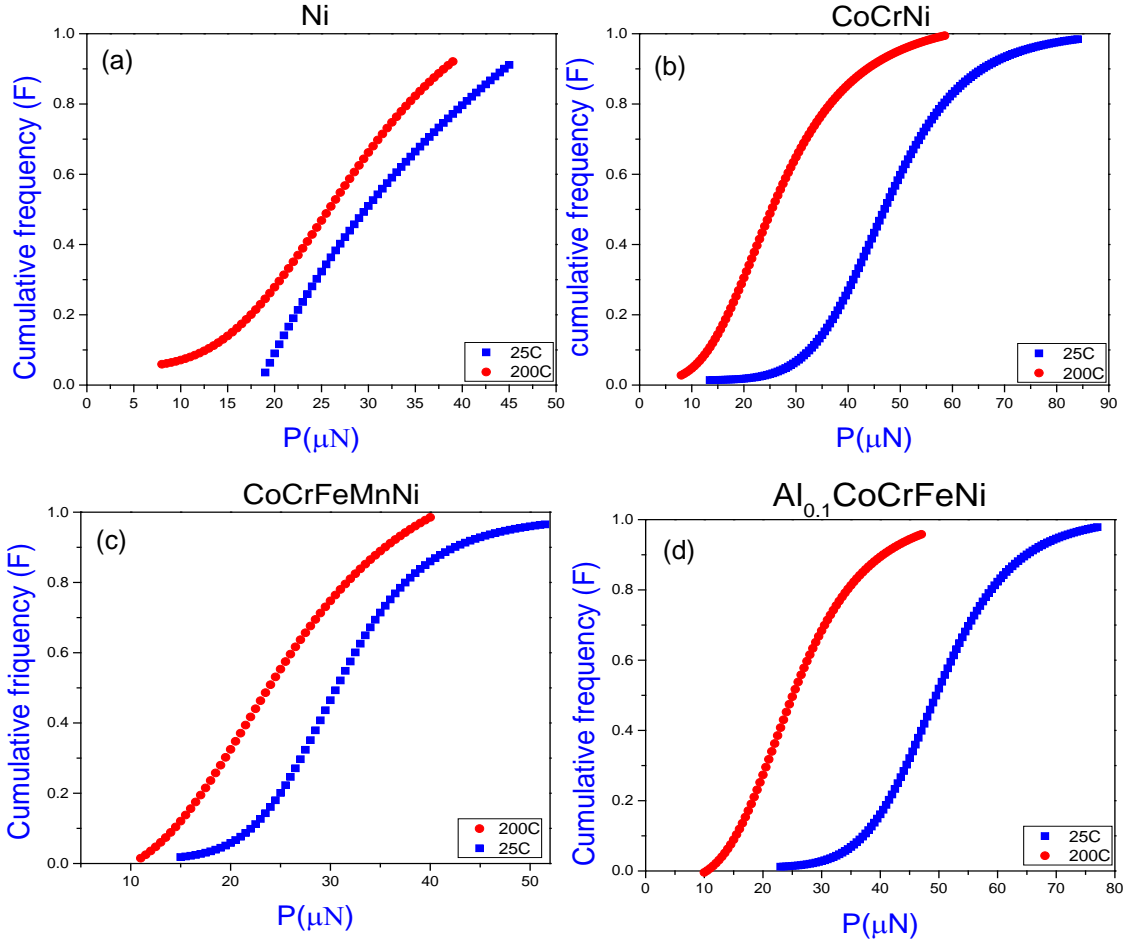


Figure 7.4: Cumulative fraction of experiment loads at the pop-in events plotted for 25°C and 200°C for (a) Ni, (c) CoCrNi alloys, (c) CoCrFeMnNi, and (d) Al_{0.1}CoCrFeNi.

The indentation applies a stress beneath the indenter and shear stress beneath the indenter at pop-in can evaluated using Hertzian contact mechanism theorem.

$$p_m = \left(\frac{6PE_r^2}{\pi^3 R^2} \right)^{1/3} \quad (2)$$

$$\tau_m = 0.31p_m \quad (3)$$

where p_m is mean contact pressure and τ_m is the maximum shear stress at the pop in and ranges from $\frac{\mu}{10} - \frac{\mu}{16}$ (μ is the shear modulus) at room temperature for the three alloys. The ideal shear

strength of a metal also lies in the similar range. It can be concluded the pop-in event involves nucleation of the dislocation. But only stress might not be enough to conclude about the dislocation nucleation mechanism in these alloys.

The activation energy of the process is also of great importance. Using probabilistic distribution of pop-in stress, an analytical solution has been proposed to evaluate the activation volume and activation energy associated with displacement burst [28] . Nucleation of dislocation has activation barrier which may be overcome by the mechanical work done by the indenter or by the combined effect of thermal and mechanical work. The rate equation of the process may be represented by [28]:

$$\dot{n} = \eta \exp\left(-\frac{\varepsilon - \sigma V}{kT}\right) \quad (4)$$

where \dot{n} is rate of the event, η is a pre-exponential factor, ε is the activation energy barrier for the process, and σV represents the stress bias, in which stress σ is activating over activation volume V . In the present condition, the stress bias is the maximum shear stress beneath the indenter.

According to the analytical solution the activation volume of the process can be obtained from the relation [28]:

$$V = \frac{\pi}{0.47} \left(\frac{3R}{4E_R}\right)^{2/3} kT\alpha \quad (5)$$

where α is time independent parameter and can be obtained from the slope of $\ln[-\ln(1-F)]$ vs $P^{1/3}$ plot (Figure 7.5), where F is the cumulative probability of the event. Figure 7.5 shows the $\ln[-\ln(1-F)]$ vs $P^{1/3}$ for the Ni and the three alloys at room temperature and 200C. Using the α value obtained from the slope of the curves and equation (5) the activation volume is calculated. The activation volume for the three alloys and Ni has been presented on Table 7.1. It can be observed the obtained activation volume is almost same in the three alloys and in Ni. Activation volume evaluated for Pt

using same approach showed similar value [28]. It can be concluded the dislocation nucleation mechanism operating these multi-principal element alloys is like the mechanism operating in the pure metals.

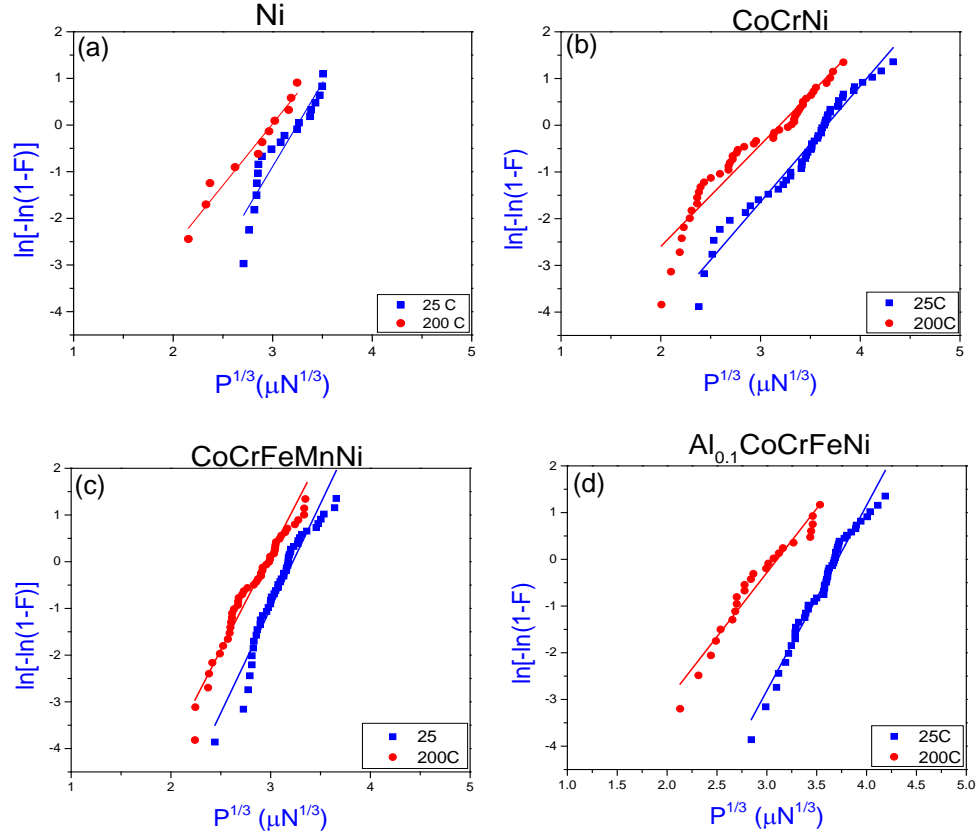


Figure 7.5: Plot of $\ln[-\ln(1-F)]$ vs $P^{1/3}$ to determine the activation volume from experimental data analysis at 25°C and 200°C for (a) Ni, (b) CoCrNi, (c) CoCrFeMnNi, and (d) $Al_{0.1}CoCrFeNi$

Equation (4) shows the ϵ also plays important role in the nucleation process. The activation enthalpy or ϵ can be evaluated from the pop-in load and activation volume using the following relation [28]:

$$P^{1/3} = \gamma kT + \frac{\pi}{0.47} \left(\frac{3\rho}{4E_R} \right)^{2/3} \frac{\epsilon}{V} \quad (6)$$

where γ has weak dependence on T compared to the second part. The method to evaluate the activation energy is, first identify the pop-in load at same cumulative function at different

temperature and to subsequently the pop-in load at same cumulative fraction at different temperature. Figure 7.6 shows the $P^{1/3}$ vs T plot for different alloys. $P^{1/3}$ vs T shows a linear relation with slope γk and intercept at 0K in y axis is the second part of the equation (6). With the obtained $P^{1/3}$ at 0K and activation volume, the ε is obtained which represents the energy required for nucleation at 0K that means all the work is done by mechanical work and no thermal work. The obtained energy is resented in Table 7.1. The activation energy for the alloys and Ni is also in the same range and like pure platinum [28], which indicates the activation of the dislocation source during nano-indentation of multicomponent alloy is by the same mechanism that cause in case of the pure metals.

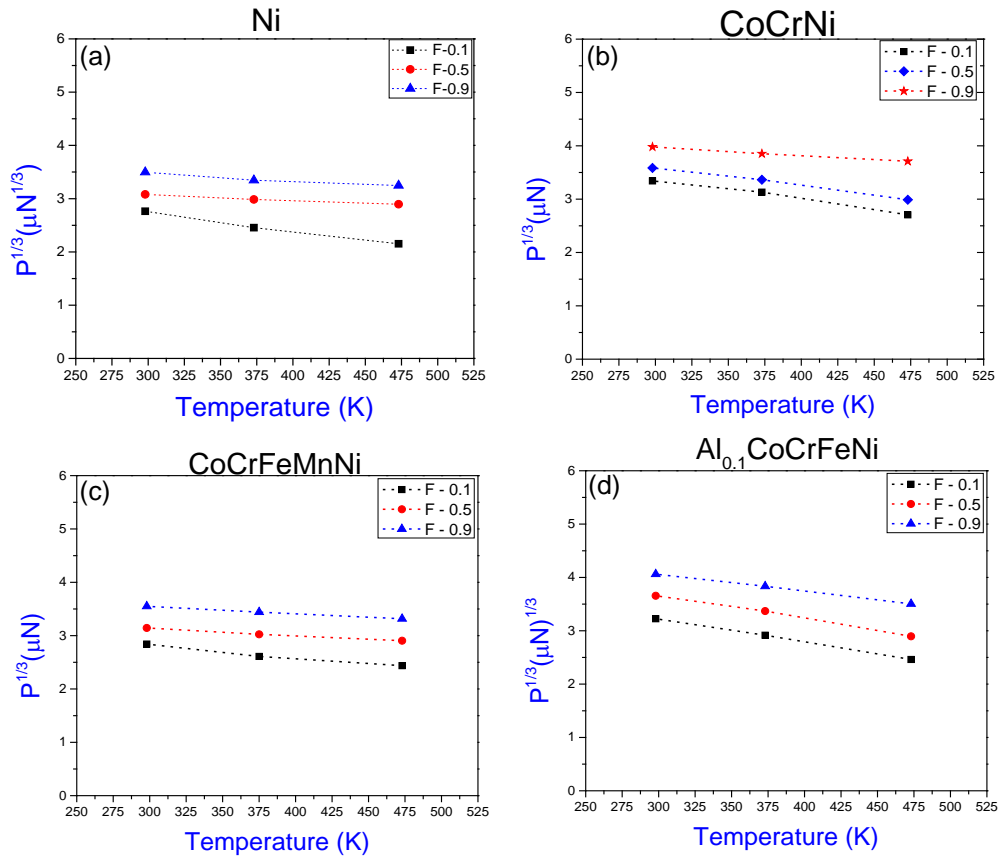


Figure 7.6: Plot of $P^{1/3}$ vs T to evaluate the activation enthalpy for the first burst for (a) Ni, (b) CoCrNi, (c) CoCrFeMnNi, and (d) $\text{Al}_{0.1}\text{CoCrFeNi}$ alloys.

7.5. Discussion

The above mentioned results and analysis for pop-in event indicate the incipient plasticity in these alloys are thermally activated, stress biased phenomenon. In addition the associated activation volume and energy is comparable to pure metals. It might be possible the transition from elastic to plastic deformation in these class of alloys occur by the likely mechanism as in pure metals. Although it is not possible to visually inspect the atomic scale deformation mechanism using the current set up. But the mathematically obtained values can be compared with the existing deformation mechanism.

7.5.1. Homogeneous Dislocation Nucleation

It has been hypothesized by several authors that the first displacement burst is nucleation of dislocation homogeneously [16, 22, 31]. In line with this argument the process would involve cooperative motion of multiple atoms to form stable dislocation nucleation loop with critical radius. In this scenario the critical size loop need to be contained in large atomic volume and the activation energy also reflection of large no of bond breaking which should be much higher than 1eV. In the current study the activation volume and activation energy evaluated for MPEAs using the first order shear bias statistical model is in the range of 4.6 to 8 Å³ and activation energy of 0.27 to 0.50 eV. These values are much lower than that would be required for homogenous dislocation nucleation. This discrepancy in activation volume and enthalpy between experimentally measured and homogenous dislocation loop nucleation mechanism has been reported by several researchers some of them tried to explain it. Few work proposed that dislocation nucleation process is influenced by potential existence of a finite population of subcritical loops assuming the ϵ as function of stress and temperature instead of a constant [32, 33]. Sun *et al.* [34] proposed that presence of subcritical loops in the stressed volume that affect the nucleation via their image stress

filed, τ_{im} . Few researchers proposed another possibility for discrepancy in measured small activation values and required homogenous dislocation loop nucleation [35,36]. They proposed that measured small activation volume and enthalpy corresponds to near atomic size volume for homogenous nucleation dislocation loop's critical size and associated to initial thermal fluctuation site. However, further studies ruled out the possibility of thermal fluctuation site at measured stress. Thermal fluctuations in homogenous nucleation dislocation loop only exist at ideal shear strength, which is not observed in the present work. Based on the above discussion, we can conclude homogenous dislocation nucleation hypothesis can be ruled out for displacement burst event.

7.5.2. Heterogeneous Dislocation Nucleation

The obtained result of the activation energy, ϵ and activation volume, V for all the three alloys indicate an atomic level activity associated with the dislocation nucleation during nano-indentation. Several theories have been proposed regarding the probable nucleation sites. Few authors have proposed the vacancy migration is the dominating deformation dynamics during nano-indentation [11]. But the self-diffusion rate is very slow at room temperature and vacancy migration energy lies in the range of 1-2 eV. The obtained activation enthalpy for all the three alloys are much lower than the vacancy migration energy of pure metals. In addition, it has been concluded by several authors that the equiatomic multicomponent alloys has lower diffusivity than pure metals indicate vacancy migration more difficult in multicomponent alloy than pure metals. Vacancy migration may not be the rate limiting process.

The existing grain boundary and dislocation can also be dislocation site but probability of finding such site is very less. In addition, for these higher order defects the dislocation will expand rather than nucleate. Thus we can eliminate the grain boundary and the pre-existing dislocation as

probable nucleation site. But it has been shown by several author the surface ledges reduce the activation energy when the dislocation nucleates from them. And it is almost impossible to avoid the surface defects. Therefore, the presence of surface ledges can act as potential site for dislocation nucleation.

Another proposed possible heterogeneous dislocation nucleation site for dislocation loop at room or higher temperature is the hot-spot defects. According to these studies at higher temperature, thermal vibrations generate asymmetry which creates hot-spot defects below the surface (in the bulk) and work as a potential site for dislocation nucleation, whereas at 0K, the dislocation nucleates from the surface defects [35,37]. Thus, there are two types of heterogeneous sites at higher temperature. In current study it has been observed the displacement at which “pop-in” occurs decreases with increasing temperature. As example the average indentation depth for CoCrFeMnNi alloy corresponding to 298K, 373K and 473K are 8 nm, 5 nm and 3 nm, respectively. The similar trend is observed for other two alloys Al_{0.1}CoCrFeNi and CoCrNi. The decreasing trend of indentation depth with increasing temperature supports the hot-spot theory as with increasing the temperature the fraction of hot spot defect would increase and lead to lowering the depth and load for “pop-in” confirms the presence of higher fraction of hot-spot defects at higher temperature. The hot-spot could be possible dislocation site for dislocation nucleation above absolute temperature.

Few researcher also suggested the vacancy cluster or presence of impurity elements could be a potential nucleation site for dislocation nucleation [28]. As the alloys are air cooled after annealing, there is a possibility to have vacancy concentration higher than the equilibrium concentration. So, vacancy cluster could be a potential heterogeneous site for dislocation nucleation for these alloys.

7.6. Conclusions

Shallow depth nano-indentation was performed on multi-principal five component $\text{Al}_{0.1}\text{CoCrFeNi}$ and CoCrFeMnNi alloys and on three component CoCrNi alloy to elucidate the mechanism associated at the onset of plasticity for these alloys. Nano-indentation was done at three different temperatures (25°C, 100 °C, 200°C). The experimentally obtained data fitted with statistical model and the activation volume and activation enthalpy of the process was evaluated. The following can be concluded from the obtained experimental and analyzed results:

1. The “pop-in” load marking incipient plasticity was found to decrease with increase of temperature for each of the three alloys.
2. At all the temperatures, the “pop-in” load was not constant rather occurred on a range of loads and at room temperature ranged from $\mu/10$ - $\mu/16$ (μ is the shear modulus) for three alloys.
3. Using the statistical approach, the evaluated activation volume and enthalpy were close to 10 \AA^3 and 0.5 eV respectively. Owing to small activation volume and energy the dislocation nucleation mechanism is believed to be heterogeneous.
4. Both the values are much less than that required for vacancy migration. So, vacancy migration was ruled out as the dominating nucleation mechanism.
5. Surface defects like ledges, vacancy clusters, and “hot spots” created by asymmetry generated by thermal vibration could be potential sites for dislocation nucleation in these alloys during nano-indentation.

7.7. References

- [1] M.C. Gao, Progress in high-entropy alloys, JOM. 65 (2013).
- [2] R. Kozak, A. Sologubenko, W. Steurer, Single-phase high-entropy alloys—an overview, Zeitschrift für Kristallographie-Crystalline Materials. 230 (2015) 55-68.

- [3] M. Tsai, J. Yeh, High-entropy alloys: a critical review, *Materials Research Letters*. 2 (2014) 107-123.
- [4] J.W. Yeh, Y.L. Chen, S.J. Lin, S.K. Chen, High-entropy alloys—a new era of exploitation, 560 (2007) 1-9.
- [5] J. Yeh, S. Chen, S. Lin, J. Gan, T. Chin, T. Shun, C. Tsau, S. Chang, Nanostructured high-entropy alloys with multiple principal elements: novel alloy design concepts and outcomes, *Advanced Engineering Materials*. 6 (2004) 299-303.
- [6] Y. Zhang, T.T. Zuo, Z. Tang, M.C. Gao, K.A. Dahmen, P.K. Liaw, Z.P. Lu, Microstructures and properties of high-entropy alloys, *Progress in Materials Science*. 61 (2014) 1-93.
- [7] B. Gludovatz, A. Hohenwarter, K.V. Thurston, H. Bei, Z. Wu, E.P. George, R.O. Ritchie, Exceptional damage-tolerance of a medium-entropy alloy CrCoNi at cryogenic temperatures, *Nature communications*. 7 (2016).
- [8] A. Gali, E.P. George, Tensile properties of high-and medium-entropy alloys, *Intermetallics*. 39 (2013) 74-78.
- [9] M. Komarasamy, N. Kumar, Z. Tang, R. Mishra, P. Liaw, Effect of microstructure on the deformation mechanism of friction stir-processed Al_{0.1}CoCrFeNi high entropy alloy, *Materials Research Letters*. 3 (2015) 30-34.
- [10] R. Mishra, N. Kumar, M. Komarasamy, Lattice strain framework for plastic deformation in complex concentrated alloys including high entropy alloys, *Materials Science and Technology*. 31 (2015) 1259-1263.
- [11] C. Zhu, Z. Lu, T. Nieh, Incipient plasticity and dislocation nucleation of FeCoCrNiMn high-entropy alloy, *Acta Materialia*. 61 (2013) 2993-3001.
- [12] D. Wu, J. Jang, T. Nieh, Elastic and plastic deformations in a high entropy alloy investigated using a nanoindentation method, *Intermetallics*. 68 (2016) 118-127.
- [13] C.A. Schuh, A.C. Lund, Application of nucleation theory to the rate dependence of incipient plasticity during nanoindentation, *J. Mater. Res.* 19 (2004) 2152-2158.
- [14] Y. Chiu, A. Ngan, A TEM investigation on indentation plastic zones in Ni₃Al (Cr, B) single crystals, *Acta materialia*. 50 (2002) 2677-2691.
- [15] J. Kiely, J. Houston, Nanomechanical properties of Au (111),(001), and (110) surfaces, *Physical Review B*. 57 (1998) 12588.
- [16] N. Tymiak, A. Daugela, T. Wyrobek, O. Warren, Acoustic emission monitoring of the earliest stages of contact-induced plasticity in sapphire, *Acta materialia*. 52 (2004) 553-563.
- [17] D. Lorenz, A. Zeckzer, U. Hilpert, P. Grau, H. Johansen, H. Leipner, Pop-in effect as homogeneous nucleation of dislocations during nanoindentation, *Physical review B*. 67 (2003) 172101.
- [18] S. Syed Asif, J. Pethica, Nanoindentation creep of single-crystal tungsten and gallium arsenide, *Philos. Mag. A*. 76 (1997) 1105-1118.

- [19] S. Corcoran, R. Colton, E. Lilleodden, W. Gerberich, Anomalous plastic deformation at surfaces: Nanoindentation of gold single crystals, *Physical Review B*. 55 (1997) R16057.
- [20] D. Bahr, D. Kramer, W. Gerberich, Non-linear deformation mechanisms during nanoindentation, *Acta materialia*. 46 (1998) 3605-3617.
- [21] Y. Chiu, A. Ngan, Time-dependent characteristics of incipient plasticity in nanoindentation of a Ni 3 Al single crystal, *Acta materialia*. 50 (2002) 1599-1611.
- [22] W. Wang, C. Jiang, K. Lu, Deformation behavior of Ni 3 Al single crystals during nanoindentation, *Acta materialia*. 51 (2003) 6169-6180.
- [23] T.F. Page, W.C. Oliver, C.J. McHargue, The deformation behavior of ceramic crystals subjected to very low load (nano) indentations, *J. Mater. Res.* 7 (1992) 450-473.
- [24] A. Gouldstone, H. Koh, K. Zeng, A. Giannakopoulos, S. Suresh, Discrete and continuous deformation during nanoindentation of thin films, *Acta Materialia*. 48 (2000) 2277-2295.
- [25] S. Suresh, T. Nieh, B. Choi, Nano-indentation of copper thin films on silicon substrates, *Scr. Mater.* 41 (1999) 951-957.
- [26] K.J. Van Vliet, J. Li, T. Zhu, S. Yip, S. Suresh, Quantifying the early stages of plasticity through nanoscale experiments and simulations, *Physical Review B*. 67 (2003) 104105.
- [27] A. Gannepalli, S.K. Mallapragada, Atomistic studies of defect nucleation during nanoindentation of Au (001), *Physical Review B*. 66 (2002) 104103.
- [28] J. Mason, A. Lund, C. Schuh, Determining the activation energy and volume for the onset of plasticity during nanoindentation, *Physical Review B*. 73 (2006) 054102.
- [29] G. Laplanche, P. Gadaud, O. Horst, F. Otto, G. Eggeler, E. George, Temperature dependencies of the elastic moduli and thermal expansion coefficient of an equiatomic, single-phase CoCrFeMnNi high-entropy alloy, *J. Alloys Compounds*. 623 (2015) 348-353.
- [30] A. Haglund, M. Koehler, D. Catoor, E.P. George, V. Keppens, Polycrystalline elastic moduli of a high-entropy alloy at cryogenic temperatures, *Intermetallics*. 58 (2015) 62-64.
- [31] D. Bahr, D. Wilson, D. Crowson, Energy considerations regarding yield points during indentation, *J. Mater. Res.* 14 (1999) 2269-2275.
- [32] M. Khantha, D. Pope, V. Vitek, Cooperative generation of dislocation loops and the brittle-to-ductile transition, *Materials Science and Engineering: A*. 234 (1997) 629-632.
- [33] M. Khantha, D. Pope, V. Vitek, Mechanism of yielding in dislocation-free crystals at finite temperatures—Part II. Applications to the deformation of whiskers and the brittle-to-ductile transition, *Acta materialia*. 45 (1997) 4687-4694.
- [34] Y. Sun, P. Hazzledine, P. Hirsch, Cooperative nucleation of shear dislocation loops, *Phys. Rev. Lett.* 88 (2002) 065503.
- [35] L. Zuo, A. Ngan, G. Zheng, Size dependence of incipient dislocation plasticity in Ni 3 Al, *Phys. Rev. Lett.* 94 (2005) 095501.

- [36] P. Wo, L. Zuo, A. Ngan, Time-dependent incipient plasticity in Ni₃Al as observed in nanoindentation, *J. Mater. Res.* 20 (2005) 489-495.
- [37] R. Wagner, L. Ma, F. Tavazza, L. Levine, Dislocation nucleation during nanoindentation of aluminum, *J. Appl. Phys.* 104 (2008) 114311.

CHAPTER 8

STRAIN RATE SENSITIVITY OF NANOCRYSTALLINE $\text{Al}_{0.1}\text{CoCrFeNi}$ MULTI-PRINCIPAL ELEMENT ALLOY

8.1. Abstract

The mechanical behavior was investigated for nanocrystalline $\text{Al}_{0.1}\text{CoCrFeNi}$ multi-principal element alloy (average grain size ~ 40 nm) synthesized using magnetron sputtering technique. Strain rate sensitivity was determined using *in situ* pico-indentation technique at different strain rates. The nanocrystalline alloy demonstrated 0.2% offset yield strength of ~ 2.4 GPa, 10 times greater than the coarse grained counterpart. Hall-Petch parameters, σ_0 and k for $\text{Al}_{0.1}\text{CoCrFeNi}$ MPEA were 126 MPa and $449 \text{ MPa } (\mu\text{m})^{1/2}$, which are significantly higher compared to pure metals. Higher strength of the nano-crystalline $\text{Al}_{0.1}\text{CoCrFeNi}$ was attributed to the small grain size as well as higher lattice friction due to the distorted lattice. The small activation volume in the multi-principal element alloy ($5b^3$) compared to pure metals was attributed to the difficulty in dislocation movement through the nano-sized grains due to higher Pearl's stress from the lattice distortion.

Keywords: Multi-principal element alloy, Picoindentation; Activation volume; Strain rate sensitivity

8.2. Introduction

Multi-Principal Element Alloys (MPEAs) represent a new alloy design paradigm of combining five or more elements in equiatomic or near-equiatomic proportions [1-4]. In certain compositions, higher configurational entropy suppresses the intermetallic compound formation and leads to formation of random solid solutions [1]. MPEAs have attracted widespread interest due to their intriguing physical and mechanical properties albeit with simple microstructures [3-

8]. Some of the appealing properties include high strength [9], high corrosion resistance [10], outstanding thermal stability [11], cryogenic fracture toughness [12], and sluggish diffusion [13]. Bulk of the research on MPEAs have focused on alloy development [14-17], phase stability [18,19], and mechanical behavior of coarse grain (CG) systems [4,9,20]. In contrast, there are limited reports on nanocrystalline (NC) bulk and micro-/nano-pillar MPEAs. NC metals typically show high strength [21-23], fatigue resistance [24], and wear resistance [22]. NbMoTaW refractory nano-pillar MPEA consisting of NC grains exhibited exceptional strength, ductility and nanostructural stability [25]. Developing nanocrystalline, micro-/nano-pillar MPEAs, and studying their mechanical behavior could provide insights into deformation mechanisms at the reduced length-scale and potentially open up entirely new application domains.

In this paper, we report on the mechanical behavior of nanocrystalline $\text{Al}_{0.1}\text{CoCrFeNi}$ MPEA (average grain size ~ 40 nm) synthesized using magnetron sputtering technique. Strain rate sensitivity was determined using *in situ* pico-indentation technique at different strain rates. Both strain rate sensitivity (m) and activation volume (V^*) were evaluated for detailed insight into the deformation mechanism.

8.3. Experimental

Target alloy of composition $\text{Al}_{0.1}\text{CoCrFeNi}$ was prepared using high purity elements (99.99%) and arc melted in an Ar atmosphere. A thin film of the alloy was deposited by magnetron sputtering technique (AJA International, USA) on a silicon substrate at room temperature (RT), with the base and process pressure maintained at $\sim 3.1 \times 10^{-6}$ Torr, and $\sim 5 \times 10^{-3}$ Torr, respectively. The alloy was deposited at RT in an Ar atmosphere (Ar flow rate 10 sccm) with an applied power of 75 W. Deposition was carried out at a rate of 1.02 Å/s and was optimized by varying the process parameter. Alloy thickness was measured using an optical profilometer (Veeco Inc., USA) and

was around 700 nm. Crystal structure identification was performed using Rigaku III Ultima X-ray diffractometer (XRD Rigaku Corporation, Tokyo Japan) with $\text{CuK}\alpha$ radiation of wavelength of 1.54 nm. Microstructure analysis was performed using Focused Ion Beam (FIB) scanning electron microscope (SEM) (FEI). Nano-pillars were synthesized by milling the thin film using dual beam FIB (FEI). A concentric circular pattern was used to mill out the nano-pillar. Gallium ion beam with current of 10 pA, and operating voltage of 30 kV was used for milling. The nano-pillars had a slight taper with an angle $\sim 2^\circ$ and average diameter of ~ 425 nm. ImageJ software was used to determine the grain size. *In situ* compression tests were performed on the nano-pillars in SEM equipped with PicoIndenter PI 85 (Hysitron, Inc., Minneapolis, MN, USA) using a 2 μm diameter diamond flat punch. Uniaxial compression tests were conducted at strain rates of 1.2×10^{-1} , 1.9×10^{-2} , and $7.5 \times 10^{-3} \text{ s}^{-1}$.

8.4. Results and Discussion

Figure 8.1 (a) shows the XRD patterns for $\text{Al}_{0.1}\text{CoCrFeNi}$ MPEA thin film and target, demonstrating a single phase FCC structure. SEM image of the thin film shows (Figure 8.1 (b)) a uniformly distributed nano-sized grain with the average grain size of $\sim 40 \pm 5$ nm. The SEM images of nano-pillar NC MPEA before and after *in situ* compression test are shown in Figure 8.2 (a and b), and Figure 8.2 (c), respectively. Figure 8.2 (a) shows the nano-pillar with the diamond flat punch. The 450 nm diameter ion milled nano-pillar is shown in Figure 8.2 (b). Uniform plastic deformation of the nano-pillar with no evidence of buckling was observed (Figure 8.2 (c)).

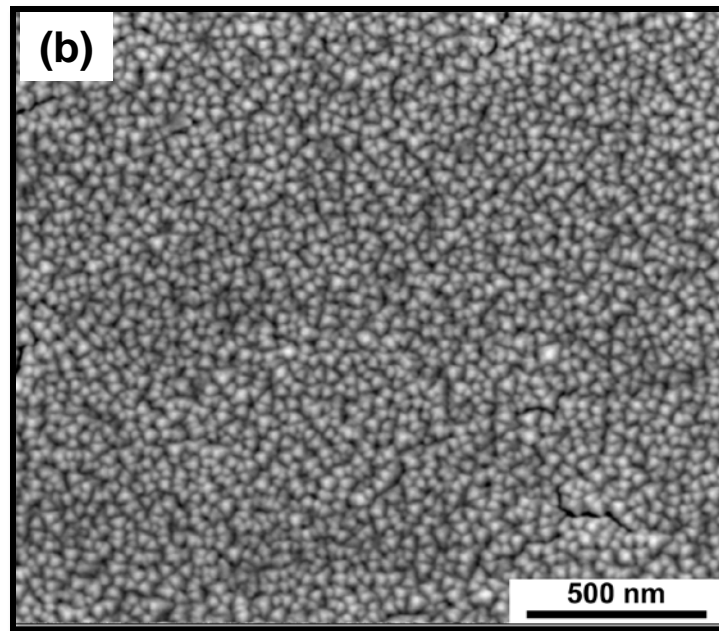
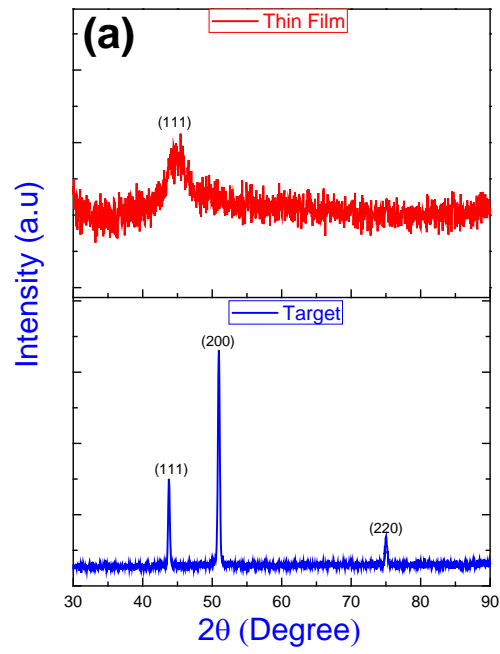


Figure 8.1: (a) XRD patterns of thin film and target $Al_{0.1}CoCrFeNi$ MPEA, showing peak correspond to FCC phase, and (b) SEM image of the thin film showing nano-size grains with average grain size of 40 nm.

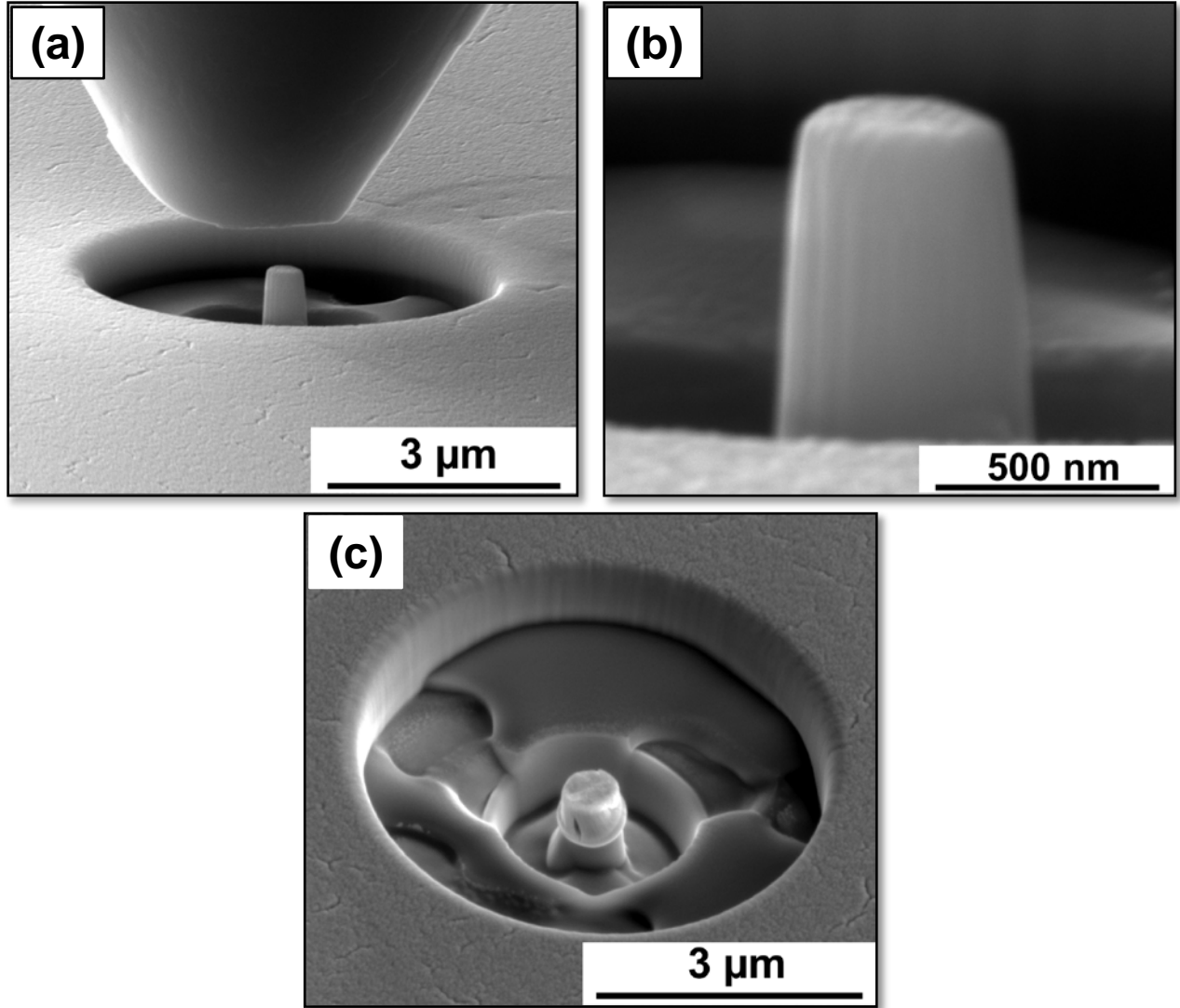


Figure 8.2: (a) SEM image during the test showing diamond punch and nano-pillar (b) SEM image of the nano-pillar with diameter 450 nm (c) SEM image of the nano-pillar after compression test.

Figure 8.3 (a) shows the engineering stress - engineering strain plot at a strain rate of $7.5 \times 10^{-3} \text{ s}^{-1}$. The measured 0.2 % offset yield strength (YS) for the NC MPEA was $\sim 2376 \text{ MPa}$ and was more than an order of magnitude higher than the CG MPEA of same composition [24]. Figure 8.3 (b) shows the YS vs $d^{-1/2}$ plot for MPEA and pure Ni. The Hall-Petch relation, $\Delta\sigma_{HP} = \sigma_0 + k_{HP}d^{-1/2}$ where σ_0 is friction stress in MPa, and k_{HP} is Hall-Petch coefficient in $\text{MPa} (\mu\text{m})^{1/2}$,

was fitted (dotted lines in Figure 8.3 (b)) to obtain σ_0 and k_{HP} . σ_0 and k_{HP} were calculated to be 126 MPa and 449 MPa (μm)^{1/2} for MPEA, and 70 MPa and 250 MPa (μm)^{1/2} for Ni. Hall-Petch coefficient obtained in this study is similar to the earlier reported result [26]. Hall-Petch coefficient for MPEA is remarkably higher than Ni. Therefore, the exceptional strength in NC MPEA is attributed to high Hall-Petch coefficient. Hall-Petch grain boundary strengthening is based on the stress required to activate dislocation sources in the neighboring grain due to dislocation pile-up stress generated at the grain boundary. This phenomenon is difficult in NC material as the grain size is extremely small to accommodate such dislocation activity. In addition to the grain size effect, in the case of NC MPEA, high Hall-Petch coefficient might make the continuation of the plastic deformation a difficult process. Hence, for the same grains size, NC MPEA exhibits higher strength as compared to NC Ni. Therefore, a detailed investigation is required to understand the deformation mechanisms of NC MPEAs.

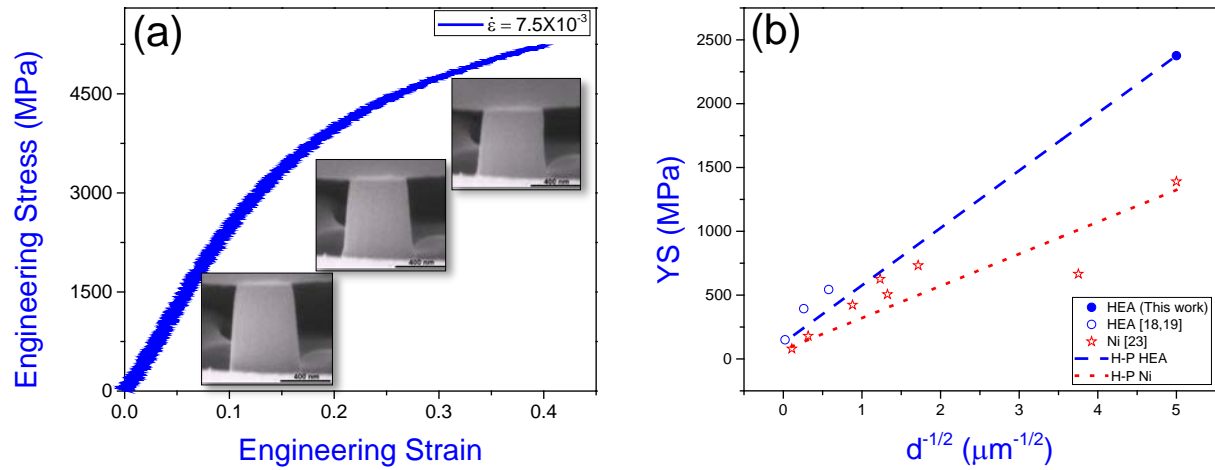


Figure 8.3: (a) Engineering stress – engineering strain curve at strain rate of $7.5 \times 10^{-3} \text{ s}^{-1}$ showing YS of 2376 MPa. Insets show the in situ image of pillar at different engineering strain during the test (b) YS vs $d^{-1/2}$ plot with Hall-Petch equation (H-P) fit. Hall-Petch parameters, σ_0 and k for MPEA were 126 MPa and 449 MPa (μm)^{1/2} and for Ni 70 MPa and 250 MPa (μm)^{1/2}, respectively.

Strain rate sensitivity and activation volume are the two crucial parameters of the dislocation dynamics, which could give insights in to the mechanism controlling plastic deformation. Strain rate sensitivity is defined as [23]: $m = \frac{\partial \ln \sigma}{\partial \ln \dot{\epsilon}}$, where σ is the flow stress and $\dot{\epsilon}$ is the strain rate. And activation volume can be expressed as [22]: $V^* = \frac{\sqrt{3}kT}{m\sigma}$, where k is Boltzmann constant and T is the test temperature. Figure 8.4 (a) shows the stress-strain plots of NC MPEA at strain rates of 1.2×10^{-1} , 1.9×10^{-2} and $7.5 \times 10^{-3} \text{ s}^{-1}$. Strength of the NC MPEA showed significant dependence on strain rate (Figure 8.4 (a)). Figure 8.4 (b) depicts strain rate vs flow stress at 1% offset strain in logarithmic scale. Following equation (1), slope of this plot yielded a strain rate sensitivity of 0.043 for NC MPEA. Based on the m value, equation (2) yielded activation volume of 5 b^3 . The CG counter part of the alloy displayed strain rate sensitivity of 0.02, and activation volume of 284 b^3 [27]. Therefore, compared to the coarse-grained MPEA, large m and small V^* was observed for NC MPEA. For NC Cu with same average grain size as the current NC MPEA, m value of 0.038 and V^* of 20 b^3 was observed [20]. Furthermore, for conventional CG material with low dislocation density, strain rate sensitivity and activation volume are in the range of 0.004-0.008 and few hundred-few thousands of b^3 , respectively [28]. Activation volume in MPEA is smaller than the conventional materials, indicating higher obstacle density and increased difficulty for dislocation motion in MPEA. As noted, interestingly, this observation holds true for the dislocation dynamics in NC MPEA as well.

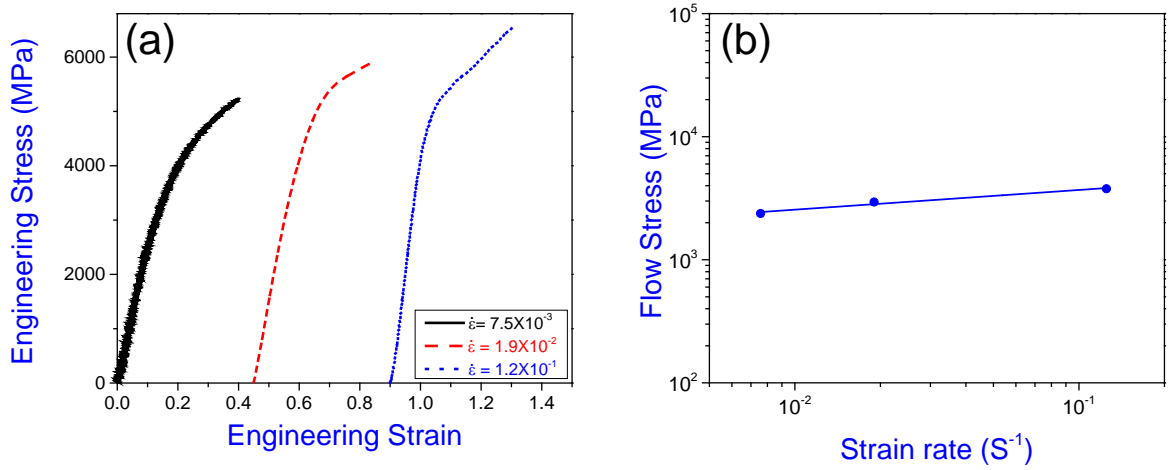


Figure 8.4: (a) Engineering stress - engineering strain plot at different strain rates showing the increase in tensile strength with increase in strain rate; (b) flow stress at 1% offset strain vs strain rate plot in ln scale to calculate the strain rate sensitivity, m . The calculated m was 0.043 for the NC $Al_{0.1}CoCrFeNi$ MPEA.

Main operative deformation mechanism in CG materials can be summarized as (i) intergranular dislocation slip, (ii) dislocation multiplication through Frank-Read source and their interaction, (iii) pile up of dislocations at grain boundary. However, as the length scale falls in the NC regime, intrinsic deformation mechanisms completely changes. Based upon the experimental observations and modeling results in conventional materials, plastic deformation mechanism in NC and CG materials are different. Typically, strain rate sensitivity for grain boundary sliding and coble creep is around 0.5 [29] and 1 [30], respectively. Rate sensitivity is much lower than the diffusion controlled mechanisms, therefore, it can be ruled out for the NC alloy. It might be possible the plastic deformation occurs by dislocation but the mechanism is different from the CG material. Different theories have been proposed to explain behavior of NC material. Some researchers proposed nucleation of dislocation from grain boundary is independent of the pile up stress but dependent on the grain size. The density of dislocation created act as obstacles for

dislocation motion and contribute to the flow strength [31]. Other researchers indicated the nucleation of dislocation is the dominant mechanism for plastic deformation in NC material [21]. Suresh *et al* proposed a mechanistic model for partial dislocation nucleation from grain boundary and formation of twin, which act as obstacle for dislocation motion. The YS related to the stress need to generate the partial dislocation [23]. Researchers have also argued not only the dislocation nucleation but the movement of dislocation is also important. Furthermore, the dislocations nucleate from grain boundary then move through the grain and absorbed in the grain boundary. The dislocation can be get pin down due to interaction with each other or with the grain boundary [32]. A model considering escape of the dislocation with help of thermal activation before forming semicircular loop has also been developed. Nucleation of dislocation from GB in NC material should be easier as there is stress concentration in the atomistic deformed structure of GB. Simulation showed it needs larger stress to propagate than nucleate [33]. The absorption rate of dislocation at the GB is also important. It has been shown in simulation when there is no strain hardening in the NC material there is no pile up near the boundary, the emission and absorption rate is same.

Comparing the NC Ni and MPEA, it can be concluded the strength of the MPEA is twice than the Ni which indicates the stress required to propagation of dislocation through grain is more difficult. The propagation can also involve the density of dislocation that get nucleated. It has been argued the formation of dislocation is easier compare to propagation [34]. In this line the density of dislocation is higher in the MPEA compared to Ni and movement of dislocation is also difficult in MPEA due to high Peierls stress. In accordance with mechanism proposed regarding the thermally activated depinning of the dislocation indicate larger activation energy require in case of MPEA. It has been shown by different authors that the diffusion rate in MPEA is slower. The

stress-strain curve for the MPEA shows large amount of strain hardening which has not been observed in case of pure metals. This could be related to the absorption rate of dislocation. It has been argued the dislocation annihilation involves the movement of atoms at the GB, most probably by diffusion. Annihilation rate should be proportional to rate of diffusion. It could possible due to slower diffusion rate the annihilation rate is slower and lead to pile up at GB and contribute to the strength of the NC alloy.

8.5. Conclusions

Al_{0.1}CoCrFeNi MPEA followed the Hall-Petch relationship down to the nanometer length-scale and NC MPEA showed 10 times higher strength compared to CG alloy of the same composition. Hall-Petch parameters, σ_0 and k for Al_{0.1}CoCrFeNi MPEA were 126 MPa and 449 MPa (μm)^{1/2}, which are significantly higher compared to pure metals. Higher strength of the nano-crystalline Al_{0.1}CoCrFeNi is attributed to the small grain size as well as higher lattice friction due to the distorted lattice. Nano-crystalline Al_{0.1}CoCrFeNi alloy showed strain rate sensitivity of $m=0.043$ and corresponding activation volume of $5b^3$. The small activation volume in the MPEA compared to pure metals maybe attributed to the difficulty in dislocation movement through the nano-sized grains due to higher Pearl's stress from the lattice distortion.

8.6. Future Work

TEM analysis will be performed on the thin film sample to confirm the crystallographic structure of the MPEA. TEM analysis will be performed on the deformed pillar for better insight of the deformation mechanism

8.7. References

[1] J. Yeh, S. Chen, S. Lin, J. Gan, T. Chin, T. Shun, C. Tsau, S. Chang, Nanostructured high-entropy alloys with multiple principal elements: novel alloy design concepts and outcomes, *Advanced Engineering Materials*. 6 (2004) 299-303.

- [2] B. Cantor, I. Chang, P. Knight, A. Vincent, Microstructural development in equiatomic multicomponent alloys, *Materials Science and Engineering: A*. 375 (2004) 213-218.
- [3] M. Tsai, J. Yeh, High-entropy alloys: a critical review, *Materials Research Letters*. 2 (2014) 107-123.
- [4] Y. Zhang, T.T. Zuo, Z. Tang, M.C. Gao, K.A. Dahmen, P.K. Liaw, Z.P. Lu, Microstructures and properties of high-entropy alloys, *Progress in Materials Science*. 61 (2014) 1-93.
- [5] L. Patriarca, A. Ojha, H. Sehitoglu, Y. Chumlyakov, Slip nucleation in single crystal FeNiCoCrMn high entropy alloy, *Scr. Mater.* 112 (2016) 54-57.
- [6] P. Yu, H. Cheng, L. Zhang, H. Zhang, M. Ma, G. Li, P. Liaw, R. Liu, Nanotwin's formation and growth in an AlCoCuFeNi high-entropy alloy, *Scr. Mater.* 114 (2016) 31-34.
- [7] E. Huang, D. Yu, J. Yeh, C. Lee, K. An, S. Tu, A study of lattice elasticity from low entropy metals to medium and high entropy alloys, *Scr. Mater.* 101 (2015) 32-35.
- [8] Y. Brif, M. Thomas, I. Todd, The use of high-entropy alloys in additive manufacturing, *Scr. Mater.* 99 (2015) 93-96.
- [9] F. Otto, A. Dlouhý, C. Somsen, H. Bei, G. Eggeler, E.P. George, The influences of temperature and microstructure on the tensile properties of a CoCrFeMnNi high-entropy alloy, *Acta Materialia*. 61 (2013) 5743-5755.
- [10] C. Hsu, J. Yeh, S. Chen, T. Shun, Wear resistance and high-temperature compression strength of Fcc CuCoNiCrAl_{0.5}Fe alloy with boron addition, *Metallurgical and Materials Transactions A*. 35 (2004) 1465-1469.
- [11] V. Dolique, A. Thomann, P. Brault, Y. Tessier, P. Gillon, Thermal stability of AlCoCrCuFeNi high entropy alloy thin films studied by in-situ XRD analysis, *Surface and Coatings Technology*. 204 (2010) 1989-1992.
- [12] B. Gludovatz, A. Hohenwarter, D. Catoor, E.H. Chang, E.P. George, R.O. Ritchie, A fracture-resistant high-entropy alloy for cryogenic applications, *Science*. 345 (2014) 1153-1158.
- [13] K. Tsai, M. Tsai, J. Yeh, Sluggish diffusion in Co–Cr–Fe–Mn–Ni high-entropy alloys, *Acta Materialia*. 61 (2013) 4887-4897.
- [14] S. Mohanty, N. Gurao, K. Biswas, Sinter ageing of equiatomic Al 20 Co 20 Cu 20 Zn 20 Ni 20 high entropy alloy via mechanical alloying, *Materials Science and Engineering: A*. 617 (2014) 211-218.
- [15] S. Mridha, S. Samal, P.Y. Khan, K. Biswas, Processing and Consolidation of Nanocrystalline Cu-Zn-Ti-Fe-Cr High-Entropy Alloys via Mechanical Alloying, *Metallurgical and Materials Transactions A*. 44 (2013) 4532-4541.
- [16] M.C. Gao, D.E. Alman, Searching for next single-phase high-entropy alloy compositions, *Entropy*. 15 (2013) 4504-4519.
- [17] O. Senkov, G. Wilks, D. Miracle, C. Chuang, P. Liaw, Refractory high-entropy alloys, *Intermetallics*. 18 (2010) 1758-1765.

- [18] C. Ng, S. Guo, J. Luan, S. Shi, C.T. Liu, Entropy-driven phase stability and slow diffusion kinetics in an Al 0.5 CoCrCuFeNi high entropy alloy, *Intermetallics*. 31 (2012) 165-172.
- [19] F. Otto, Y. Yang, H. Bei, E.P. George, Relative effects of enthalpy and entropy on the phase stability of equiatomic high-entropy alloys, *Acta Materialia*. 61 (2013) 2628-2638.
- [20] W. Liu, Y. Wu, J. He, T. Nieh, Z. Lu, Grain growth and the Hall–Petch relationship in a high-entropy FeCrNiCoMn alloy, *Scr. Mater.* 68 (2013) 526-529.
- [21] J. Chen, L. Lu, K. Lu, Hardness and strain rate sensitivity of nanocrystalline Cu, *Scr. Mater.* 54 (2006) 1913-1918.
- [22] Z. Farhat, Y. Ding, D. Northwood, A. Alpas, Effect of grain size on friction and wear of nanocrystalline aluminum, *Materials Science and Engineering: A*. 206 (1996) 302-313.
- [23] R.J. Asaro, S. Suresh, Mechanistic models for the activation volume and rate sensitivity in metals with nanocrystalline grains and nano-scale twins, *Acta Materialia*. 53 (2005) 3369-3382.
- [24] H. Padilla II, B. Boyce, A review of fatigue behavior in nanocrystalline metals, *Exp. Mech.* 50 (2010) 5-23.
- [25] Y. Zou, H. Ma, R. Spolenak, Ultrastrong ductile and stable high-entropy alloys at small scales, *Nature communications*. 6 (2015).
- [26] N. Kumar, M. Komarasamy, P. Nelaturu, Z. Tang, P. Liaw, R. Mishra, Friction stir processing of a high entropy alloy Al_{0.1}CoCrFeNi, *JOM*. 67 (2015) 1007-1013.
- [27] M. Komarasamy, N. Kumar, R.S. Mishra, P.K. Liaw, Anomalies in the deformation mechanism and kinetics of coarse-grained high entropy alloy, *Materials Science and Engineering: A*. 654 (2016) 256-263.
- [28] M.A. Meyers, K.K. Chawla, *Mechanical Behavior of Materials*, Cambridge university press Cambridge, 2009.
- [29] H. Lüthy, R.A. White, O.D. Sherby, Grain boundary sliding and deformation mechanism maps, *Materials Science and Engineering*. 39 (1979) 211-216.
- [30] L. Lu, S. Li, K. Lu, An abnormal strain rate effect on tensile behavior in nanocrystalline copper, *Scr. Mater.* 45 (2001) 1163-1169.
- [31] J. Li, Y. Chou, The role of dislocations in the flow stress grain size relationships, *Metallurgical and Materials Transactions*. 1 (1970) 1145-1159.
- [32] H. Van Swygenhoven, M. Spaczer, A. Caro, Microscopic description of plasticity in computer generated metallic nanophase samples: a comparison between Cu and Ni, *Acta Materialia*. 47 (1999) 3117-3126.
- [33] M. Kato, Thermally activated dislocation depinning at a grain boundary in nanocrystalline and ultrafine-grained materials, *Materials Science and Engineering: A*. 516 (2009) 276-282.
- [34] A.S. Khan, J. Liu, A deformation mechanism based crystal plasticity model of ultrafine-grained/nanocrystalline FCC polycrystals, *Int. J. Plast.* 86 (2016) 56-69.

APPENDIX A

LOAD FUNCTION FOR ROOM TEMPERATURE AND HIGH TEMPERATURE

INDENTATION

It has been observed the load function has a great influence on high temperature hardness and modulus measurement specially in case of material with low creep resistance. The reduce modulus is determined from using the relation: $E = \frac{S\sqrt{\pi}}{2\beta\sqrt{A}}$, where $S = dP/dh$ is slope at the beginning of the unloading curve, β is dimensionless parameter, and A is the contact area of the indentation. In this study two different load functions were used. Figure 1 shows the schematic of two load functions (a) 5 s loading – 2 s holding- 5 s unloading (LF 1 used at room temperature) and (b) 5 s loading – 20 s holding- 0.5 s unloading (LF 2, used at elevated temperature). Both the load functions have same loading rate so the applied strain rate is same for both. For LF1 it has been observed in case of a material with low creep resistance the initial part of unloading curve has a curvature rather than a straight line as the material is still in the primary stage of creep, which leads to wrong estimation of modulus as well as hardness. To avoid that the LF2 was used. In case of LF2 the holding time is high which allows the material to achieve the secondary stage of creep and does not affect the nature of unloading curve. In addition for LF2 a high unloading rate also has been used to avoid the high creep rate effect on the shape of the unloading curve.

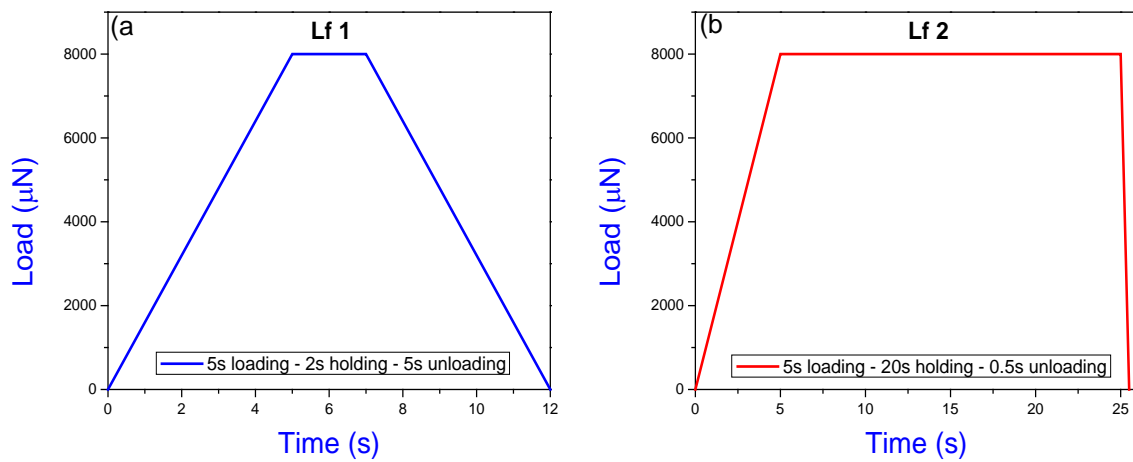


Figure A.1: the schematic of two load functions (a) 5 s loading – 2 s holding- 5 s unloading (LF 1) and (b) 5 s loading – 20 s holding- 0.5 s unloading (LF 2)

APPENDIX B
LIST OF PUBLICATIONS

1. Atomic Distribution in Catalytic Amorphous Metals: **S Mridha**, DL Jaeger, HS Arora, R Banerjee, S Mukherjee Journal of Nanomaterials 2015
2. Evolution of atomic distribution during devitrification of bulk metallic glass investigated by atom probe microscopy: **S Mridha**, DL Jaeger, HS Arora, R Banerjee, S Mukherjee Materials Letters 158, 99-103
3. Nanomechanical Behavior of CoCrFeMnNi High-Entropy Alloy: **S Mridha**, S Das, S Aouadi, S Mukherjee, RS Mishra JOM 67 (10), 2296-2302
4. High Temperature in situ Compression of Thermoplastically Formed Nano-scale Metallic Glass: **Sanghita Mridha**, Harpreet Singh Arora, Joseph Lefebvre, Sanjit Bhowmick, and Sundeep Mukherjee, accepted to JOM, DOI: 10.1007/s11837-016-1961-7
5. Laser assisted high entropy alloy coating on aluminum: Microstructural evolution: S Katakam, SS Joshi, **S Mridha**, S Mukherjee, NB Dahotre Journal of Applied Physics 116 (10), 104906
6. Structural changes in amorphous metals from high-strain plastic deformation: HS Arora, HS Grewal, **S Mridha**, H Singh, S Mukherjee Materials Science and Engineering: A 617, 175-178
7. Thermodynamics and kinetics of laser induced transformation in zirconium based bulk metallic glass: HD Vora, **S Mridha**, S Katakam, HS Arora, S Mukherjee, NB Dahotre Journal of Non-Crystalline Solids 432, 237-245
8. Controlling the length scale and distribution of the ductile phase in metallic glass composites through friction stir processing: HS Arora, **S Mridha**, HS Grewal, H Singh, DC Hofmann, S Mukherjee Science and Technology of Advanced Materials
9. Electromechanical behavior of pulsed laser deposited platinum-based metallic glass thin films: S Das, R Santos-Ortiz, HS Arora, **S Mridha**, ND Shepherd, S Mukherjee physica status solidi (a), 213 (2), pages 399–404, February 2016
10. Surface Modification of Metallic Glass Composites Through Severe Plastic Deformation: S Mukherjee, HS Arora, **S Mridha** Metallurgical and Materials Transactions A 46 (3), 1030-1034
11. High Temperature Nano-mechanical Behavior of Bulk Metallic Glasses: **S. Mridha** and Sundeep Mukherjee; manuscript to be submitted
12. Strain Gradient Plasticity in Multi Principal Element Alloys: **S. Mridha** and Sundeep Mukherjee; manuscript to be submitted
13. Dislocation Nucleation in Multi Principal Element Alloys: **S. Mridha** and Sundeep Mukherjee; manuscript to be submitted
14. Strain Rate Sensitivity of Nanocrystalline Al_{0.1}CoCrFeNi Multi Principal Element Alloy: **S. Mridha** and Sundeep Mukherjee; manuscript to be submitted